

BIOLOGICAL CONSEQUENCES OF CHROMATIN LOOPING IN PERICENTRIC CHROMATIN

Joshua Glenn Lawrimore

A dissertation submitted to the faculty at the University of North Carolina at Chapel Hill in partial fulfillment of the requirements for the degree Doctor of Philosophy in the Curriculum in Genetics & Molecular Biology in the School of Medicine.

Chapel Hill
2018

Approved by:

Kerry Bloom

Dorothy Erie

Michael Falvo

M. Gregory Forest

Paul Maddox

Kevin Slep

©2018
Joshua Glenn Lawrimore
ALL RIGHTS RESERVED

ABSTRACT

Joshua Glenn Lawrimore: Biological Consequences of Chromatin Looping in Pericentric Chromatin
(Under the direction of Kerry Bloom)

During mitosis, replicated sister chromatids are attached to opposite sides of a microtubule spindle at their centromeres in a process called biorientation. The proteinaceous structure that links centromeres, a region of the chromosome, to the spindle is called the kinetochore. Tension within kinetochores of bioriented chromosomes is thought to be crucial for accurate chromosome segregation. The simplest method of generating tension within kinetochores in bioriented chromosomes would be sister chromatid cohesion at the centromere. However, across phylogeny, sister centromeres are separated by 800-1000 nm. Using *Saccharomyces cerevisiae*, we explore how pericentric chromatin, the 20-50 kb region surrounding the centromere, is organized to allow for tension to be generated and regulated at the centromere during mitosis. Pericentric chromatin is enriched in the ring-like protein complexes condensin and cohesin. We find that the pericentromeric region contains several of chromatin loops formed by condensin and cross-linked by cohesin. Simulations of chromatin loops recapitulate the experimental observation that fluorescently labeled regions within pericentric chromatin to appear as compact foci radially displaced from, i.e. above or below, the sister kinetochore. Live-cell imaging experiments with a dicentric plasmid, a circular double stranded DNA molecule that can biorient without replication due to the presence of two centromeres, illustrated the mitotic spindle has sufficient force to extend chromatin during metaphase. Simulations revealed that chromatin loops isolate tension to a geometric subset of chromatin that is directly in between, not above or below, sister kinetochores. Thus, the majority of pericentric chromatin, which is contained in compact loops, is under reduced tension. Additionally, chromatin loops explain the distributions of pericentric cohesin and condensin. Cohesin's radial, barrel-like distribution is due to its ability to diffuse to the radial tips of the loops. Condensin's ability

to form chromatin loops requires condensin to bind to the high-tension chromatin on either side of the low-tension loop, forcing condensin to colocalize with the axial, high-tension chromatin. Chromatin loops recapitulate experimental observations of pericentric chromatin and provide an elegant mechanism for tension modulation at the centromere during mitosis.

To those who helped me along the way.
Thank you for letting me stand on your shoulders.

ACKNOWLEDGEMENTS

I would like to thank all those who have help turn a confused kid into a bemused scientist. The generosity and guidance I've received has been invaluable. Forgive me for limiting the list below to a few highlights.

Mom

Thanks for ensuring I was both smart and kind.

Dad

Thanks for tricking me into thinking deeply about things. At the time, I thought you were just constantly teasing me and beating me at chess.

Dave

Your drive for personal and professional excellence is inspiring. Thanks for leading by example.

Colleen

For everything. Always.

Ajit Joglekar

Thanks for taking a chance on hiring a UNC graduate with no prior lab experience. You are a great mentor.

Ted Salmon

Thanks for taking the time for teaching me how to do good science and explaining why it is so important.

The Fordham 6th Floor Crew

For all those who have mentored, befriended, and helped me, thank you for your patience and advice. I'm trying to pay it in forward.

My Committee, Dorothy Erie, Mike Falvo, Greg Forest, Paul Maddox, and Kevin Slep

I've had the privilege of having a biological chemist, a physicist, an applied mathematician, a cell biologist/microscopist, and a biophysicist come together to guide my research. Your support and insights have enabled me to examine and appreciate biology in ways I couldn't fathom on my own. I am so grateful you all agreed to be on my committee.

Elaine Yeh

You were the emotional and intellectual support I needed to succeed in graduate school. Thank you so much for being there for me.

Kerry Bloom

Thanks for introducing me to true interdisciplinary research. You are a great mentor, friend and example of how to perform great science.

TABLE OF CONTENTS

LIST OF TABLES	x
LIST OF FIGURES.....	xi
LIST OF ABBREVIATIONS AND SYMOBOLS	xiii
CHAPTER 1: DNA LOOPS GENERATE INTRA-CENTROMERE TENSION IN MITOSIS	1
Summary	1
Introduction.....	1
Results	3
Discussion	24
Materials and Methods	29
References	37
CHAPTER 2: CHROMOSHAKE – A CHROMOSOME DYNAMICS SIMULATOR REVEALS CHROMATIN LOOPS STIFFEN CENTROMERIC CHROMATIN	43
Summary	43
Introduction.....	43
Results	46
Discussion	74
Materials and Methods	77
References	93
CHAPTER 3: ROTOSTEP: A CHROMOSOME DYNAMICS SIMULATOR REVEALS MECHANISMS OF LOOP EXTRUSION.....	101
Summary	101

Introduction.....	101
Results	103
Discussion	117
Materials and Methods	119
References	120
CHAPTER 4: CHROMATIN LOOPS CAUSE GEOMETRIC PARTITIONING OF COHESIN AND CONDENSIN	125
Summary	125
Introduction.....	125
Results	127
Discussion	151
Materials and Methods	154
References	162
CHAPTER 5: FUTURE DIRECTIONS	165
Nucleosome Remodeling's Influence on Pericentric Chromatin Dynamics	165
Machine-Learning-Assisted Model Fitting of Protein Distributions to Fluorescent Images	166
References	167
APPENDIX 1: CHROMOSHAKE MANUAL	168
APPENDIX 2: AUTOTRACKER PIPELINE GUIDE	175
APPENDIX 3: DICENTRIC PLASMID TRACKING INTERFACE	180

LIST OF TABLES

Table 1.1 – Radii of confinement calculated for untreated and treated cells.....	1
Table 1.2 – One-dimensional radii of confinement and effective spring constants	10
Table 1.3 – Directional analysis of step size relative to spindle axis	11
Table 1.4 – Percent of directed motion of pericentric chromatin	12
Table 1.5 – Percent of directed motion of pericentric chromatin in <i>bub1Δ</i>	13
Table 1.6 – Percent of directed motion of GFP separation.....	14
Table 1.7 – Frequency and magnitude of elongated TetR-GFP signals	1
Table 1.8 – Strain number and genotypes of yeast strains	31
Table 2.1 – Diameter of cohesin rings after perturbation by thermal forces.....	49
Table 2.2 – Initial and final average radial displacements of chromatin loops and cohesin distribution	56
Table 2.3 – Average plateau values of mean squared displacement curves of arrays of different sizes	60
Table 2.4 – Cross-correlation values of simulated 6.8 <i>lacO</i> / <i>LacI</i> -GFP arrays for motion parallel to the spindle axis	63
Table 2.5 – Comparison of simulated cross-correlation values with published experimental values.....	64
Table 2.6 – The average and standard deviation of the axial and radial displacement of the simulated 6.8 kb array	67
Table 2.7 – The average and standard deviation of the axial and radial displacement of the tips of the radial sub-loops.....	68
Table 2.8 – The average and standard deviation of the axial and radial displacement of the bases of the radial sub-loops.....	69
Table 2.10 – Radius of gyration and average end to end length	89
Table 4.1 – Strain genotypes	156

LIST OF FIGURES

Figure 1.1 – Single particle tracking of pericentric chromatin reveals fluctuations predicted from models of polymer chains tethered at both ends.....	6
Figure 1.2 – Microtubule-dependent events contribute fractionally to off-axis fluctuations	7
Figure 1.3 – Speed correlation index analysis and orientation of pericentric chromatin separation	8
Figure 1.4 – Tension along the spindle axis is sufficient to release nucleosomes	17
Figure 1.5 – Heat map analysis of unreplicated, dicentric plasmids.....	18
Figure 1.6 – Tension along the spindle axis promotes microtubule growth.....	21
Figure 1.7 – Higher DNA binding protein turnover proximal to the spindle axis	23
Figure 1.8 – Mechanistic basis for extensional forces from packed centromere DNA loops	27
Figure 1.9 – Fluctuation and trajectory of dicentric plasmids relative to the mitotic spindle axis	28
Figure 2.1 – Thermal forces collapse radial chromatin loops	48
Figure 2.2 – Distribution and Fluctuations of Experimental and Simulated 6.8 kb Array	51
Figure 2.3 – Chromatin loops dictate cohesin distribution	54
Figure 2.4 – Size of radial loops affects cohesin barrel shape	55
Figure 2.5 – Mean square displacement curves for 1.1 kb and 10 kb LacO arrays	58
Figure 2.6 – Size and position of fluorescent array affects motion of the array.....	59
Figure 2.7. – Correlated motion of simulated 6.8 lacO/LacI-GFP array	62
Figure 2.8 – Cohesin and Condensin confine radial loop fluctuations.....	66
Figure 2.9 – End to end length of simulated chains.....	72
Figure 2.10 – Side chains and cohesin rings can extend chromatin	73
Figure 2.11 – ChromoShake workflow diagram.....	78
Figure 2.12 – Illustration of hinge forces.....	81
Figure 2.13 – Diffusion Validation	87
Figure 3.1 – Simulated step and release algorithm	105
Figure 3.2 – Simulation of condensin walking along a chromatin substrate	106
Figure 3.3 – Kymographs of simulated motion convolved through objective point spread function	108

Figure 3.4 – Chromosome compaction	110
Figure 3.5 – Motion on a dicentric plasmid	113
Figure 3.6 – Condensin enrichment at centromere-proximal DNA loops in simulation with mobile vs. immobile condensin	115
Figure 3.7 – Simulated FRAP experiment by model convolution	116
Figure 4.1 – Motion analysis reveals cohesin confines pericentric chromatin while both cohesin and condensin limit rate of sister foci fluctuations	130
Figure 4.2 – Condensin, not cohesin, stiffens endogenous pericentric chromatin	132
Figure 4.3 – Condensin condenses and stiffens pericentric chromatin	136
Histograms of dicentric plasmid, tetO/TetR-GFP signal lengths reveals condensin creates subpopulation of compacted signals	137
Figure 4.5 Dicentric plasmid models and simulated fluorescent images	140
Figure 4.6 – Static and dynamic loop extrusion compact and stiffen simulated dicentric plasmids	141
Figure 4.7 – Static and dynamic chromatin loops create subpopulations in the signal lengths of simulated dicentric plasmids	142
Figure 4.8 – Temperature sensitive allele, brn1-9, reduces enrichment and increases turnover of pericentric SMC4-GFP	144
Figure 4.9 – Condensin creates two force regimes in chromatin.....	149
Figure 4.10 – Visualization of simulations with neither condensin nor cohesin, and collisions are not necessary to amplify and isolate tension.....	150
Figure 4.11 – Models of WT, mcm21Δ, and brn1-9 pericentric regions	153

LIST OF ABBREVIATIONS AND SYMOBOLS

3C – Chromosome Conformation Capture

FRAP – Fluorescent Recovery After Photobleaching

GFP – Green Fluorescent Protein

kMT – Kinetochore Microtubule

lacO – Lactose Operon

MSD – Mean Squared Displacement

PCR – Polymerase Chain Reaction

Rc – Radius of Confinement

RFP – Red Fluorescent Protein

Rg – Radius of Gyration

RMS – Root Mean Square

RSC – Remodeling the Structure of Chromatin

SMC – Structural Maintenance of Chromosomes

SPB – Spindle Pole Body

SWI/SNF – SWitch/Sucrose NonFermentable

$t_{1/2}$ - Half-life

tetO – Tetracycline Operon

WT – Wild Type

Δ – Null Mutation

CHAPTER 1: DNA LOOPS GENERATE INTRA-CENTROMERE TENSION IN MITOSIS¹

Summary

The centromere is the DNA locus that dictates kinetochore formation and is visibly apparent as heterochromatin that bridges sister kinetochores in metaphase. Sister centromeres are compacted and held together by cohesin, condensin and topoisomerase-mediated entanglements until all sister chromosomes bi-orient along the spindle apparatus. The establishment of tension between sister chromatids is essential for quenching a checkpoint kinase A signal generated from kinetochores lacking microtubule attachment or tension. How the centromere chromatin spring is organized and functions as a tensometer is largely unexplored. We have discovered that centromere chromatin loops generate an extensional/poleward force sufficient to release nucleosomes proximal to the spindle axis. This study describes how the physical consequences of DNA looping directly underlie the biological mechanism for sister centromere separation and the spring-like properties of the centromere in mitosis.

Introduction

DNA looping was first observed in preparations of salamander eggs under the light microscope in the early 1900s (Hertwig, 1906). Paulson and Laemmli found DNA loops that emanate from a protein-rich chromosome scaffold when examining chromosome spreads in mammalian cells (Paulson and Laemmli, 1977). Loops are particularly prominent in meiotic chromosomes (Kleckner, 2006; Zickler and Kleckner, 1999). Most recently, methods such as Hi-C were used to generate genome-wide contacts and provide a statistical, population-averaged, view of the loop organization of the chromosome (Kleckner et al., 2013; Maeshima and Laemmli, 2003; Naumova et al., 2013). Sister chromatids are organized as stacks of radial arrays, with each loop in the array linked at its base. The base of these loops comprise

¹ This chapter previously appeared as an article in The Journal of Cell Biology. The original citation is as follows: Lawrimore, J., Vasquez, P.A., Falvo, M.R., Taylor, R.M., 2nd, Vicci, L., Yeh, E., Forest, M.G., and Bloom, K. (2015). DNA loops generate intracentromere tension in mitosis. J Cell Biol 210, 553-564.

the chromosome scaffold that defines a primary axis spanning the length of the chromosome. These loops have garnered much attention with regard to their role in chromosome packaging and gene expression (Rao et al., 2014).

The radial loops exhibit thermal entropic fluctuations, as well as non-thermal ATP dependent random motion inside cells (Vasquez and Bloom, 2014; Weber et al., 2012). A significant feature of these loops is their influence on the primary axis or chromosome scaffold. Polymer physics shows that a linear polymer will collapse into a random coil in a thermal bath, while a linear polymer with side chains will adopt an entropically-favored state that is more extended than a random coil (de Gennes, 1979). Recent work has demonstrated that a particular type of branched polymer, a bottle brush, with a high number of sidechains (i.e. crowded), can generate extensional forces (outward/poleward) that under certain conditions are strong enough to break covalent bonds (Lebedeva et al., 2012; Panyukov et al., 2009a; Panyukov et al., 2009b). Given that chromosomes contain side loops off a main axis, we wanted to investigate if the centromere region of a chromosome would have similar fluctuations and enhanced tension along its axis as a bottle brush polymer.

The centromere is a unique structure built to mediate chromosome segregation via spindle microtubules in mitosis and to hold sister chromatids together in meiosis I. It is highly condensed relative to the remainder of the genome and is sufficiently compacted that tension at one sister kinetochore can be transmitted to the other sister approximately 1 μm away through kilo- to megabase pairs of DNA. Tension is monitored by surveillance pathways (known as checkpoints) at the kinetochore, but mechanical integrity between sister chromatids is critical for the fidelity of segregation and checkpoint signaling. Like the axis of mitotic mammalian chromosomes, the budding yeast pericentromere is comprised of radial loops emanating from a central scaffold that runs between sister kinetochores. This scaffold is proximal to the spindle axis in budding yeast and is enriched in condensin and cohesin that function in tethering and confining the loops (Stephens et al., 2011; Stephens et al., 2013). Based on the increased concentration of cohesin and condensin, the radial loops are 3X more compacted in the centromere relative to the chromosome arms. Through motion analysis and visualization of conformational states we demonstrate that the spatial arrangement of radial loops in the centromere can

generate tension along the spindle axis. These studies reveal the physical basis for tension between sister chromatids, a conserved mechanism throughout eukaryotes.

Results

Pericentric chromatin motion is dominated by thermal and non-directed ATP-dependent motion, rather than microtubule-based events

We tracked the motion of a 10 kb GFP-labeled chromatin array (lacO/LacI-GFP) relative to a Spc29-RFP-labeled spindle pole body (SPB) at two chromosomal loci during metaphase (Figure 1.1 A). The array was placed at either the pericentric region (6.8 kb from CEN15, Cen-linked) or the arm region (240 kb from CEN2). Both of the arrays appear as nearly diffraction-limited spots. To quantify chromatin motion, we measured the DNA locus position over time. From these data, a radius of confinement (R_c) was estimated from the plateau value of mean square displacement or mean positional variance (Verdaasdonk et al., 2013). The Cen-linked array was more confined than the arm region (Figure 1.1 and Table 1.1 (Verdaasdonk et al., 2013)), and exhibited similar R_c values whether tethered to the spindle pole in G1 (prior to DNA replication and spindle formation) or following DNA replication and spindle formation in G2/M (R_c Cen-linked = 396 nm G1, 363 nm G2/M; R_c Arm = 705 nm G1, 609 nm G2/M Table 1.1 and (Verdaasdonk et al., 2013)). The variance in the X and Y position of LacI-GFP were similar for all array's measured, however when coordinates were rotated in relation to the spindle axis, physical constraints on the pericentric locus were evident in the scatter plots of position of LacI-GFP parallel or perpendicular to the spindle axis (Figure 1.1 B.). The variance, and thus the R_c , in pericentric position was greater parallel to the spindle axis (X-axis), than perpendicular to the axis (Y-Axis) (Figure 1.1 B, Table 1.2). The R_c in arm motion (240 kb) exhibited no directional constraint (Figure 1.1 B, Table 1.2). The reduction in fluctuations of pericentric chromatin relative to arm loci is predicted from polymer models of dual tethered bead-springs (Verdaasdonk et al., 2013). The anisotropy in Cen-linked motion is indicative of radial compression relative to the mitotic spindle axis.

Microtubule dynamics could contribute to pericentric chromatin motion in two ways. One is through the random jostling of kinetochores that is propagated through the pericentric chromatin. The other is through persistent kinetochore microtubule (kMT) growth or shortening that would appear as directed motion. Suppression of microtubule dynamics with the drug benomyl ($t_{1/2}$ of tubulin turnover = 59" WT vs. 259") (Pearson et al., 2003) had little if any influence on Cen-linked motion (Figure 1.1, benomyl).

The spot motion remained anisotropic and Rc values were reduced from 363 nm (WT) to 289 nm (benomyl) (Figure 1.1, Table 1.1, Table 1.2). The step size of benomyl treated pericentric spots was reduced compared to untreated pericentric spots (156 ± 104 vs 177 ± 110 nm, respectively), with the displacement parallel to the spindle axis more reduced than the displacement perpendicular to the spindle axis (Table 1.3). To illustrate directed DNA motion, kymographs were generated from time-lapse images of cells containing labeled pericentric chromatin (6.8 kb from CEN15) and spindle pole bodies. DNA foci undergo infrequent poleward or anti-poleward excursions along the spindle axis (Figure 1.2 A, middle panel). If these excursions are due to kMTs, they should travel at rates similar to kMT dynamics, 17 to 25 nm/s (Gardner et al., 2005). To track chromatin motion, GFP foci and spindle pole bodies were tracked using Gaussian fitting (see Methods). Defining an excursion as any event that persisted for 300, 350, or 400 nm at a rate of > 10 nm/s, we found that directed events comprise 19-11% respectively, of pericentric chromatin motion parallel to the axis, and 4-1% of motion perpendicular to the axis (Table 1.4). Upon benomyl treatment, directed excursions were completely suppressed (Figure 1.1 B, Table 1.4). Since benomyl results in Bub1-dependent phosphorylation of histone H2A (S121) (Haase et al., 2012; Kawashima et al., 2010), we treated *bub1Δ* cells with benomyl. Directed motion was decreased, but not to the degree observed in benomyl treated wild-type cells (Table 1.5). Alternatively, we suppressed microtubule dynamics by depleting protein levels of Stu2 via copper-inducible degradation of Stu2 (Stu2CU) ($t_{1/2}$ of tubulin turnover = 40" WT vs. 233", Kosco et al, 2001, Pearson et al, 2003). Reducing Stu2p levels decreases directed motion but not to the extent of benomyl (See Methods) (Table 1.6). Thus, only a fraction of the directed events can be attributed to microtubule dynamics. These findings lend further support to the conclusion that the drivers of centromere chromatin fluctuations are not dominated by microtubule dynamics.

In addition to directed motion analysis, we measured the speed correlation index (SCI) to quantify the percent of directed motion (Figure 1.3). SCI measures the trajectory of particle motion over time, the more constant the direction, the higher the SCI value. A particle traveling in one direction has an SCI value of 1. A particle traveling in the exact, opposite direction has an SCI value of -1 (Bouzigues and Dahan, 2007). Defining a directed event with an SCI score above 0.5 that persisted for 2 to 5 consecutive windows (each window is an average of 4 frames), we found that directed motion comprised 4-8% of

pericentric chromatin motion. The directed events defined by both analyses are suppressed upon benomyl treatment ($\leq 1\%$ Table 1.4 benomyl, Figure 1.3). Thus, 80-90% of pericentric chromatin motion in untreated cells is non-directed and exhibits a random trajectory.

Separated sister lacO arrays can lie perpendicular to the spindle axis (Snider et al., 2014) (Figure 1.2 C), indicative of non-microtubule based force for centromere separation. Kymographs from these orientations reveal fluctuations similar to those observed in benomyl treated samples (Figure 1.1 C). Disruption of the kinetochore using a temperature sensitive *ndc10-2* mutation also leads to off-axis separated pericentric sister foci (LacO/LacI-GFP 1.7 kb from CEN11) (Figure 1.3 D). Thus, pericentric sister separation is not dependent on directed microtubule-based spindle force. The random motion is a consequence of Brownian motion (thermal fluctuations), non-thermal ATP-dependent events (WT vs. azide treatment, Figure 1.1) and jostling due to the stochastic dynamics of the microtubule plus-ends (Benomyl, Figure 1.1, Figure 1.3).

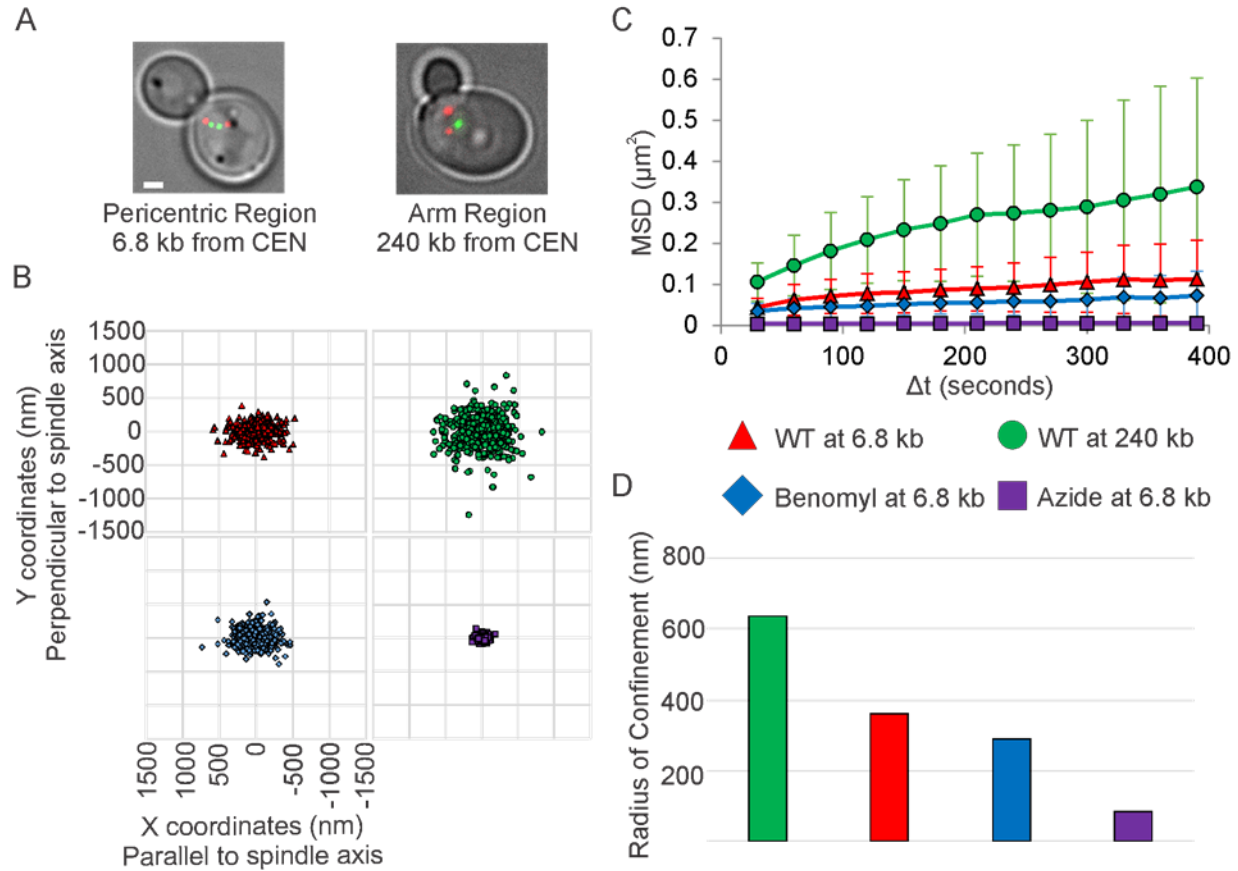


Figure 1.1 – Single particle tracking of pericentric chromatin reveals fluctuations predicted from models of polymer chains tethered at both ends

(A) Representative Images of metaphase yeast with a 10 kb lacO/LacI-GFP array at the pericentromere (6.8 kb) or chromosome arm (240 kb) (green). Spindle pole bodies (SPBs) (Spc29-RFP) in red. Scale bar = 1 micron. (B) Scatter plots of 2D-position relative to the proximal SPB in untreated cells, cells treated with low-doses of benomyl, or with sodium azide + deoxy-glucose. The X-axis is set to the spindle axis. (C) Average mean squared displacement of arrays in untreated and drug treated cells. Error bars are standard deviation. (D) Radii of confinement of untreated and drug treated cells. Values were calculated from the entire population of data (B) from multiple experiments (WT at 6.8 kb $n = 41$, WT at 240 kb = 40, Benomyl at 6.8 kb $n = 41$, and Azide at 6.8 kb $n = 37$). See Table 1 for alternative calculation methods for values with standard deviations. All values are significantly different (Levene's Test, $p < 0.05$).

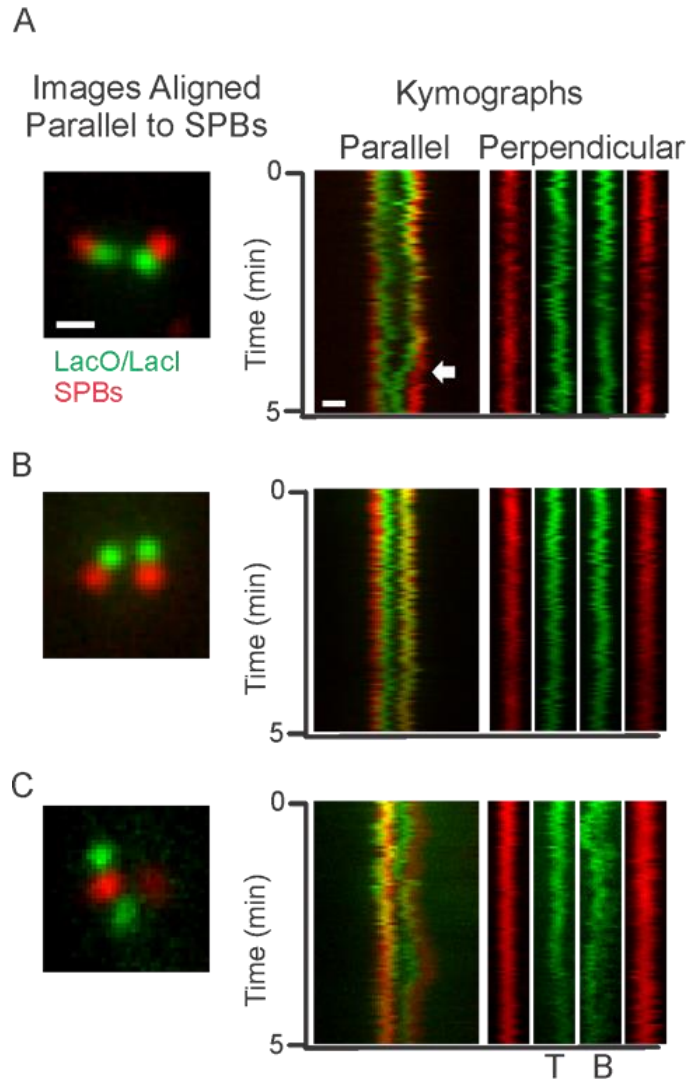


Figure 1.2 – Microtubule-dependent events contribute fractionally to off-axis fluctuations
 (A) Left, image of a metaphase yeast with pericentric chromatin (6.8 kb from CEN15) labeled in green and SPBs (Sp29-RFP) labeled in red. Middle, corresponding kymographs of single-plane timelapses of motion parallel to the spindle axis. Right, kymograph of motion perpendicular to the spindle axis. Arrows indicate an excursion event. Left SPB is fixed in position. Scale bar = 0.5 microns. (B) Left, image of metaphase cells treated with low-concentrations of benomyl. Middle, corresponding kymographs of single-plane timelapses of motion parallel to the spindle axis. Right, kymograph showing motion perpendicular to the spindle axis. Left SPB is fixed in position. (C) Left, image of *cfb5*-AUU mutant cells with a LacO/LacI-GFP array 12.5 kb from CEN11 and labeled SPBs (red). Middle, kymographs of single-plane timelapses of motion parallel to the spindle axis. Right, kymograph of motion perpendicular to the spindle axis. T is the top GFP foci, B is the bottom GFP foci. The bottom GFP foci stretches giving it an elongated appearance in the kymograph.

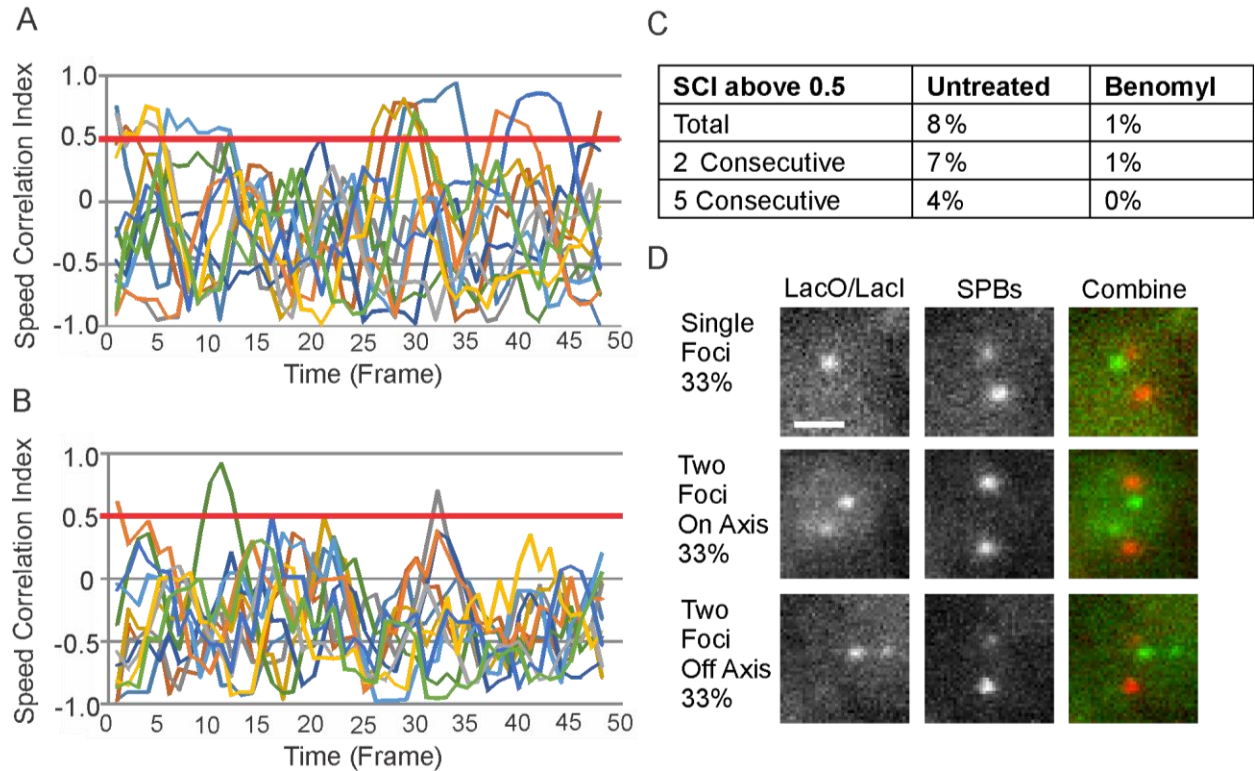


Figure 1.3 – Speed correlation index analysis and orientation of pericentric chromatin separation

(A) Plot of speed correlation index (SCI) over time for untreated cells containing a 6.8 kb LacO/LacI-GFP array. Each line represents an individual GFP foci with the corresponding spindle pole body motion subtracted. Red bar indicates SCI of 0.5, the threshold used for assigning directed motion. SCI was calculated using a window size of 4 frames. The x-axis denotes progression of averaged frames over the ~2.5 minutes of the time course of analysis. The negative skew in SCI is similar to that observed for actin filament motion in the nucleus and attributed to properties of particles imbedded in a viscoelastic medium such as the nucleoplasm (Belin et al., 2013; Weber et al., 2010) (B) Plot of SCI over time for benomyl treated cells. The data shown in A and B are from 6 experiments (two foci each) with SCI values for $n = 12$ foci in both A and B. (C) Summary of the percentage of time SCI was above 0.5 in total, above 0.5 for two consecutive time points, or above 0.5 for 5 consecutive time points for untreated and benomyl treated cells. (D) Representative images of yeast containing an *ndc10-2* mutation at restrictive temperature. Cells contain labeled pericentric chromatin (LacO/LacI-GFP 1.7 kb from CEN11) in green and spindle pole bodies (Spc29-CFP) in red. Pericentric foci in cells with two spindle pole bodies appeared as a single focus, two on-axis foci, or two off-axis foci. The percentage of the population for each phenotype is shown (total $n = 15$). Scale bar is 1 μm .

Table 1.1 – Radii of confinement calculated for untreated and treated cells

LacO array distance from centromere			240 kb Untreated	240 kb Azide	6.8 Untreated	6.8 Benomyl	6.8 Azide
Sample Size (Foci)			40	41	41	41	37
Radius of confinement (nm)	$= \frac{5}{4} * \sqrt{MSD_{plateau}}$	Plateau (individual cell)	664 ± 243	187 ± 68.3	388 ± 152	306 ± 118	89.6 ± 25.6
	$= \frac{5}{4} * \sqrt{(2\sigma^2 + \langle \Delta r_0^2 \rangle)}$	σ (individual cell)	593 ± 170	165 ± 56.7	350 ± 112	280 ± 84	84.0 ± 22.9
		σ (entire data set)	609	172	363	289	86
Effective spring constant (pN/nm)	$= \frac{2k_b T}{\langle MSD_{plateau} \rangle - \langle \Delta r_0^2 \rangle}$	Plateau (individual cell)	9.4x10 ⁻⁵ ± 1.0x10 ⁻⁴	1.22x10 ⁻³ ± 1.7x10 ⁻³	2.4x10 ⁻⁴ ± 2.2x10 ⁻⁴	4.4x10 ⁻⁴ ± 3.9x10 ⁻⁴	4.0x10 ⁻³ ± 4.0x10 ⁻³
	$= \frac{k_b T}{\sigma^2}$	σ (individual cell)	9.1x10 ⁻⁵ ± 5.7x10 ⁻⁵	1.54x10 ⁻³ ± 1.8x10 ⁻³	2.9x10 ⁻⁴ ± 2.2x10 ⁻⁴	4.4x10 ⁻⁴ ± 3.4x10 ⁻⁴	4.7x10 ⁻³ ± 3.4x10 ⁻³
		σ (entire data set)	6.9x10 ⁻⁵	8.6x10 ⁻⁴	1.9x10 ⁻⁴	3.1x10 ⁻⁴	4.7x10 ⁻³

Table 1.2 – One-dimensional radii of confinement and effective spring constants

Name	Sample Size (number of coordinates)	Radius of Confinement		Effective Spring Constant		Levene's Test Parallel vs Perpendicular P-value
		Parallel to axis	Perpendicular to axis	Parallel to axis	Perpendicular to axis	
6.8 kb (Chr XV) Untreated	525	594	349	1.5×10^{-4}	4.2×10^{-4}	4×10^{-18}
6.8 kb (Chr XV) Benomyl	861	483	335	2.2×10^{-4}	4.6×10^{-4}	1×10^{-12}
6.8 kb (Chr XV) Azide	441	130	110	3.0×10^{-3}	4.3×10^{-3}	0.01
240 kb (Chr II) Untreated	609	793	716	8.1×10^{-5}	1.0×10^{-4}	0.06

Radii and effective spring constants calculated using population variance in a single dimension.

Table 1.3 – Directional analysis of step size relative to spindle axis

	Wildtype (3 s Interval)	Benomyl (3 s Interval)	Wildtype (30 s Interval)	Benomyl (30 s Interval)
Average Step Size* (nm)	81 ± 54	63 ± 39	177 ± 110	156 ± 104
Average Displacement Parallel to Axis+ (nm)	51 ± 46	37 ± 32	143 ± 116	112 ± 98
Average Displacement Perpendicular to Axis+ (nm)	46 ± 43	41 ± 33	85 ± 77	89 ± 82

*The one dimensional step sizes of LacO/LacI-GFP foci were calculated using pythagorean theorem. Wildtype 3 s n=698, Benomyl 3 s n=1601, Wiltype 30 s n=525, Benomyl 30s n=861.

+ How far each foci traveled in a single dimension, either parallel and perpendicular to the spindle axis, during each step. Wildtype 3 s n=710, Benomyl 3 s n=1616, Wiltype 30 s n=820, Benomyl 30s n=500

Table 1.4 – Percent of directed motion of pericentric chromatin

Minimum Displacement (nm)	Untreated (n=22 foci)		Benomyl (n = 16 foci)		kMT dynamics from mitotic simulation*
	Parallel	Perpendicular	Parallel	Perpendicular	
300	19%	4%	0%	0%	20%
350	16%	1%	0%	0%	14%
400	11%	0%	0%	0%	9%

*Simulated kMT dynamics were generated using the default settings of a MATLAB Mitotic Spindle Simulation that incorporates kMT dynamics with a chromatin spring to recapitulate lacO fluctuation and stretching in wild-type and mutant cells (Stephens et al., 2013a).

Table 1.5 – Percent of directed motion of pericentric chromatin in bub1Δ

Minimum Displacement (nm)	Untreated (n = 13 foci)		Benomyl (n = 11 foci)	
	Parallel	Perpendicular	Parallel	Perpendicular
300	29%	3%	14%	4%
350	20%	3%	11%	4%
400	14%	0%	7%	2%

Table 1.6 – Percent of directed motion of GFP separation

Minimum Displacement (nm)	Untreated Stu2 ^{CU} (n=4 cells)	Copper Added Stu2 ^{CU} (n=4 cells)	Benomyl Stu2 ^{CU} (n=3 cells)	Untreated WT (n=11 cells)	Benomyl WT (n=8 cells)
300	50%	17%	4%	7%	2%
350	41%	15%	2%	6%	2%
400	35%	14%	0%	6%	0%

Pericentric chromatin is subject to higher tension proximal to the spindle axis

During metaphase LacO signals in pericentric chromatin occupy two distinct areas throughout the spindle. The majority of LacO signals (90%) appear as near-diffraction spots and are radially displaced from the spindle axis, while the elongated filaments reside closer to the axis. A focus that is stretching will move closer to the spindle axis and a filament compacting into a focus will move away from the spindle axis (Stephens et al., 2011; Stephens et al., 2013). To characterize the force along the axis, we used a conditionally functional dicentric plasmid with an excisable origin of replication (Dewar et al., 2004). Growth in the appropriate media prevents DNA replication and activates the conditional centromere. Each centromere independently attaches to kinetochore microtubules and the un-replicated plasmid bi-oriens on the mitotic spindle. The DNA is visualized via tetR-GFP bound to a tandem tetO operator DNA array (5.5 kb TetO/7kb total, 1.8-micron B-form length, 260 nm nucleosome fiber) between the two centromeres. Elongation was defined as an increase in the ratio of the axes of a distribution of the TetR-GFP signal (parallel 1.2X > perpendicular). The short span of DNA between the two centromeres reduces the potential for DNA looping, predisposing the DNA toward the spindle axis. Images of foci and stretching events are shown in Figure 1.4 A. As with endogenous chromosomes, TetR-GFP signals from dicentric plasmids that are elongated lie closer to the spindle axis than signals that appear as foci (Figure 1.5). The dicentric plasmid was elongated in ~45% of cells (1.0 – 1.5 μm spindle length) (Table III), vs. 10% for chromosomal spots (Stephens et al., 2011). As the spindles elongate, more frequent and greater extensions of plasmid DNA are observed (Figure 1.4 B, ~86%, >2 μm spindles). The average dicentric chromatin extension in metaphase (1.0 to 2.0 μm spindle length) was ~630 nm. This corresponds to the release/unwrapping of approximately 6 nucleosomes (for loss of 6 nucleosomes, 320 nm of 11 nm fiber + 320 nm 2 nm fiber = 640 nm).

The force for generating tension between sister centromeres has been attributed to the shortening of kinetochore microtubules. An alternative hypothesis is that thermal fluctuations of the pericentric loops observed as radially displaced foci (Figure 1.1), anchored by condensin along the central spindle can generate an outward/poleward force (Panyukov et al., 2009a). This tension force would be generated via fluctuations of chromatin loops that repel one another as a consequence of their crowding (Panyukov et al., 2009a; Panyukov et al., 2009b). The repulsion of the loops is balanced by the

inward/anti-poleward entropic spring force of the chromatin along the primary axis. The extension of the chromatin along the primary axis is an entropically disfavored state, resulting in a net inward force seeking to collapse the chromatin into a random coil. In vivo, the balance of the loop's outward repulsive force and the primary axis' inward spring force generates the tension between sister centromeres. To distinguish microtubule shortening from crowding-based extension, microtubule dynamics were suppressed with benomyl and the length of the TetR-GFP signal of the dicentric plasmid along the primary axis was quantitated. The fraction of stretched (parallel $1.2\times$ > perpendicular) chromatin is largely insensitive to benomyl treatment in cells with short spindles (% stretched \pm benomyl Figure 1.4, D; 35% vs 28% stretched in spindles 0.5 to 1.0 μm Table 1.7). Likewise, chromatin stretch length is insensitive to spindle length up to 2.0 μm (chromatin stretch length: WT 630 nm, benomyl 637 nm, binning 0.5 μm to 2.0 μm spindles, Table 1.7). Thus, dynamic microtubules are not required for chromatin extension. Repulsion between pericentric loops can generate sufficient force to release or unwrap several nucleosomes.

Spindle length is dependent on microtubule dynamics and growth, and lengths much beyond 2 μm in metaphase are not observed in benomyl treated cells. Likewise, the fraction of stretched dicentric chromatin fibers is reduced upon benomyl treatment, 45% to 16% in spindles 1 – 1.5 μm , and 65% to 29% in spindles 1.5 -2.0 μm (Figure 1.4 D, Table 1.7). The fraction and magnitude of chromatin stretching is microtubule-independent on length scales < 1 μm , but microtubule-dependent in spindles > 1 μm . The limited length scale of repulsive forces is consistent with the short length scales of polymer crowding models for generating extensional forces (Bloom, 2014).

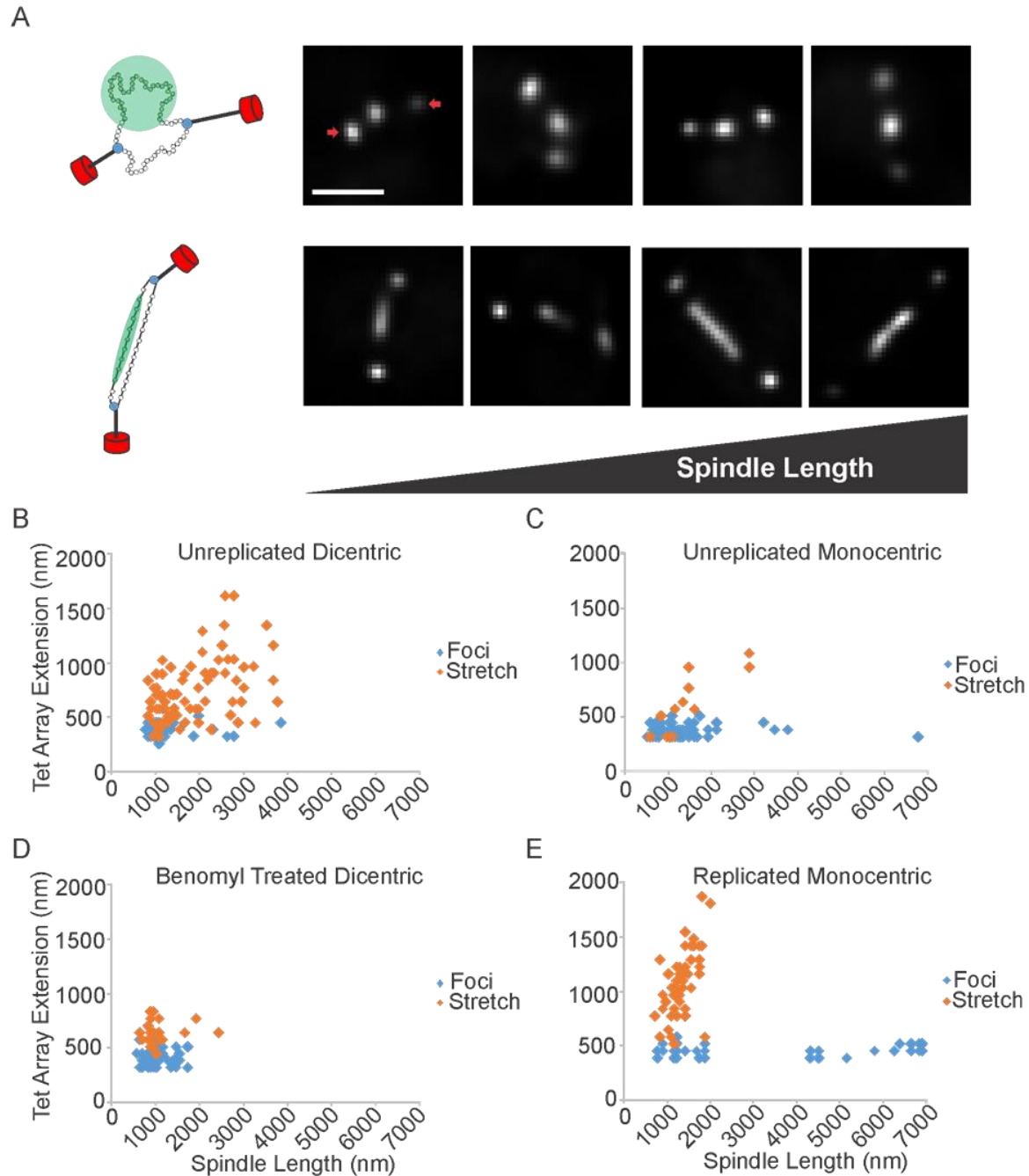


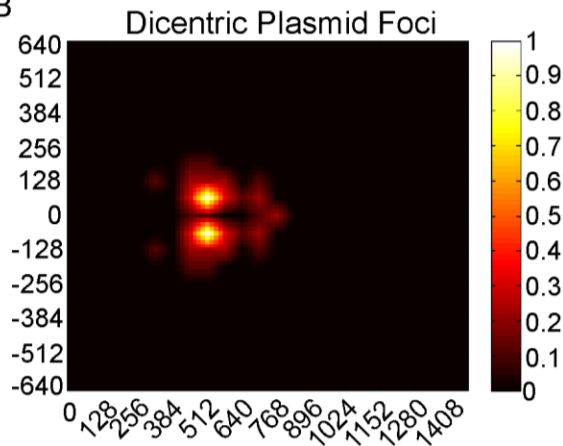
Figure 1.4 – Tension along the spindle axis is sufficient to release nucleosomes

(A) Left, schematic of dicentric plasmid. The plasmid is attached to kinetochore microtubules (kMTs, black) via the kinetochore (blue). Nucleosomes are green, SPBs are red. The DNA appears as a near-diffraction spot (green circle, top) or a filament (green bar, below). Right four panels, deconvolved images of near-diffraction foci (top) and filaments (below) of dicentric plasmids. SPBs are indicated by arrows. TetO/TetR-GFP extension vs spindle length for unreplicated dicentric ($n = 129$ arrays) (B), unreplicated monocentric ($n = 102$ arrays) (C), benomyl treated dicentric ($n=92$ arrays) (D), and replicated monocentric plasmids ($n=94$ arrays) (E). Scatter plots display population data from multiple experiments. Scale bar = 1 micron.

A

	Foci (n = 33)	Stretched All Spindle Lengths (n = 31)	Stretched Spindles < 2 μ m (n = 20)	Stretched Spindles > 2 μ m (n = 11)
Average Radial Displacement (nm)	78 \pm 49	47 \pm 49	64 \pm 50	17 \pm 29
Average Axial Displacement (nm)	436 \pm 108	684 \pm 353	455 \pm 112	1100 \pm 246

B



C

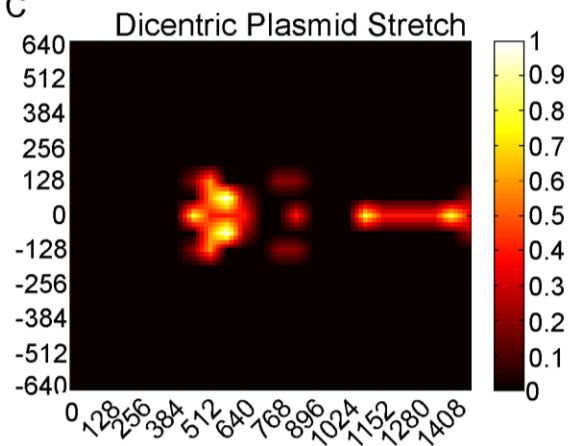


Figure 1.5 – Heat map analysis of unreplicated, dicentric plasmids

(A) Table summarizing the average radial and axial displacement of the TetR-GFP signals that appear as foci or elongated filaments. Heat maps of TetR-GFP signals that appear as foci (B) and elongated filaments (C).

Table 1.7 – Frequency and magnitude of elongated TetR-GFP signals

Spindle Length (μm)	Unreplicated Dicentric Plasmid (n = 129)			Unreplicated Monocentric Plasmid (n = 102)			Unreplicated Benomyl, Dicentric Plasmid (n = 92)			Replicated Monocentric Plasmid (n = 94)		
	N	Stretch Frequency (%)	Stretch Length (nm)	N	Stretch Frequency (%)	Stretch Length (nm)	N	Stretch Frequency (%)	Stretch Length (nm)	N	Stretch Frequency (%)	Stretch Length (nm)
0.5-1.0	20	35%	587 ± 165	27	11%	384 ± 91	47	28%	645 ± 105	11	55%	892 ± 215
1.0-1.5	60	45%	634 ± 171	49	10%	653 ± 212	38	16%	597 ± 95	46	72%	1000 ± 237
1.5-2.0	14	65%	648 ± 185	18	6%	576	7	29%	704 ± 64	20	75%	1342 ± 292
>2.0	35	86%	1252 ± 378	8	25%	1024 ± 64	NA	NA	NA	17	0%	NA

Extended chromatin promotes tension-based kinetochore microtubule rescue

Chromatin forces along the spindle axis will be transmitted through the kinetochore to the attached microtubule. The dicentric plasmid provides a unique opportunity to correlate chromatin extension with kinetochore microtubule length. 80% of DNA between the two centromeres (5.5/7 kb) is labeled with TetR. When the plasmid is extended along the spindle axis, the distance between the Tet array and the spindle pole body provide an estimate of kinetochore microtubule length (Figure 1.6 A-D). In cells containing the unreplicated dicentric plasmid, chromatin extension is constant, while kinetochore microtubules lengthen as a function of spindle length (Figure 1.6 A, C, E). In cells where a monocentric plasmid (pT323), the parent plasmid of the dicentric (pT431) (Dewar et al., 2004), has replicated, chromatin extension increases, while kinetochore microtubule length is constant as a function of spindle length (Figure 1.6 B, D, F). Thus, more compact the DNA (e.g. looped), the more tension is exerted at the microtubule plus-end, promoting the growth state. In contrast, if there is sufficient DNA extension (2X the DNA length in a replicated plasmid), less tension is exerted at the microtubule plus-end, and the microtubules shorten. These results highlight the interplay between chromatin length and kinetochore microtubule state. Kinetochore dynamics are not the sole drivers of tension, rather the chromatin and its length regulation can dictate microtubule dynamics. Limiting the length of the DNA in the unreplicated plasmid keeps tension constant, and at a level sufficient to drive kMT growth. Limiting DNA length in the unreplicated plasmid keeps tension constant, and at a level sufficient to drive kMT growth (Figure 1.6).

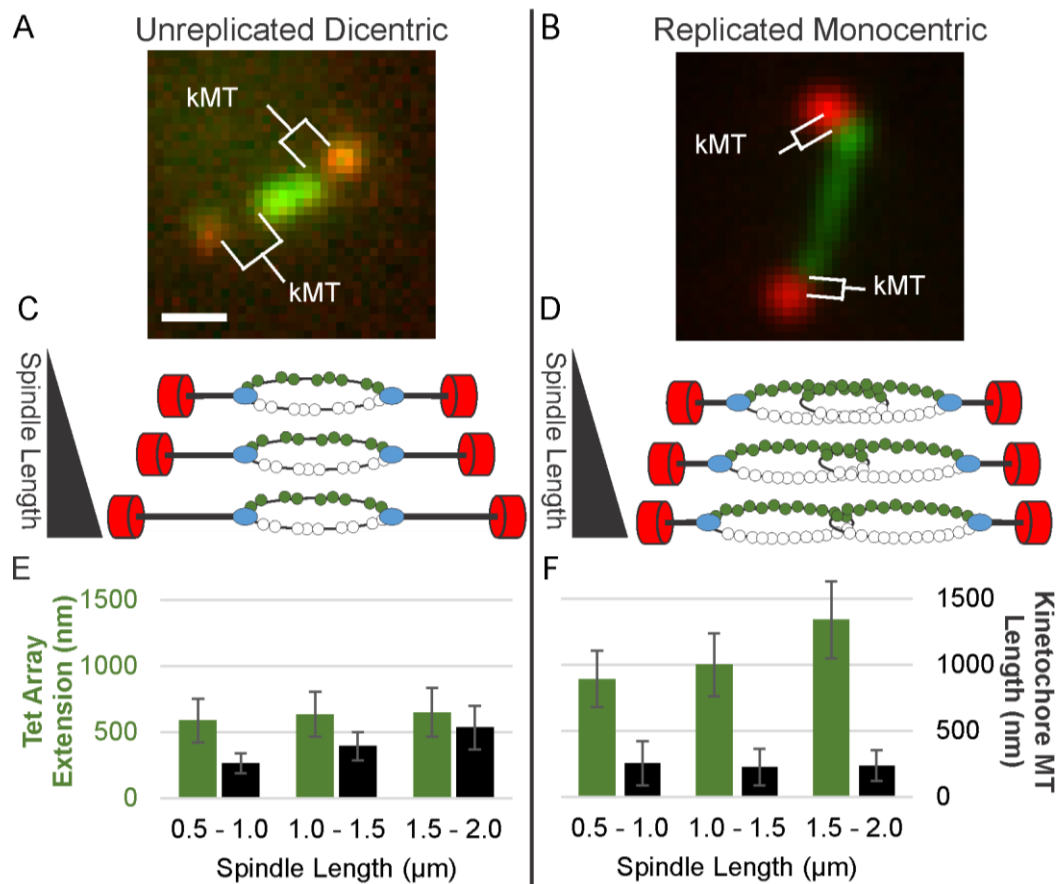


Figure 1.6 – Tension along the spindle axis promotes microtubule growth

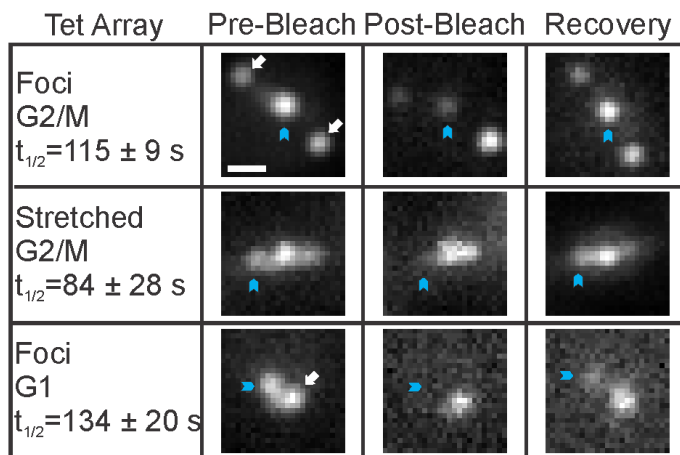
TetO array extension and kMT length in unreplicated, dicentric plasmids vs replicated, monocentric plasmids. Image of metaphase yeast containing an unreplicated, dicentric plasmid (A) and a replicated, monocentric plasmid (B). Schematic of a spindle containing an unreplicated, dicentric plasmid (C) and a replicated, monocentric plasmid (D). SPBs are in red, kinetochores are in blue, and DNA in green. TetO array extension and kMT length vs spindle length for unreplicated, dicentric plasmids (E) and for replicated, monocentric plasmids (F). Scale bar = 0.5 microns. Error bars are standard deviation. The data shown are from multiple experiments (Dicentric $n = 43$ arrays, Replicated Monocentric $n = 54$).

Increased tension on chromatin proximal vs. displaced from the spindle axis

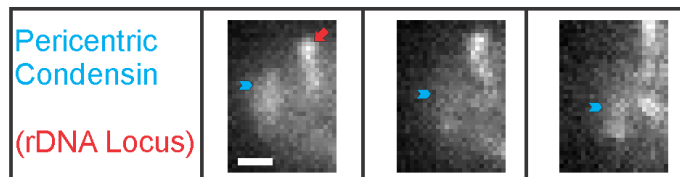
An alternative approach to demonstrate multiple tension regimes in the pericentric chromatin is the ability to measure turnover of the DNA binding proteins. Mechanical tension can reduce the half-life ($t_{1/2}$) of DNA factor binding (Blumberg et al., 2005), disrupt nucleosomes in vitro (Brower-Toland et al., 2002) and in vivo (Figure 1.4) (Thrower and Bloom, 2001). We determined the $t_{1/2}$ of TetR-GFP bound to TetO using fluorescence recovery after photobleaching (Figure 1.7 A). The $t_{1/2}$ of TetR-GFP bound to the TetO array in the compact loop configuration was $115 \pm 9''$ in G2/M cells. TetR-GFP binding to stretched dicentric plasmids was more rapidly exchanged with a $t_{1/2}$ of $84 \pm 28''$ ($P = 0.01$, compared to G2/M foci). The $t_{1/2}$ was $134 \pm 20''$ for cells in G1 in cases where the dicentric chromosome is attached but under no tension (Figure 1.7 A).

During metaphase pericentric condensin is enriched along the spindle axis while pericentric cohesin is radially displaced from the spindle axis (Stephens et al., 2011), (Yeh et al., 2008). Pericentric cohesin shows little recovery after photobleaching (Yeh et al., 2008). Condensin showed $\geq 30\%$ recovery after photobleaching in $\sim 20\%$ WT cells at the pericentric and rDNA loci (Figure 1.7 B, C). Yeast lacking Mcm21 have decreased levels of pericentric cohesin which results in increased extension of pericentric chromatin (Stephens et al., 2011). In *mcm21 Δ* mutants, condensin showed $\geq 30\%$ recovery in $\sim 60\%$ of cells at the pericentric locus and $\sim 20\%$ at the rDNA locus. Thus, chromatin extension results in an increased turnover rate of DNA binding proteins, indicative of an increase in tension proximal to the spindle axis.

A



B



C

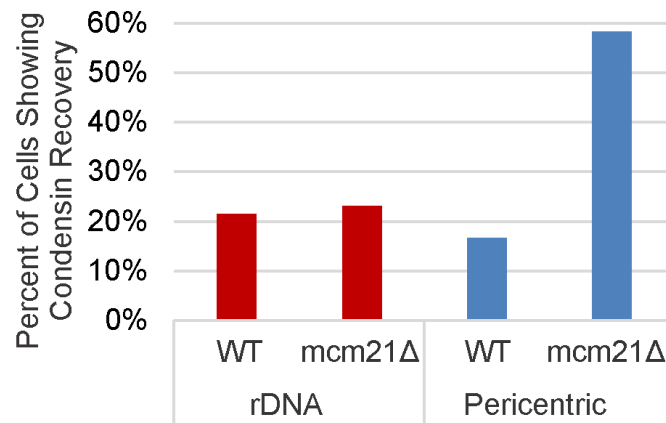


Figure 1.7 – Higher DNA binding protein turnover proximal to the spindle axis

FRAP analysis of TetR-GFP and condensin. (A) Representative images of dicentric plasmids Pre, Post, and 2-4 minute after photobleaching. Blue arrowhead marks the bleached TetR-GFP spot. SPBs are indicated by white arrows. Scale bar = 0.5 micron. (B) Images of condensin Pre, Post, and 5 minutes after photobleaching. Blue arrowhead indicates the bleached condensin bound to pericentric DNA. Red arrow indicates condensin bound to the rDNA locus. Only pericentric condensin was bleached in the cell shown. Scale bar = 0.5 microns. (C) The percentage of cells showing recovery of condensin bound to the pericentric and rDNA loci in WT and mcm21Δ cells 10 minutes after bleaching. Recovery threshold is 30% of the original corrected signal. Each data set summarizes multiple experiments (WT rDNA n = 14, mcm21Δ n = 13, WT Pericentric n = 12, mcm21Δ Pericentric n = 12 cells).

Discussion

The dynamics and configurational state of pericentric chromatin leads to a fundamental new model for the function of a eukaryotic centromere. Centromere proximal DNA loops ~10 kb in length are bound by condensin at their base (Snider et al., 2014) and extend radially from the spindle axis in metaphase (Figure 1.8 A) (Stephens et al., 2011; Stephens et al., 2013). Visualization of pericentric DNA loops via TetR-GFP bound to TetO array, reveals random fluctuations that explore an area larger than expected from thermal force, but consistent with energy from randomly directed, non-thermal, ATP-dependent sources. Using benomyl treatment and Stu2 depletion to dampen microtubule dynamics we show that only a fraction of motion (<20%) can be attributed to microtubule-based directional force. The DNA loops fluctuate into random coils and are constantly being jostled by neighboring loops. In three dimensions this means that sister chromatids are not constrained to a linear position between sister kinetochores. The appearance of sister chromatids perpendicular to the spindle axis have been reported in the literature and constitute 30% of the configurational states upon depletion of condensin (Figure 1.2 C, Figure 1.8 C) (Snider et al., 2014). The motion analysis of the loops reveals two important features. The perpendicular foci exhibit virtually no directed motion, expected if they remain constrained at their bases and extended from the axis. Second, the foci move independently, each loop moving around the axis. Protein turnover is slower on these off-axis loci, consistent with a more relaxed configurational state (Figure 1.7).

In wild-type cells the loops undergo a configurational state change from a larger than diffraction spot to an extended filament that is aligned with the spindle axis (Figure 1.4, Figure 1.5) (Stephens et al., 2011). Chromatin extension provides a quantitative measure of nucleosome occupancy where the two ends of DNA are accounted for in vitro. For the in vivo measurement, two centromeres on the same dicentric molecule are attached to microtubules and the intervening DNA visualized by TetR-GFP bound to the intervening TetO array. Unlike the radial displaced spots, chromatin on the spindle axis appeared highly extended, well beyond nucleosome packing. On average, 6 nucleosomes were released (out of 35 total, 5.5 kb/160 bp) on chromatin proximal to the spindle axis during metaphase (spindle length 1.0 – 2.0 μm). The estimates of the force threshold for nucleosome release range from 3-5 pN in the presence of cell extract to 20 pN in the absence of cell extract (Brower-Toland et al., 2002; Yan et al., 2007).

Nucleosomes for biophysical studies are often assembled on DNA that has been selected for strong nucleosome positioning. The advantage for the in vitro experiment is in knowing the number of nucleosomes with some certainty. Nucleosomes are assembled on lacO arrays introduced into yeast (Thrower and Bloom, 2001), but they are not positioned with respect to sequence, and are not likely bound with the same affinity relative to the 601 bp sequence used in in vitro experiments (Lowary and Widom, 1998). However, the conformational state and the release of nucleosomes are indicative of higher tension relative to adjacent off-axis chromatin. The increased turnover of DNA-binding proteins is an independent indicator that the extended chromatin is subject to higher tension (Figure 1.7). These strands along the axis are not rigid, as evidenced by the change in angular distribution relative to the spindle axis (Figure 1.9). Thus, extended fibers are still subject to the random jostling and pushing from the close packing of neighboring strands.

A unique feature of the dicentric plasmid is that almost all of the DNA between sister centromeres is bound by TetR-GFP (Figure 1.6). Consequently, we are able to track the growth and shortening of a single kinetochore microtubule in a living cell. As the spindle elongates, the kinetochore microtubule grows without further extension of chromatin (Figure 1.6 A). Microtubules are dynamically unstable and tension at the plus-end rescues them from the shortening state and promotes polymer growth. The extended chromatin spring of the single dicentric plasmid is stiff enough to promote microtubule growth. It is noteworthy that the chromatin does not continue to extend upon spindle growth during metaphase. In late anaphase, we have demonstrated that the DNA can extend to its B-form length ($1\ \mu\text{m}/3.3\ \text{kb}$) (Thrower and Bloom, 2001). Thus, there is no physical constraint to extension beyond the loss of 6-8 nucleosomes out of 35 upon anaphase onset. The loop organization is dynamic, chromatin can flow toward the spindle as evidenced in the replicated plasmid situation (Figure 1.6 B). In this case, the two centromeres are on individual molecules and as the spindle elongates, the amount of DNA proximal to the spindle increases based on length of the Tet array (Figure 1.6 B). The constraint on extension of the dicentric plasmid most likely reflects the force balance between the chromatin spring and microtubule based extensional forces. The unfolding of chromatin beyond the nucleosome length reaches an equilibrium state where ~50% of the length is nucleosomal ($29\ \text{nucleosomes} \times 11\ \text{nm} = \sim 320\ \text{nm}$) and ~50% is B-form length DNA (release of 6 nucleosomes $160\ \text{bp} \times 6 \times 0.33 = 320\text{nm}$).

The chromatin spring is not completely dependent on microtubules, based on the properties of the extension observed in the presence of benomyl (Figure 1.4 and Table 1.7) and the separation of pericentric chromatin in a kinetochore-disrupted, *ndc10-2* mutant at restrictive temperature (Figure 1.3 D). Rather it is interactive with the microtubules, due to the physical effects of the chromatin loops attached to the primary axis. The remarkable feature of the centromere is that it resembles a particular type of branched polymer called a “bottle brush” (Fig 1.8 A) based on the heterogeneity of stress distribution within the centromere. Tension is generated along the primary brush axis (known as tension amplification) created by the collective effect of steric repulsion of the side chains resisting the inward/anti-poleward spring force of the primary axis seeking to collapse into a random coil. The individual side chains themselves are shielded from this tension and fluctuate thermally (Panyukov et al., 2009a). The extensional force of radial loops on the primary axis explains how sister chromatids could be held apart in the absence of spindle-based force in the *ndc10-2* mutants where the kinetochores have been compromised (Figure 1.3 D). Unlike a simple bottle brush polymer, the centromere can alter the density of side-loops of chromatin through loop “popping” and reforming, consistent with the presence of chromatin remodeling factors such as RSC and SWI/SNF at the centromere (Hsu et al., 2003; Xue et al., 2000) (Figure 1.8 D). The dynamic nature of the chromatin loops allows the centromere to act as a molecular “shock-absorber”. A stationary bottle-brush polymer will have an equilibrium configuration when all forces are balanced. However, the centromere is non-stationary with active, stochastic forces acting along the primary axis from microtubule dynamics. This creates a variation in force balance in which the primary axis of pericentric chromatin is occasionally under an enhanced tensional load because of microtubule shortening. The tensile load is initially relieved when a loop “pops”, effectively lengthening the primary axis while decreasing the side loop density. The newfound slack in the primary allows microtubule shrinkage to occur. Once the microtubule grows again the slack can be taken up by a chromatin loop reforming. This coupling of structure and force conspires to maintain a dynamic tensile balance within the chromatin during mitosis. The centromere is thus a molecular shock absorber that can modulate its length and stiffness to buffer the stochastic effects of microtubule dynamics.

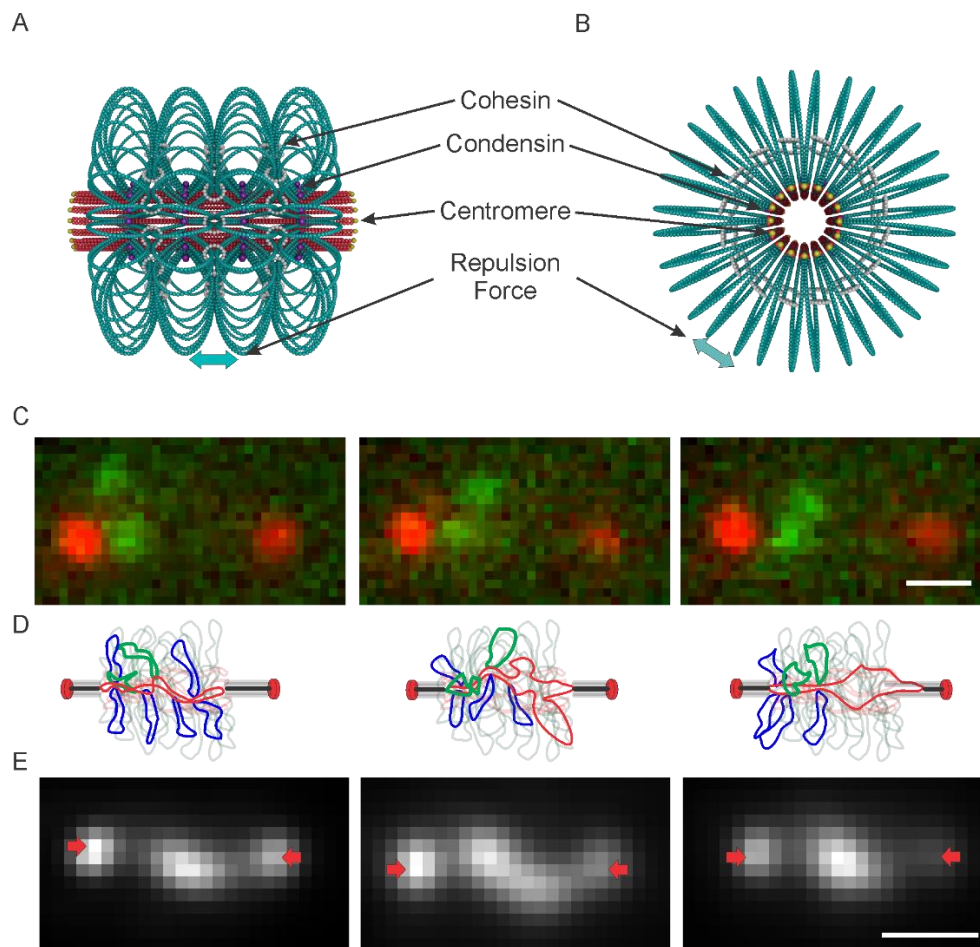


Figure 1.8 – Mechanistic basis for extensional forces from packed centromere DNA loops

(A) Model of pericentric chromatin in budding yeast. The pericentric chromatin from all 16 chromosomes is shown. 50 kb of DNA (red and teal) surround the centromeres, shown at the apex of a DNA loop (centromere DNA in yellow, DNA primary-axis in red) and form a cylinder around the spindle microtubules (not shown). Sister centromeres are at opposite ends of the cylinder. DNA loops (teal) are formed via the action of condensin (purple) binding to the base of loops. The number of loops and their geometric arrangement are based on experimental evidence from the spatial segregation of condensin, cohesin and LacO DNA arrays. The loops repel each other, resulting in a net outward/poleward force. Cohesin rings are depicted in white. (B) End-on view of the model. (C) Timelapse of pericentric LacO arrays in *cbf5-AUU* mutant yeast during metaphase. (D) Schematic of sister chromatid loop fluctuations (in green) over time. SPBs (red ovals), lines are KMTs. Chromatin proximal to the spindle axis is indicated as the red line, loops extending off axis are indicated in blue. The green loops depict the labeled chromatin in (C). Microtubule shortening will release condensin bound at the base of a loop as the DNA transits from a radial to an axial position (read panels left to right). The release of a loop results in a precipitous drop in tension due to increase DNA length along the axis. As the microtubule shortens, DNA (red) elongates along the spindle axis, until it reaches equilibrium and greater force is required to further stretch the fiber. This leads to tension-dependent microtubule rescue, allowing the DNA to recoil and adopt a random coil. DNA fluctuation off the spindle axis allows condensin binding and loop formation (read panels right to left). (E) Timelapse of TetO/TetR-GFP labeled, dicentric plasmid. These plasmids lie along the primary axis, where tension force is sufficient to extend the chromatin beyond its nucleosomal length. SPBs are indicated with arrows (red). Scale bar = 0.5 microns.

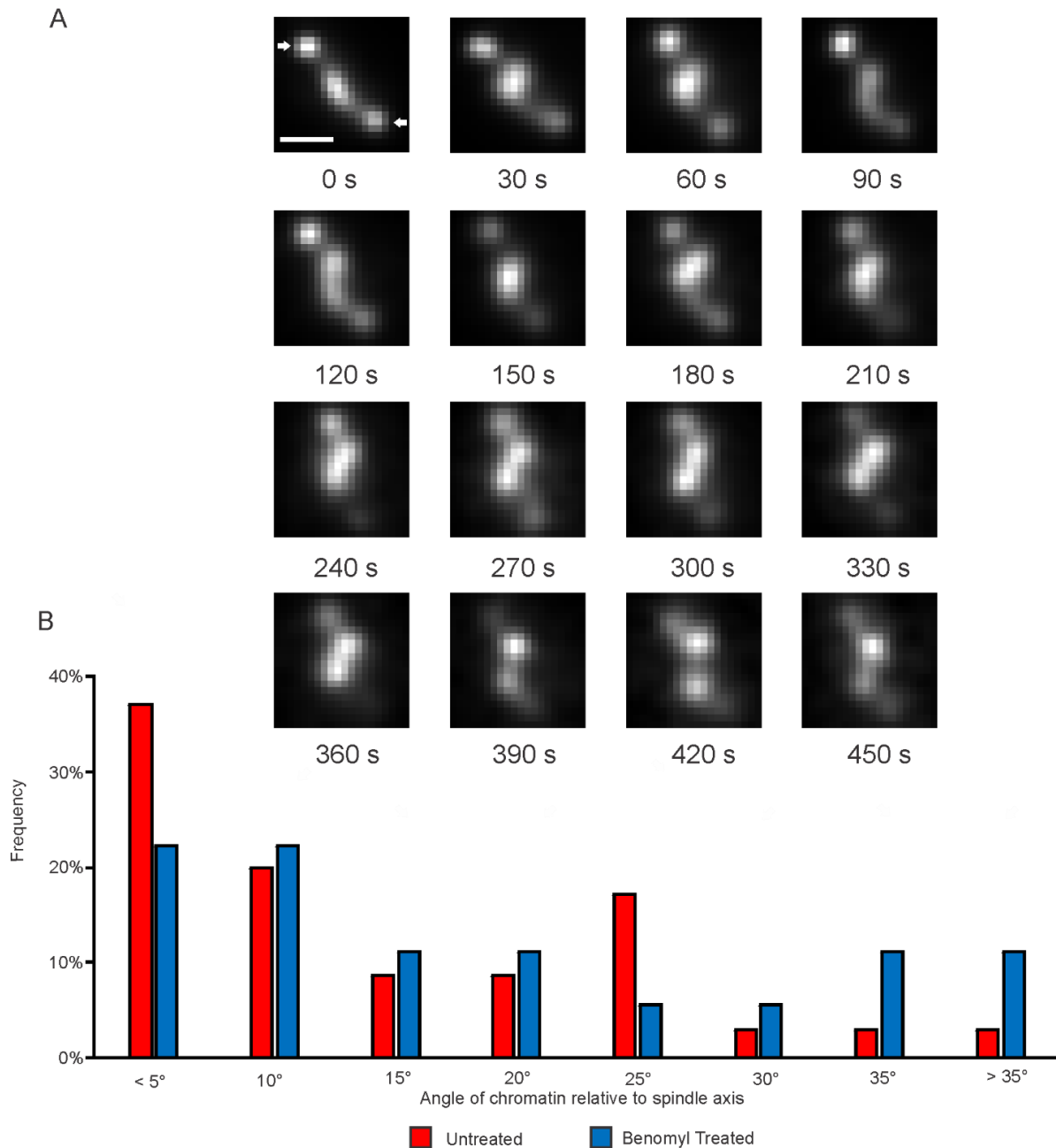


Figure 1.9 – Fluctuation and trajectory of dicentric plasmids relative to the mitotic spindle axis

(A) Fluorescent images of configurational states of the dicentric plasmid in metaphase. Deconvolved single-plane images of cells containing a single dicentric plasmid at 30s intervals over 450s are shown. Spindle poles appear as diffraction-limited spots indicated with arrows. Scale bar = 0.5 microns. (B) Angular distribution of elongated dicentric plasmids in 0.5 to 1.8 μ m spindles from individual cells in a population. Angles represent the difference between the trajectories of the primary chromatin axis relative to the spindle axis (defined by the two spindle poles, indicated with arrows). The percentages are calculated using data from multiple experiments (Untreated n = 35 arrays, Benomyl Treated n = 18 arrays). Red, untreated; blue, benomyl treated.

Materials and Methods

Strain and construct information

The detailed genotypes and mutations of each strain are listed in table IV. For KS406 and KBY8065 the lac operon arrays (Straight et al., 1996) were targeted adjacent to the Rad16 promoter (467,248, Chromosome 2) (Lobachev et al., 2004) and ~1 kb to the left of CEN15 (325,382 – 326,687) (Goshima and Yanagida, 2000) respectively. For KBY2157 and Y589 (Stu2CU) the lac operon array was targeted to the MET14 locus (438,816 – 439,365) using PCR fragments from pLKL60Y, which contains a 32 mer (1.2 kb in length) of the lac operator with a G418-resistance marker (Pearson et al., 2001). For KBY9533.1 the pLKL60Y-derived lac operon array was targeted to 12.7 kb from CENXI (440,246 – 440,129) (Pearson et al., 2001). The LacI-GFP used to visualize the lac operators is a fusion protein of GFP, a truncation of the LacI gene lacking the final 11 C-terminal amino acids to prevent tetramerization, and a nuclear localization signal (NLS) (Straight et al., 1996).

T2755, JLY1018.1, and T3000 were derived from yeast strain T2726, a derivative of the W303 yeast strain containing a *Zygosaccharomyces rouxii* R recombinase gene under the control of the MET3 promoter, a TetR-GFP-NLS under the URA3 promoter (Michaelis et al., 1997), and SPC42-YFP C-terminal fusion protein (He et al., 2000). JLY1018.1 was derived from T2755 by swapping the SPC42-YFP for a SPC42-RFP:KAN using chimeric PCR primers with homology to SPC42 and pKS390 (pFA6a-mCherry-kanMX6) (Wach et al., 1997). The monocentric plasmid pT323 was made by inserting two recombination sites, from pHM401 (Araki et al., 1992), using XhoI and HindIII cut sites, and a tet operon array (112 repeats) into a BamHI cut site of YCp50 (GenBank X70276) (Tanaka et al., 2002). The dicentric plasmid pT431 was made by cloning a fragment of CEN4 (730-bp DNA containing CDEI-II-III) under control of the GAL1-10 promoter into pT323 (Dewar et al., 2004).

Y589 (Stu2CU) was derived from a strain that upon the addition of copper (CuSO₄) there is simultaneous repression of STU2 mRNA synthesis and degradation of Stu2 (Kosco et al., 2001). KBY2157 was derived from a strain containing an *ndc10-2* mutation (Kopski and Huffaker, 1997). For *cbf5-AUU* the AUG start codon was mutated to AUU (Kendall et al., 2000; Snider et al., 2014). SMC3-

GFP and SPC29-RFP are C-terminal fusions of Smc4 to GFP and Spc29 to RFP respectively (Stephens et al., 2011). The *mcm21*, *ura3*, and *nat* gene deletions were performed using chimeric PCR primers with homology upstream and downstream of the gene to be deleted and the pFA6a plasmid series (Wach et al., 1997). Bub1 was deleted by transforming with the pTR92 plasmid (Roberts et al., 1994).

Table 1.8 – Strain number and genotypes of yeast strains

Strain Number	Genotype
KS406	MAT α CEN2(240kb)-GFP[10kb] ade5-1, trp1-289, ura3 Δ , leu2-3, 112, lys2::insI-Sce1, lacO array next to RAD16 promoter, tetO array next to LYS2 promoter, arg4::hisG Gal1/10 I-Sce1, thr1::HISpLacI-GFP:Nat, ade1::URApTetR-CFP:Hyg, Spc29-RFP:Bsd
KBY8065	MAT α CEN15(1.8)-GFP[10kb] ade2-1, his3-11, trp1-1, ura3-1, leu2-3,112, can1-100, LacINLSGFP:HIS3, lacO::URA3, Spc29-RFP:Hyg
T3000	W303 MAT α ; (T2726 carrying pT431-URA3 (2xCEN, 2xRS)) trp1::MET-Recombinase::TRP leu2::TetR-GFP::LEU2 spc42::Spc42-YFP:HIS3
T2755	W303 MAT α , (T2726 carrying pT323-URA3 (1xCEN, 2XRS)) trp1::MET-Recombinase::TRP leu2::LEU2::tetR-GFP spc42::Spc42-YFP::HIS3
JLY1018.1	W303 MAT α , (T2726 carrying pT323-URA3 (1xCEN, 2XRS)) trp1::MET-Recombinase::TRP leu2::LEU2::tetR-GFP spc42::Spc42-RFP:kan
KBY9533.1	MAT α ade1 met14 ura3-52 leu2-3,112 lys2 Δ ::lacI-GFP-NLS-NATr his3-11,15 12.5 kb XI::lacO-KANMX Nat Δ ::His3MX6, Spc29-RFP-Hb, cbf5-AUU-Nat
KBY2157	MAT α his3-delta200, leu2-3,112 ura3-52 Gal+, ndc10-2, met14::lacO:KAN, lys2::lacI:GFP:NAT, Spc29-CFP::Hb
MAY8602	MAT α LacINLSGFP:HIS3 lacO::URA3(1.8kb from CEN15) Spc29RFP:Hb ura Δ :TRP bub1 Δ :URA
Y589 (Stu2 ^{CU})	MAT α Ace1-UBR1 Ace1-ROX trp1-D1 ade2-101 ura3-52 lys2-801 stu2-D::URA3::pAnb1UB-R-STU2 lacO32::KANr::met14 LacI-GFP-NAT
KBY9035.1	(YEF 473a) Smc4-GFP-Kan, Spc29-RFP-Hb
KBY9097.1	(YEF 473a) Smc4-GFP-Kan, Spc29-RFP-Hb, mcm21D-Nat

Cell preparations and drug treatments

Cell strains KBY2157, KBY8065, KS406, KBY9035.1, KBY9097.1, KBY9533.1, MAY8602, and Y589 (Stu2CU) were grown to logarithmic phase at 24° C in rich YPD media with 0.5 mg additional adenine per mL of media. Strain KBY2157 (ndc10-2 temperature sensitive mutation) was shifted to 37° C in SD-HIS media at least four hour prior to imaging. Cells containing the dicentric (T3000) or monocentric (T2755) plasmids were grown to logarithmic phase at 24° C in YCAT-galactose media with 0.5 mg of additional adenine and methionine per mL of media. Four hours before imaging cells were washed with ddH₂O and resuspended in SG (synthetic -containing galactose) media lacking methionine to induce loss of the origin of replication as described by Dewar et al., (Dewar et al., 2004). Twenty minutes before imaging cells were resuspended in YPD at 24° C to repress transcription from the GAL1 promoter and activate the conditional centromere (Dewar et al., 2004). Prior to imaging the replicated monocentric plasmid, strain JLY1018.1 was grown to logarithmic phase at 24° C in YCAT-glucose media with 0.5 mg additional adenine per mL of media. For benomyl treatment, a 10 mg/mL stock of benomyl was added directly to growth media so that the final concentration was 55 or 85 μ M. For strains KBY8065, KS406, and Y589 (Stu2CU) cells were incubated with benomyl for 1 hour before imaging. For strains T3000 and T2755, cells were incubated with benomyl for at least 30 minutes during their YPD incubation. For ATP depletion, sodium azide and deoxy-glucose were added to YC-complete lacking sugar with 0.5 mg additional adenine per mL of media to a final concentration of 0.02% and 1 μ M, respectively. Cells were washed and resuspended in YC-complete, sodium azide, deoxy-glucose media and incubated at 24° C for 20 minutes prior to imaging. To deplete Stu2p in Y589 (Stu2CU) cells, cupric sulfate (CuSO₄) was added to growth media to a final concentration of 500 μ M for four hours prior to imaging as described in Kosco et al. (2001). All cells were imaged in media with the final concentration of drug added.

Microscopy

Population images of JLY1018.1 and ten minute timelapse images for MSD and variance analysis for strains KBY8065 and KS406 were acquired every 30 seconds at RT (25° C) using a Nikon Eclipse Ti wide-field inverted microscope with a 100x Apo TIRF 1.49 NA objective (Nikon, Melville, New York, USA) and Andor Clara CCD camera (Andor, South Windsor, Connecticut, USA) using Nikon NIS Elements imaging software (Nikon, Melville, New York, USA). Timelapse stacks contained 7 Z-plane sections with

400 nm step-sizes. Five minute timelapse images for kymographs, directed motion analysis, and SCI analysis were acquired every 3-4 seconds using the same imaging setup as described above for KBY8065, KBY9533.1, Y589 (Stu2CU), and MAY8602. Images of T3000, T2755, KBY9533.1 and KBY2157 were acquired at RT (25°C) using a Nikon Eclipse E600FN microscope with a 100x Plan Apo TIRF 1.45 NA objective (Nikon, Melville, New York, USA) and Hamamatsu ImagEM EM-CCD digital camera (Hamamatsu, Photonics, Bridgewater, NJ) with a custom Lumencor LED illumination system (Lumencor Inc., Beaverton, OR, USA) using MetaMorph 7.7 imaging software (Molecular Devices, Sunnyvale, CA, USA). Single stacks contained 7 Z-planes sections with 300 nm step-size. Population images of KBY9533.1 images were taken on an inverted, widefield microscope (Eclipse TE2000-U; Nikon) with a 100x Plan Apo 1.4 NA digital interference contrast oil emersion lens with an Orca ER camera (Hamamatsu Photonics, Bridgewater, NJ) using MetaMorph 6.1 software at RT (25°C). All strains were imaged in YC complete media with 2% filter sterile glucose added, except for condensin containing strains (KBY9035.1 and KBY9097.1) which were imaged with YC complete media lacking glucose.

Radii of confinement

All LacO/LacI-GFP and spindle pole body foci were tracked using the Speckle Tracker program in MATLAB (The Mathworks, Natick, MA, USA) (Wan et al., 2012; Wan et al., 2009). Speckle Tracker is a graphical user interface that detects GFP and RFP foci in a digital image file, tracks the foci through the timelapse images, determines the centroids of the signals by fitting a 2D Gaussian function to a 5x5 pixel region using MATLAB's nonlinear curve-fitting methods (lsqcurvfit), and exports the subpixel X and Y coordinates to an Excel (Microsoft, Redmond, WA, USA) spreadsheet. Radii of confinement and effective spring constants in Figure 1 and Table I were calculated as described in (Verdaasdonk et al., 2013) prior to coordinate rotation. A custom PERL script was used to parse the coordinates generated by Speckle Tracker, convert the coordinates from pixels to nanometers, subtract the coordinates of the proximal pole from the lacO/LacI-GFP coordinates, subtract the mean position of the resulting lacO/LacI-GFP coordinates, calculate the mean squared displacement (MSD) of each timelapse, and export the MSDs and coordinates to Excel spreadsheets. Radii of confinement using MSD curve plateau values were calculated using $R_c = \frac{5}{4} * \sqrt{MSD_{plateau}}$, where $MSD_{plateau}$ is the average plateau value, calculated manually in Excel by averaging the MSD values at time steps 330, 360 and 390 seconds, of the MSD

curves generated by the PERL program. Effect spring constants using MSD curve plateau values were calculated automatically using a custom MATLAB program using the equation $k_s = \frac{2k_bT}{\langle MSD_{plateau} \rangle - \langle \Delta r_0^2 \rangle}$, where k_b is the Boltzmann constant, T is temperature (Kelvin), and $MSD_{plateau}$ is the average plateau value. Radii of confinement using positional variance σ^2 were calculated using $R_c = \frac{5}{4} * \sqrt{(2\sigma^2 + \langle \Delta r_0^2 \rangle)}$, where σ^2 is the variance of the distribution of foci positions calculated by $\sigma^2 = \text{mean}(\sigma_x^2, \sigma_y^2)$. The variance in X and Y are calculated by fitting the pole and mean subtracted coordinates generated by the PERL script to a normal distribution using MATLAB's normfit function. The average squared deviation from the mean position $\langle \Delta r_0^2 \rangle$, is calculated $\langle \Delta r_0^2 \rangle = \langle \Delta x_0^2 \rangle + \langle \Delta y_0^2 \rangle$. Effective spring constants were calculated using $k_s = \frac{k_B T}{\sigma^2}$, where k_b is the Boltzmann constant, T is temperature (Kelvin), and σ^2 is the variance of the distribution of foci positions. For variance-based (σ^2) equations, both the population distribution and the average individual cell distributions were calculated for comparison. Population, variance-based equations were calculated manually in MATLAB, while individual R_c and k_s values were calculated by a custom MATLAB script. Radii of confinement and spring constants calculated by population variance were compared using Levene's Test in MATLAB. The coordinates of LacI-GFP were rotated to set the spindle axis to the X axis using a custom MATLAB program. One dimensional R_c values were calculated from rotated coordinates using $R_c = \frac{5}{2} * \sqrt{\sigma^2 + \langle \Delta r_0^2 \rangle}$ where σ^2 is the variance of the distribution of positions in one dimension, and $\langle \Delta r_0^2 \rangle$ is the average squared deviation from the mean position.

Kymograph, directed motion, and SCI analysis

Kymographs were generating using MetaMorph 7.7 software without background subtraction using the maximum intensity setting from single-plane timelapses. Kymograph showing parallel motion captured both GFP/RFP foci in a single kymograph. Kymographs showing perpendicular motion contain only a single focus. Image rotation to align spindle axis with the X-axis was performed using a custom MATLAB program. Directed motion analysis using minimum displacement and minimum rate criteria was performed by tracking the GFP and RFP foci in the images using the MATLAB program Speckle Tracker (Wan et al., 2012; Wan et al., 2009) and then analyzing the resulting coordinates using a custom MATLAB program. SCI analysis was performed on the coordinates using a custom Python script.

Directed motion analysis for the Stu2CU strain was performed using the distance between the GFP foci with a minimum rate of 20 nm/s and a minimum displacement of 300, 350, or 400 nm. To test the GFP separation-based method, the same dataset shown in Table 1.1 was analyzed with this method and showed a reduction of directed motion events upon benomyl treatment in wildtype cells (Table 1.6).

Dicentric and monocentric mini-chromosome analysis

Images of unreplicated dicentric and monocentric mini-chromosomes were deconvolved using Huygens Essential compute engine 4.3.1p3 64b (Scientific Volume Imaging B.V., Laapersveld, The Netherlands). Spindle lengths were measured using MetaMorph 7.7 software by measuring the distance between brightest pixels of the two spindle pole body foci. Dicentric and monocentric chromosome lengths were measured parallel and perpendicular to the spindle axis by generating a linescans using MetaMorph 7.7 software, and calculating the full-width-half-max of the linescan as previously described (Stephens et al., 2011). The angle of TetR/TetO-GFP array was determined by taking the angle between a line along the longest axis of the TetR/TetO-GFP array and a line connecting the two brightest pixels of the spindle pole body foci. The kinetochore microtubule length was measured as the distance between the end of the TetR-GFP signal, as determined by full-width-half-max analysis, to the brightest pixel of the proximal spindle pole body signal on compiled image stacks that were not deconvolved. Replicated monocentric extension length was measured using the full-width-half-max analysis on compiled image stacks that were not deconvolved. Heatmaps of the TetR-GFP arrays of dicentric plasmids were constructed using a custom MATLAB program as described in Stephens et al. (2011).

Fluorescence recovery after photobleaching

Cell strain T3000 was prepared as described above and imaged on the same microscope system as above. GFP signal from a dicentric chromosome were photobleached with a Sapphire 488-50 CDRH laser (Coherent, Santa Clara, CA, USA). In order to compensate for photobleaching during acquisition, 3 Z-series were taken to estimate the bleaching rate during Z-series acquisition. A Z-series was obtained immediately before, immediately after, and then at 1-minute intervals after photobleaching. Integrated intensity values were measured using MetaMorph 7.7 imaging software (Molecular Devices, Sunnyvale, CA, USA) for a 5 x 5 region over the photobleached spot for the in-focus plan of each Z-series at each timepoint. The half-life of photobleaching was calculated as $\frac{\ln(2)}{k}$, where k is the rate constant, calculated

as: $\frac{F_{\infty}-F_t}{F_{\infty}-F_0} = e^{-kt}$, where F_{∞} is the average fluorescence intensity after maximum recovery, F_t is the fluorescence intensity at each time point, F_0 is the fluorescence intensity immediately after photobleaching, and t is time.

Cells containing labeled condensin (Smc4-GFP) were photobleached and analyzed as described above except images were taken on an inverted, widefield microscope (Eclipse TE2000-U; Nikon) with a 100x Plan Apo 1.4 NA digital interference contrast oil emersion lens with a camera (Orca ER; Hamamatsu Photonics, Bridgewater, NJ) with MetaMorph 6.1 software. After photobleaching images were taken every 5 minutes for a 10-minute duration.

REFERENCES

- Araki, H., N. Nakanishi, B.R. Evans, H. Matsuzaki, M. Jayaram, and Y. Oshima. 1992. Site-specific recombinase, R, encoded by yeast plasmid pSR1. *J Mol Biol.* 225:25-37.
- Bloom, K.S. 2014. Centromeric Heterochromatin: The Primordial Segregation Machine. *Annu Rev Genet.*
- Blumberg, S., A.V. Tkachenko, and J.C. Meiners. 2005. Disruption of protein-mediated DNA looping by tension in the substrate DNA. *Biophys J.* 88:1692-1701.
- Bouzigues, C., and M. Dahan. 2007. Transient directed motions of GABA(A) receptors in growth cones detected by a speed correlation index. *Biophys J.* 92:654-660.
- Brower-Toland, B.D., C.L. Smith, R.C. Yeh, J.T. Lis, C.L. Peterson, and M.D. Wang. 2002. Mechanical disruption of individual nucleosomes reveals a reversible multistage release of DNA. *Proc Natl Acad Sci U S A.* 99:1960-1965.
- de Gennes, P.G. 1979. Scaling Concepts in Polymer Physics. Cornell Univ. Press, Ithaca, New York.
- Dewar, H., K. Tanaka, K. Nasmyth, and T.U. Tanaka. 2004. Tension between two kinetochores suffices for their bi-orientation on the mitotic spindle. *Nature.* 428:93-97.
- Gardner, M.K., C.G. Pearson, B.L. Sprague, T.R. Zarzar, K. Bloom, E.D. Salmon, and D.J. Odde. 2005. Tension-dependent regulation of microtubule dynamics at kinetochores can explain metaphase congression in yeast. *Mol Biol Cell.* 16:3764-3775.
- Goshima, G., and M. Yanagida. 2000. Establishing biorientation occurs with precocious separation of the sister kinetochores, but not the arms, in the early spindle of budding yeast. *Cell.* 100:619-633.
- Haase, J., A. Stephens, J. Verdaasdonk, E. Yeh, and K. Bloom. 2012. Bub1 kinase and Sgo1 modulate pericentric chromatin in response to altered microtubule dynamics. *Curr Biol.* 22:471-481.
- He, X., S. Asthana, and P.K. Sorger. 2000. Transient sister chromatid separation and elastic deformation of chromosomes during mitosis in budding yeast. *Cell.* 101:763-775.
- Hertwig, O. 1906. Lehrbuch der Entwicklungsgeschichte des Menschen und der Wirbeltiere (Textbook of developmental history of humans and vertebrates).
- Hsu, J.M., J. Huang, P.B. Meluh, and B.C. Laurent. 2003. The yeast RSC chromatin-remodeling complex is required for kinetochore function in chromosome segregation. *Mol Cell Biol.* 23:3202-3215.
- Kawashima, S.A., Y. Yamagishi, T. Honda, K. Ishiguro, and Y. Watanabe. 2010. Phosphorylation of H2A by Bub1 prevents chromosomal instability through localizing shugoshin. *Science.* 327:172-177.
- Kendall, A., M.W. Hull, E. Bertrand, P.D. Good, R.H. Singer, and D.R. Engelke. 2000. A CBF5 mutation that disrupts nucleolar localization of early tRNA biosynthesis in yeast also suppresses tRNA gene-mediated transcriptional silencing. *Proc Natl Acad Sci U S A.* 97:13108-13113.
- Kleckner, N. 2006. Chiasma formation: chromatin/axis interplay and the role(s) of the synaptonemal complex. *Chromosoma.* 115:175-194.
- Kleckner, N., D. Zickler, and G. Witz. 2013. Molecular biology. Chromosome capture brings it all together. *Science.* 342:940-941.
- Kopski, K.M., and T.C. Huffaker. 1997. Suppressors of the ndc10-2 mutation: a role for the ubiquitin system in *Saccharomyces cerevisiae* kinetochore function. *Genetics.* 147:409-420.

- Kosco, K.A., C.G. Pearson, P.S. Maddox, P.J. Wang, I.R. Adams, E.D. Salmon, K. Bloom, and T.C. Huffaker. 2001. Control of microtubule dynamics by Stu2p is essential for spindle orientation and metaphase chromosome alignment in yeast. *Mol Biol Cell*. 12:2870-2880.
- Lebedeva, N.V., A. Nese, F.C. Sun, K. Matyjaszewski, and S.S. Sheiko. 2012. Anti-Arrhenius cleavage of covalent bonds in bottlebrush macromolecules on substrate. *Proc Natl Acad Sci U S A*. 109:9276-9280.
- Lobachev, K., E. Vitriol, J. Stemple, M.A. Resnick, and K. Bloom. 2004. Chromosome fragmentation after induction of a double-strand break is an active process prevented by the RMX repair complex. *Curr Biol*. 14:2107-2112.
- Lowary, P.T., and J. Widom. 1998. New DNA sequence rules for high affinity binding to histone octamer and sequence-directed nucleosome positioning. *J Mol Biol*. 276:19-42.
- Maeshima, K., and U.K. Laemmli. 2003. A Two-Step Scaffolding Model for Mitotic Chromosome Assembly. *Dev Cell*. 4:467-480.
- Michaelis, C., R. Ciosk, and K. Nasmyth. 1997. Cohesins: chromosomal proteins that prevent premature separation of sister chromatids. *Cell*. 91:35-45.
- Naumova, N., M. Imakaev, G. Fudenberg, Y. Zhan, B.R. Lajoie, L.A. Mirny, and J. Dekker. 2013. Organization of the mitotic chromosome. *Science*. 342:948-953.
- Panyukov, S., E.B. Zhulina, S.S. Sheiko, G.C. Randall, J. Brock, and M. Rubinstein. 2009a. Tension Amplification in Molecular Brushes in Solutions and on Substrates (dagger). *J Phys Chem B*.
- Panyukov, S.V., S.S. Sheiko, and M. Rubinstein. 2009b. Amplification of tension in branched macromolecules. *Phys Rev Lett*. 102:148301.
- Paulson, J.R., and U.K. Laemmli. 1977. The structure of histone-depleted metaphase chromosomes. *Cell*. 12:817-828.
- Pearson, C.G., P.S. Maddox, E.D. Salmon, and K. Bloom. 2001. Budding yeast chromosome structure and dynamics during mitosis. *J Cell Biol*. 152:1255-1266.
- Pearson, C.G., P.S. Maddox, T.R. Zarzar, E.D. Salmon, and K. Bloom. 2003. Yeast kinetochores do not stabilize Stu2p-dependent spindle microtubule dynamics. *Mol Biol Cell*. 14:4181-4195.
- Rao, S.S., M.H. Huntley, N.C. Durand, E.K. Stamenova, I.D. Bochkov, J.T. Robinson, A.L. Sanborn, I. Machol, A.D. Omer, E.S. Lander, and E.L. Aiden. 2014. A 3D Map of the Human Genome at Kilobase Resolution Reveals Principles of Chromatin Looping. *Cell*. 159:1665-1680.
- Roberts, B.T., K.A. Farr, and M.A. Hoyt. 1994. The *Saccharomyces cerevisiae* checkpoint gene BUB1 encodes a novel protein kinase. *Mol Cell Biol*. 14:8282-8291.
- Snider, C.E., A.D. Stephens, J.G. Kirkland, O. Hamdani, R.T. Kamakaka, and K. Bloom. 2014. Dyskerin, tRNA genes, and condensin tether pericentric chromatin to the spindle axis in mitosis. *Journal of Cell Biology*. 207.
- Stephens, A.D., J. Haase, L. Vicci, R.M. Taylor, 2nd, and K. Bloom. 2011. Cohesin, condensin, and the intramolecular centromere loop together generate the mitotic chromatin spring. *J Cell Biol*. 193:1167-1180.

- Stephens, A.D., R.A. Haggerty, P.A. Vasquez, L. Vicci, C.E. Snider, F. Shi, C. Quammen, C. Mullins, J. Haase, R.M. Taylor, 2nd, J.S. Verdaasdonk, M.R. Falvo, Y. Jin, M.G. Forest, and K. Bloom. 2013. Pericentric chromatin loops function as a nonlinear spring in mitotic force balance. *J Cell Biol.* 200:757-772.
- Straight, A.F., A.S. Belmont, C.C. Robinett, and A.W. Murray. 1996. GFP tagging of budding yeast chromosomes reveals that protein-protein interactions can mediate sister chromatid cohesion. *Curr Biol.* 6:1599-1608.
- Tanaka, T.U., N. Rachidi, C. Janke, G. Pereira, M. Galova, E. Schiebel, M.J. Stark, and K. Nasmyth. 2002. Evidence that the Ipl1-Sli15 (Aurora kinase-INCENP) complex promotes chromosome bi-orientation by altering kinetochore-spindle pole connections. *Cell.* 108:317-329.
- Thrower, D.A., and K. Bloom. 2001. Dicentric chromosome stretching during anaphase reveals roles of Sir2/Ku in chromatin compaction in budding yeast. *Mol Biol Cell.* 12:2800-2812.
- Vasquez, P.A., and K. Bloom. 2014. Polymer models of interphase chromosomes. *Nucleus.* 5.
- Verdaasdonk, J.S., P.A. Vasquez, R.M. Barry, T. Barry, S. Goodwin, M.G. Forest, and K. Bloom. 2013. Centromere tethering confines chromosome domains. *Mol Cell.* 52:819-831.
- Wach, A., A. Brachat, C. Alberti-Segui, C. Rebischung, and P. Philippsen. 1997. Heterologous HIS3 marker and GFP reporter modules for PCR-targeting in *Saccharomyces cerevisiae*. *Yeast.* 13:1065-1075.
- Wan, X., D. Cimini, L.A. Cameron, and E.D. Salmon. 2012. The coupling between sister kinetochore directional instability and oscillations in centromere stretch in metaphase PtK1 cells. *Mol Biol Cell.* 23:1035-1046.
- Wan, X., R.P. O'Quinn, H.L. Pierce, A.P. Joglekar, W.E. Gall, J.G. DeLuca, C.W. Carroll, S.T. Liu, T.J. Yen, B.F. McEwen, P.T. Stukenberg, A. Desai, and E.D. Salmon. 2009. Protein architecture of the human kinetochore microtubule attachment site. *Cell.* 137:672-684.
- Weber, S.C., A.J. Spakowitz, and J.A. Theriot. 2012. Nonthermal ATP-dependent fluctuations contribute to the in vivo motion of chromosomal loci. *Proc Natl Acad Sci U S A.* 109:7338-7343.
- Xue, Y., J.C. Canman, C.S. Lee, Z. Nie, D. Yang, G.T. Moreno, M.K. Young, E.D. Salmon, and W. Wang. 2000. The human SWI/SNF-B chromatin-remodeling complex is related to yeast rsc and localizes at kinetochores of mitotic chromosomes. *Proc Natl Acad Sci U S A.* 97:13015-13020.
- Yan, J., T.J. Maresca, D. Skoko, C.D. Adams, B. Xiao, M.O. Christensen, R. Heald, and J.F. Marko. 2007. Micromanipulation studies of chromatin fibers in *Xenopus* egg extracts reveal ATP-dependent chromatin assembly dynamics. *Mol Biol Cell.* 18:464-474.
- Yeh, E., J. Haase, L.V. Paliulis, A. Joglekar, L. Bond, D. Bouck, E.D. Salmon, and K.S. Bloom. 2008. Pericentric chromatin is organized into an intramolecular loop in mitosis. *Curr Biol.* 18:81-90.
- Zickler, D., and N. Kleckner. 1999. Meiotic chromosomes: integrating structure and function. *Annu Rev Genet.* 33:603-754.

CHAPTER 2: CHROMOSHAKE – A CHROMOSOME DYNAMICS SIMULATOR REVEALS CHROMATIN LOOPS STIFFEN CENTROMERIC CHROMATIN¹

Summary

ChromoShake is a three-dimensional simulator designed to find the thermodynamically favored states for given chromosome geometries. The simulator has been applied to a geometric model based on experimentally determined positions and fluctuations of DNA, and the distribution of cohesin and condensin in the budding yeast centromere. Simulations of chromatin in differing initial configurations reveal novel principles for understanding the structure and function of a eukaryotic centromere. The entropic position of DNA loops mirrors their experimental position, consistent with their radial displacement from the spindle axis. The barrel-like distribution of cohesin complexes surrounding the central spindle in metaphase is a consequence of the size of the DNA loops within the pericentromere to which cohesin is bound. Linkage between DNA loops of different centromeres is requisite to recapitulate experimentally determined correlations in DNA motion. The consequences of radial loops and cohesin and condensin binding are to stiffen the DNA along the spindle axis, imparting an active function to the centromere in mitosis.

Introduction

We have developed a computational polymer dynamics simulator named ChromoShake, to understand the physical and behavioral properties of chromatin in the presence of thermal motion. Unlike molecular-scale simulators, ChromoShake can simulate the dynamics of megabases of chromatin on a time scale sufficient to reach an equilibrium state in a matter of days. Chromatin dynamics can be directly compared to time-lapse microscopy in which chromatin is visualized through DNA-binding-GFP fusion

¹ This chapter previously appeared as an article in *Molecular Biology of the Cell*. The original citation is as follows: Lawrimore, J., Aicher, J.K., Hahn, P., Fulp, A., Kompa, B., Vicci, L., Falvo, M., Taylor, R.M., 2nd, and Bloom, K. (2016). ChromoShake: a chromosome dynamics simulator reveals that chromatin loops stiffen centromeric chromatin. *Mol Biol Cell* 27, 153-166.

proteins and their target DNA sequences. Moreover, ChromoShake was designed to study the thermodynamics of the class of proteins known as structural maintenance of chromosomes (SMC). These are ring-complexes that are involved in chromosome condensation (condensin) and sister chromatid cohesion (cohesin). Using ChromoShake, the three dimensional distribution of these proteins can be quantitatively compared to their in vivo distribution (Yeh et al., 2008; Stephens et al., 2011).

ChromoShake is designed a) to increase our intuition on how thermal motion affects the dynamics and overall organization of chromatin of a given geometry and b) to serve as a physically accurate model for testing chromatin structure. Although ChromoShake can be used to generate a variety of three dimensional chromatin structures (See Methods), we limit our use of ChromoShake in this study to the budding yeast pericentromere.

We constructed a three-dimensional model of the budding yeast centromere using experimentally determined geometric distributions of fluorescently labeled cohesin (SMC3-GFP), condensin (SMC4-GFP), and lacO/tetO arrays within the pericentric region. Cohesin loading is regulated and largely coupled to replication, thus ensuring that cohesion is established between sister chromatids. Cohesin and condensin are 3X enriched in a 30- to 50 kb of DNA around each centromere, (Megee et al., 1999; Tanaka et al., 1999; Glynn et al., 2004; Weber et al., 2004; D'Ambrosio et al., 2008; Hu et al., 2011). Cohesin function in the pericentromere remains enigmatic. Since sister centromeres are separated by 800 nm, cohesin does not tether sister centromere DNAs to one another in mitosis (Pearson et al., 2001). It has been proposed that individual cohesin complexes link different chromatin strands and different loops of the same strand (Stephens et al., 2013). Condensin is found along the spindle axis and appears variously as spots or linear arrays between the spindle poles in mitosis (Stephens et al., 2011). The position of condensin is dependent upon tRNA binding factors that function to cross-link pericentromeres from different chromosomes (Snider et al., 2014). Pericentric chromatin labeled with lacO/LacI-GFP at multiple locations has been found to be radially displaced from the spindle axis when GFP signals appear as foci, but fall closer to the spindle axis when signals appear stretched (Stephens et al., 2011; Haase et al., 2012).

There are several models for the chromatin organization within the centromere. A model where radial loops emanate from a primary axis between the spindle poles of the mitotic apparatus is most

consistent with experimental findings (Yeh et al., 2008; Stephens et al., 2011). Recent work has suggested that crowded radial loops stemming from a primary axis build tension along the axis (Lawrimore et al., 2015). This is a severe departure from the established view that centromere acts as a passive spring, simply stretched and compressed by microtubule dynamics that it exerts little control over. To explore this hypothesis, we have used molecular dynamics based on in vivo structures to determine the mechanical properties of the centromere. ChromoShake provides the opportunity to quantitatively assess how well a geometrical model that fluctuates to the favored entropic state compares to experimental findings. Moreover, this approach provides the opportunity to differentiate active, directed events in the pericentromere vs. passive, entropic mechanisms that together contribute to the function and morphology of the centromere in live cells.

Results

Thermodynamics collapses radial sub-loops

The pericentromere is the region of DNA surrounding the centromere on each of 16 chromosomes. The 16 centromeres are replicated prior to mitosis, become clustered, and bi-oriented relative to the spindle poles (red disks, Figure 2.1 A) of the mitotic spindle apparatus. In our model, the centromere DNA lies at the apex of the primary loop, where the kinetochore is built and promotes microtubule attachment (Figure 2.1 A, kinetochores are white end beads, green rods are microtubules). The primary centromeric axis is parallel to the microtubule spindle axis. To mimic the radial displacement of lacO/tetO arrays observed in vivo (Stephens et al., 2011; Haase et al., 2012), each chromatid is arranged as a loop with four sub-loops radiating from the primary loop (proximal to the spindle axis) (Figure 2.1 A, colored strands). Chromosome arms (Figure 2.1 A, elongated strands) beyond the pericentromere are not modeled in simulations (Figure 2.1 B-E). Each pericentric chromatid in the model is 50 kb (Figure 2.1 B-E). The 32 chromatid strands represent the replicated 16 chromosomes. The total amount of simulated DNA in the ensemble of 32 chromatids is about 1.6 Mb (Figure 2.1 B-E). The simulated DNA occupies a cylindrical geometry about 778 nm in diameter and 800 nm long (Figure 2. 1B-E).

To understand how thermal motion affects the structure of the centromere, we built a 3D model based on experimental observations of pericentric chromatin and assessed the range of configurations dictated by thermal forces. The computational model is a way to build intuition about a complex structure that would be otherwise be difficult to predict. A robust model of chromatin dynamics can be captured using a simple bead-spring model. In our model, the beads repel each other and are not allowed to pass through one another. This is known as excluded volume and simulates the volume around each chain that is inaccessible to other chains in the system. Hinge-like forces between each bead are parameterized to give the strands the same bending rigidity of DNA, i.e. a persistence length of 50 nm (Bloom, 2008). In the model, cohesin is simulated as a 51-nm diameter ring (white rings, Figure 1) formed by 16 linked beads that encompasses two neighboring chromatid strands. These rings have the same rigidity as the simulated chromatin and can migrate along the chromatin strands. Thermal forces collapse the rings to an average diameter of 44.6, 44.9, and 47.0 nm for cohesin not encompassing chromatin,

cohesin encompassing a single chromatin strand, and cohesin encompassing chromatin four strands in the centromere model respectively (Table 2.1). Condensin is modeled as a spring (not shown in Figure 2.1) that connects two beads on the same chromatin strand to form radial sub-loops. Condensin is localized along the spindle axis in fluorescent images (Stephens et al., 2011); therefore, we confined our condensin springs proximal to the spindle axis at the base of the radial sub-loops. The beads at the ends of the primary loops (Figure 2.1, white beads) are five orders of magnitude more massive than the other beads to “pin” the model in space and mimic attachment of the centromere to microtubules. Microtubule dynamics were not included as their contribution to fluctuations of pericentromeric DNA is nominal (Lawrimore et al., 2015). We loaded our centromere model into ChromoShake to simulate the thermal motion of beads and bead-ring complexes. The model was allowed to run for ~0.05 seconds of simulation time and then rendered (Figure 2.1, D and E). These images show how chromatin loops crumple toward the spindle axis upon perturbation by thermal forces.

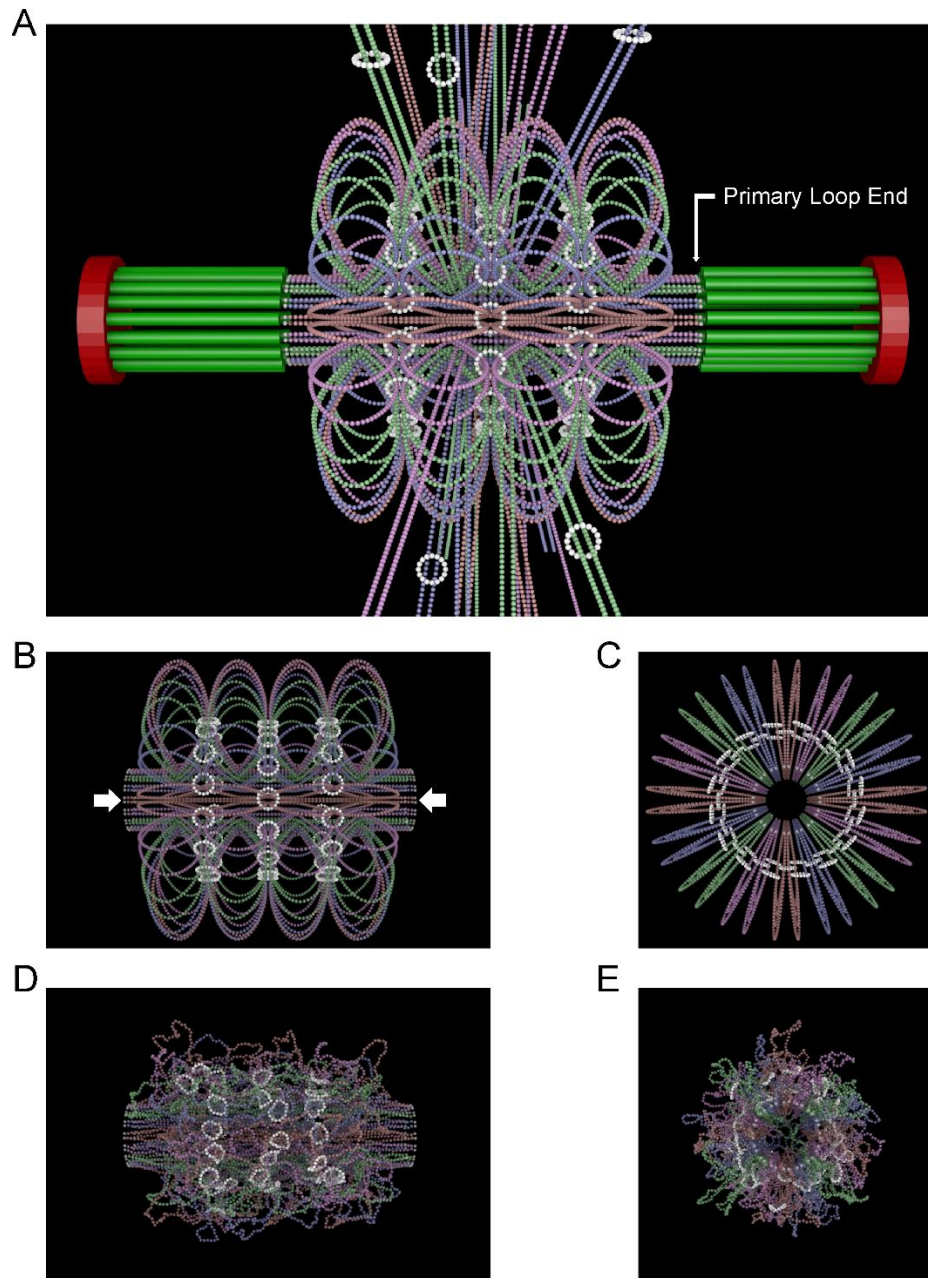


Figure 2.1 – Thermal forces collapse radial chromatin loops

(A) A three-dimensional model of the yeast spindle and the centromere. The red disks are the spindle pole bodies. The green rods are the kinetochore microtubules. The colored strands are chromatin. The primary loop (horizontal portion) is attached to a kinetochore microtubule. Chromosome arms extend perpendicular to the spindle axis. The white rings are cohesin. Condensin is located at the base of each radial sub-loop (not shown). Side (B) and end-on view (C) of the centromere polymer model prior to the introduction of thermal forces. The centromere model only simulates 50 kb of DNA per sister chromatid strand. The arms of each chromosome are not simulated in the model nor are microtubules. Each strand has four sub-loops radially extending from the primary loop. The gray beads indicated by arrows are pinned in space to represent attachment to the spindle. Side (D) and end-on (E) view of centromere polymer model after thermal force has been introduced.

Table 2.1 – Diameter of cohesin rings after perturbation by thermal forces

	Mean Diameter (nm)	Standard Deviation (nm)
Cohesin (n = 3)	44.6	0.1
Cohesin encompassing one strand (n = 10)	44.9	0.7
Cohesin encompassing four strands (n = 48)	47.0	0.2

The ensemble mean diameter was calculated for individual cohesin rings for the final 2000 timepoints (0.02 seconds of simulation time) of each simulation (see Methods).

Radial sub-loops replicate the position and the motion of chromatin observed in experimental samples

Previous studies have measured chromatin position and fluctuations in vivo using tandem-repeat sequences of the lactose operon (lacO) or tetracycline operon (tetO) integrated into chromosomes in cells expressing LacI-GFP or TetR-GFP fusion proteins (Straight et al., 1996; Michaelis et al., 1997). The probability distribution of fluorescently labeled chromatin reveals that the pericentromere DNA is, on average, radially displaced from the spindle axis (Anderson et al., 2009; Stephens et al., 2011). Since ChromoShake only simulates thermal forces, we compared our simulated motion data to experimental data in which ATP was depleted through treatment of cells with sodium azide and deoxy-glucose. We performed timelapse imaging of pericentric chromatin labeled with a 10 kb (256 repeat) lacO/LacI-GFP array centered 6.8 kb from CEN15. We imaged cells for 10 minutes every 30 seconds in media containing sodium azide and deoxy-glucose. To mimic the 6.8 kb lacO array in the centromere model, we tracked the mean position of a 73-bead array (~10 kb) centered 49 beads (~6.8 kb) from each of the centromeres (Figure 2.1, centromeres are white beads). Given the symmetry of our centromere model (Figure 2.1), we individually tracked the mean position of all 64 simulated 6.8 kb arrays. We found the 6.8 kb array has a radial displacement (mean \pm standard deviation) of 134 ± 74 nm in ATP-depleted cell and 140 ± 51 nm in the simulations (Figure 2.2, A and B).

The fluctuations of the tetO/lacO arrays have been measured in live cells using single particle tracking and mean squared displacement (MSD) analysis, allowing us to compare the fluctuations of our model directly to live cell measurements. The motion of tetO/lacO arrays is confined, and the extent of confinement is reflected by the plateau value of the MSD curve (Weber et al., 2012; Verdaasdonk et al., 2013; Chacon et al., 2014). The plateau value of a 6.8 kb array in ATP-depleted cells was published as 5600 ± 3200 nm² (Lawrimore et al., 2015), whereas the mean \pm standard deviation of the MSD plateau value for the simulated 6.8 kb array was 4000 ± 110 nm² (Figure 2.2 C). Thus, our simulation recapitulates the experimental distribution and fluctuations of chromatin in the absence of ATP-dependent processes.

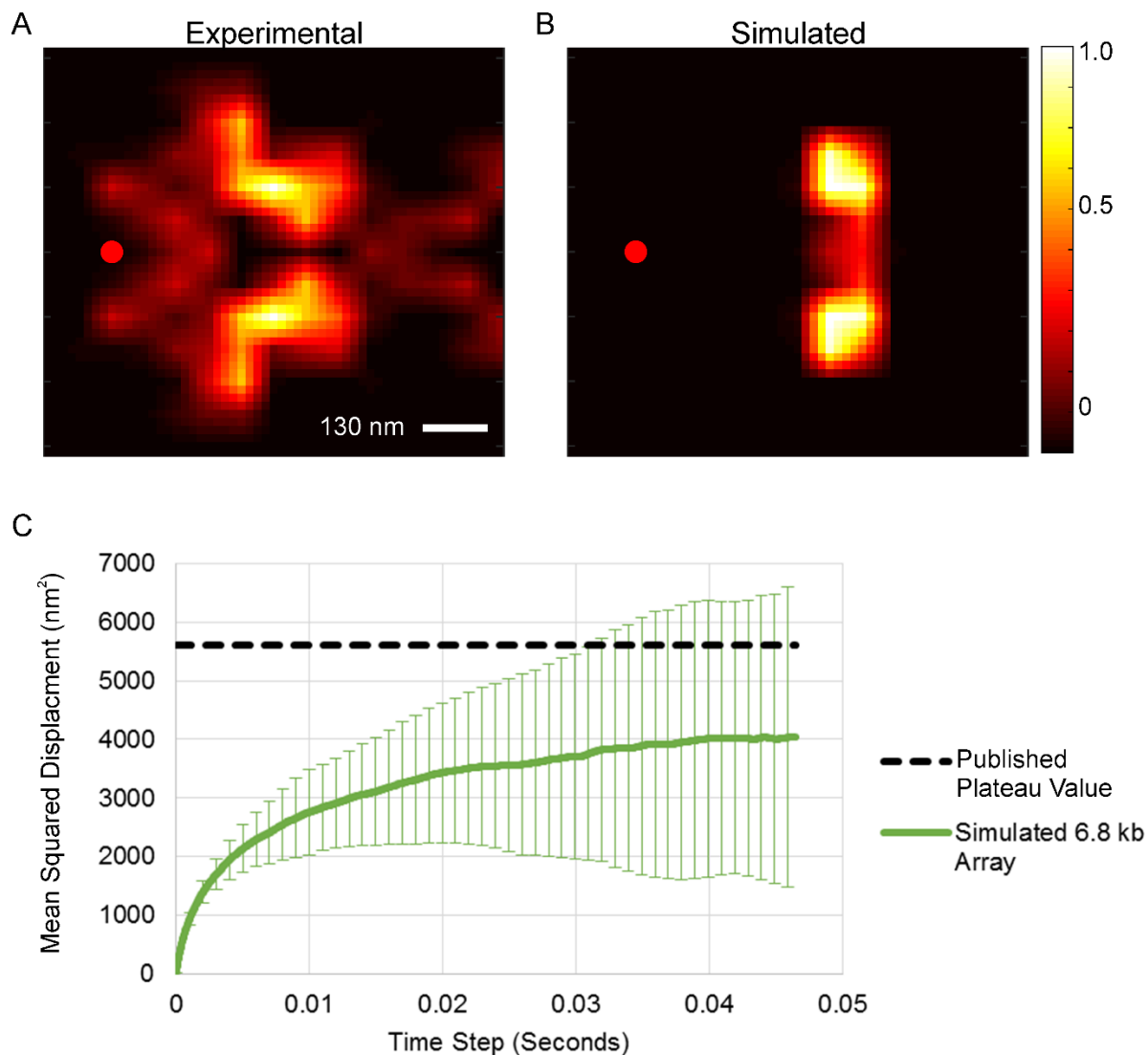


Figure 2.2 – Distribution and Fluctuations of Experimental and Simulated 6.8 kb Array

Probability maps (heatmaps) of the position of a 6.8 kb array (10 kb lacO/LacI-GFP array centered 6.8 kb from CEN15) relative to the proximal spindle pole body (red dot) from cells treated with sodium azide and deoxy-glucose (A) and a simulated 6.8 kb array (73 beads, see Figure 5). (B) For the simulated heatmap the spindle pole body (red dot) was placed 635 nm from the center of the pericentric model to mimic the average experimental spindle length of 1.27 μm . (C) MSD curve of the simulated 6.8 array. The experimental plateau value is 5600 nm² from cells treated with sodium azide and deoxy-glucose (Lawrimore et al., 2015). The initial 0.05 seconds were not analyzed to allow each model to reach equilibrium. Error bars are standard deviation. Experimental n = 37 arrays tracked. Simulated n = 64 arrays tracked.

Cohesin distribution is determined by chromatin sub-loop size

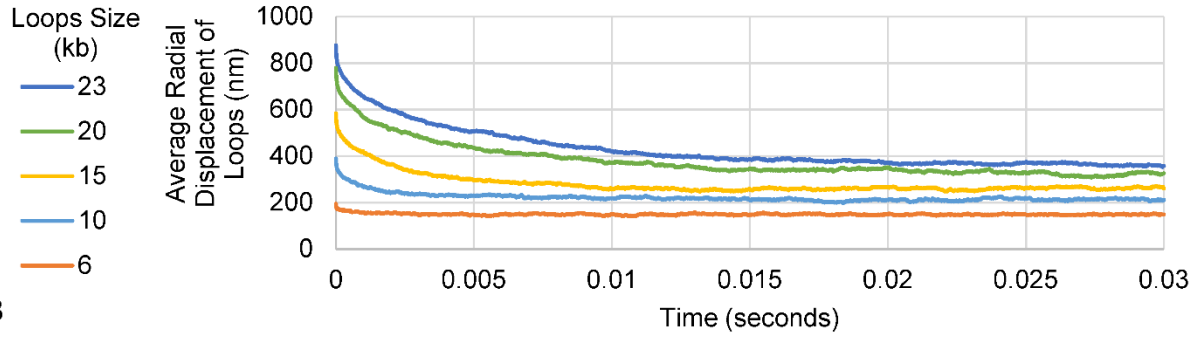
Cohesin is radially displaced from the spindle axis (Yeh et al., 2008; Stephens et al., 2011). There is no molecular mechanism that accounts for the position and homogenous appearance of pericentric cohesin. To explore whether the size and position of the chromatin sub-loops dictate the position of cohesin we measured the mean radial displacement of the tips (most radially displaced beads at initial configuration) of the chromatin sub-loops (Figure 2.3 A) and cohesin (Figure 2.3 B) over the initial 0.03 seconds of simulation time. Mean radial displacement is defined as the mean of all the distances of tips of the sub-loops or cohesin from the center of the cylindrical array of the chromosome (Figure 2.1 C). The mean radial displacement of the chromatin sub-loops (10 kb per sub-loop) collapsed from 389 nm to 210 nm, while cohesin decreased from 223 nm to 170 nm radius (Figure 2.3, Table 2.2). We generated centromere models with varying sub-loop lengths (6 to 23 kb) and found that the size of the sub-loop dictates the size of the cohesin barrel (Figure 2.3, Table 2.2).

To determine the relationship between DNA sub-loop size and position of cohesin, we created centromere models with identical 10 kb DNA sub-loops (initially 389 nm from the spindle axis), but with varying initial cohesin barrel sizes. Despite different initial radial displacements, the mean radial displacement of each cohesin distribution converged to the same mean radial displacement over time (Figure 2.3 C). Cohesin barrels with mean radii less than 240 nm linking 10 kb sub-loops show an initial period of expansion relative to the starting configuration prior to collapse (Figure 2.3 C). Additionally, the cohesin barrel of the centromere model with 6 kb sub-loops had a greater final mean radial displacement than initial (Figure 2.3 C). These data are suggestive of a repulsive force away from the base of sub-loops that is overcome by the collapse of loops greater than 6 kb.

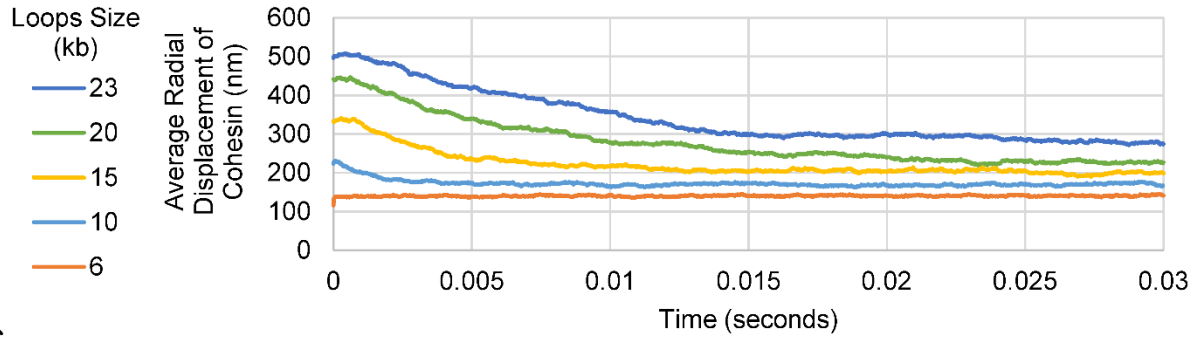
Fluorescently labeled cohesin has a characteristic cylindrical structure around the spindle microtubules during metaphase (Yeh et al., 2008; Stephens et al., 2011). When viewed from the side, fluorescently labeled cohesin has a persistent bi-lobed appearance. To test whether cohesin maintains this bi-lobed distribution in ChromoShake, we convolved our cohesin bead-rings with a point-spread-

function from a fluorescence microscope used to image cohesin (Smc3-GFP) using the program Microscope Simulator 2 (Quammen et al., 2008). Centromere models with loops greater than 15-20 kb maintained a bi-lobed geometry when viewed in sagittal section at thermodynamic equilibrium (Figure 2.4).

A



B



C

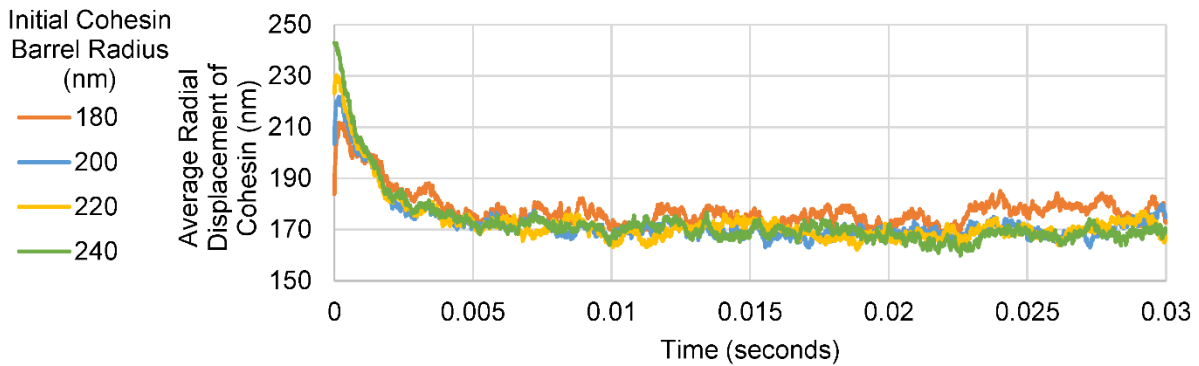


Figure 2.3 – Chromatin loops dictate cohesin distribution

Average radial displacement of the cohesin barrel (A) and the chromatin loops (B) over simulation time for centromere models with varying radial loop sizes. (C) Average radial displacement of cohesin over simulation time for centromere model with 10 kb loops with varying initial cohesin barrel radii. The average radial displacement of the cohesin barrel measured all the positions of the cohesin beads, while the loop measurements are only of the tips of the outermost (closest to the centromere) loops.

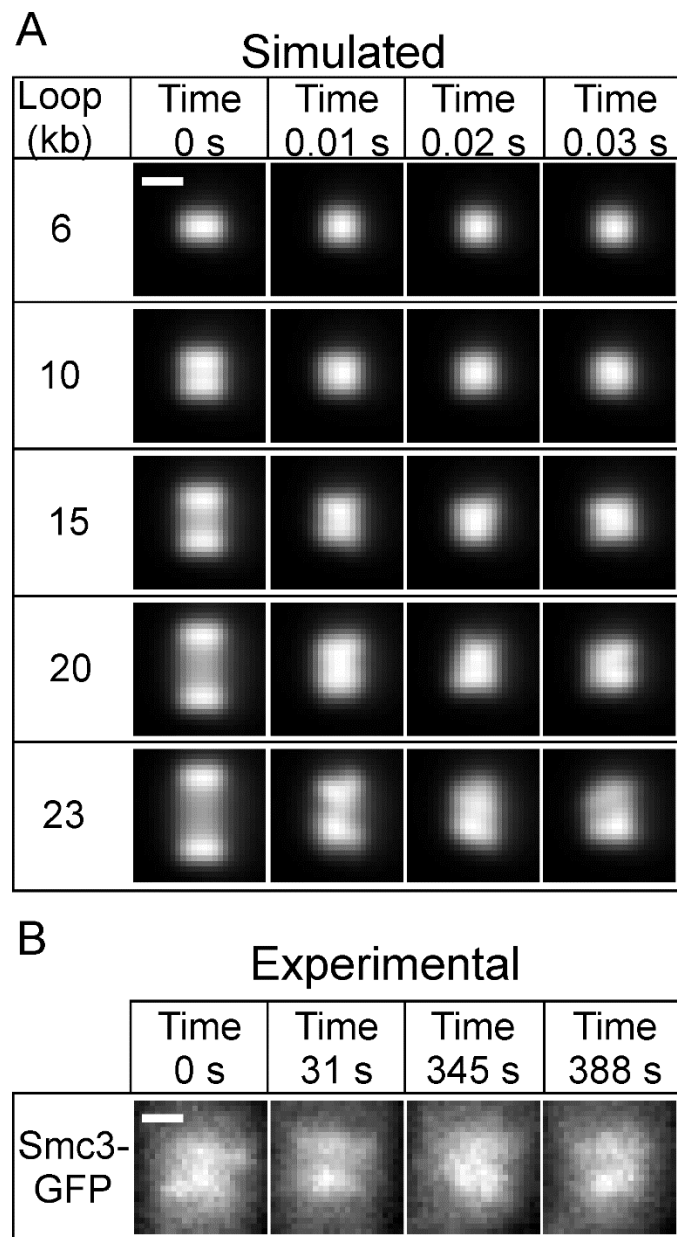


Figure 2.4 – Size of radial loops affects cohesin barrel shape

(A) Simulated fluorescent images of the cohesin barrel over simulation time. (B) Fluorescent time-lapse of cohesin complex subunit Smc3-GFP. Scale bars are 500 nm.

Table 2.2 – Initial and final average radial displacements of chromatin loops and cohesin distribution

Sub-Loop Size (kb)	Initial DNA Displacement (nm)	Final DNA Displacement (nm)	Initial Cohesin Displacement (nm)	Final Cohesin Displacement (nm)
6	195	149	116	141
10	389	210	223	170
15	584	261	332	199
20	779	325	442	227
23	876	356	497	275

Mean squared displacement affected by fluorescent array size and position

A recent study showed that the size of fluorescent particles in bacterial cells is inversely correlated with the MSD of the particle (Parry et al., 2014). This parameter is critical in studies deriving time constants to distinguish diffusional from sub-diffusional motion. We found an inverse correlation between size and MSD by timelapse imaging live yeast cells and comparing the MSD curves of a 1.7 kb lacO/LacI-GFP array placed 1.1 kb from CEN3 and a 10 kb array placed 1.8 kb from CEN15 (Figure 2.5). The size and placement of tet/lac operon arrays relative to chromosome landmarks such as loops, insulators, and centromeres can affect the MSD plateau value. As predicted by Parry et al. and our experimental measurements (Figure 2.5), we found that simulated array size is inversely correlated with MSD plateau value (Figure 2.6 A, Table 2.3). Thus, the motion of lacO/tetO arrays of different sizes are not directly comparable. We compared the MSD of our simulated 6.8 kb array (10 kb long, 256 lacO/LacI-GFP repeat, centered 6.8 kb from CEN15) to a simulated 1.7 kb array (1.7 kb long, 33 repeat lacO/LacI-GFP repeat, centered 1.1 from CEN3) (Pearson et al., 2001; Chacon et al., 2014). The 6.8 kb array is 73 beads which comprises most of the first sub-loop, while the 1.7 kb array is 8 beads and mostly encompasses chromatin proximal to the spindle axis (Figure 2.6). Surprisingly, the mean plateau value \pm standard deviation of the 6.8 kb and 1.7 kb arrays are 4000 ± 110 and 230 ± 5 nm respectively (Figure 2.6 B). Given the smaller array had a smaller MSD plateau value, which was not predicted by our previous results, we queried how the placement of the lacO array within a radial loop affects the MSD plateau value. We found a single bead near the base of a loop has a lower plateau value than a single bead at the tip of a sub-loop, 357 ± 8.7 nm² versus $15,500 \pm 510$ nm² (Figure 2.6 B), but was higher than the simulated 1.7 kb array (8 beads) value of 230 ± 5 nm, again demonstrating that array size is inversely related to MSD plateau value when the labels are in a similar location. Thus, the position of a lacO/tetO array, either within a radial sub-loop or along the spindle axis, as well as the size of the array affect the observed motion of a lacO/tetO fluorescent signal.

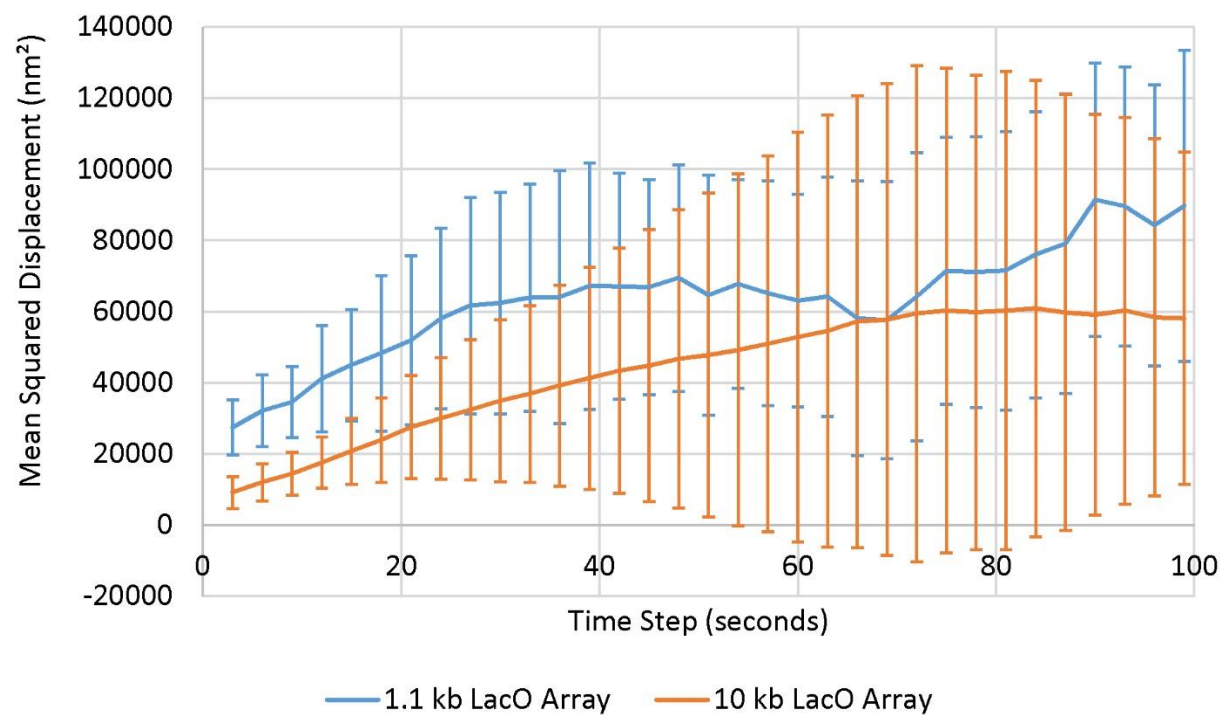


Figure 2.5 – Mean square displacement curves for 1.1 kb and 10 kb LacO arrays

Curves are the average of individual mean displacement curves. 1.7 kb lacO array (n= 12 cells) or a 10 kb array (n = 14 cells). Error bars are standard deviation.

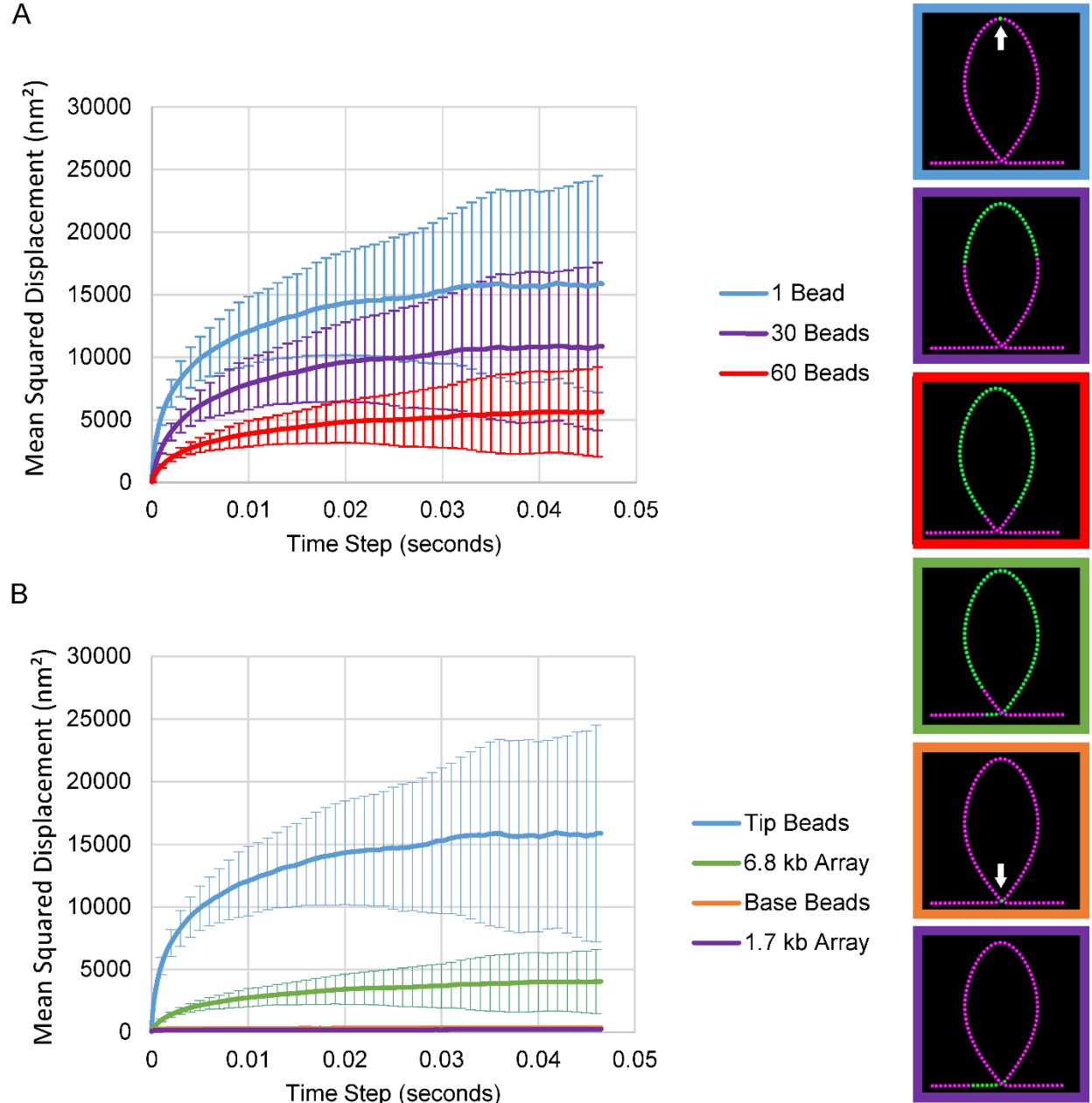


Figure 2.6 – Size and position of fluorescent array affects motion of the array

(A) The ensemble average mean squared displacement of bead arrays of increasing size centered at the tip of a loop. MSD was only measured for the centromere-proximal loops (loops closest to either end of the model) for base and tip beads. (B) The ensemble average MSD of beads located at the tips of a loop, the simulated 6.8 kb array (simulated 10 kb array, 73 beads, centered 6.8 kb from CEN15), beads at the base of a loop, and the simulated 1.7 kb array (simulated 1.7 kb array, 8 beads, centered 1.1 kb from CEN3). Tracked beads are in green. Arrows indicate position of beads that are tracked. The initial 0.05 seconds were not analyzed to allow the model to reach equilibrium (simulation actually ran > 0.1 seconds of simulation time). All MSD values were calculated from the same simulation. Error Bars are standard deviation.

Table 2.3 – Average plateau values of mean squared displacement curves of arrays of different sizes

Number of Beads	% of Loop	Average Plateau value with Standard Deviation (nm ²)
1	1%	15,500 ± 510
10	14%	14,400 ± 490
20	29%	12,600 ± 400
30	43%	10,600 ± 340
40	57%	8,720 ± 280
50	71%	7,010 ± 210
60	86%	5,550 ± 160

Average plateau values were calculated from the MSD values from 0.04 seconds to 0.05651 seconds in Figure 5. The initial 0.05 seconds of the simulation were removed to allow the simulation to reach equilibrium.

Both cohesin linkages and condensin-stabilized sub-loops are needed for experimentally observed correlated motion of different chromosomes

The motion of lacO/tetO arrays within the pericentromere placed on different chromosomes has been shown to be correlated (cross-correlation = 0.33 ± 0.34) (Stephens et al., 2013). Since our centromere model is symmetrical, we can place the simulated 6.8 kb array in any of the outermost (centromere proximal) sub-loops on either end of model. Therefore, a single simulation can contain 64 simulated 6.8 kb arrays, with 32 pairs of cohesin-linked arrays, and 32 pairs of neighboring arrays that are not linked by cohesin, and 32 pairs of “sister” arrays. We performed cross-correlation analysis on our simulated 6.8 kb arrays and found a mean \pm standard deviation cross-correlation value of 0.34 ± 0.21 for cohesin-linked arrays (Figure 2.7 A, Tables 2.4 and 2.5), in quantitative agreement with the experimental value. The motion of neighboring arrays which are not linked by cohesin in our centromere model are not correlated (-0.053 ± 0.25 , Figure 2.7 B, Table 2.4). Unlike Stephens et al. (2013), our centromere model did not show correlated motion in models depleted of cohesin nor between sister arrays with or without cohesin and/or condensin (Figure 2.7 C, Table 2.5), indicative of higher order features in vivo that remain to be incorporated in the model. Models of the centromere lacking cohesin, condensin, or both cohesin and condensin did not exhibit correlated motion (≤ 0.12) between any neighboring arrays or between sister arrays (Figure 2.7, Table 2.4). Thus, in the model, the stabilization of chromatin loops by condensin and the cross-linking of those loops by cohesin are sufficient to account for experimental levels of correlated motion between different chromosomes. This provides a physical basis for the enigma of cohesin function in the pericentromere, namely to coordinate motion between adjacent DNA strands in the ensemble of centromeric chromatin.

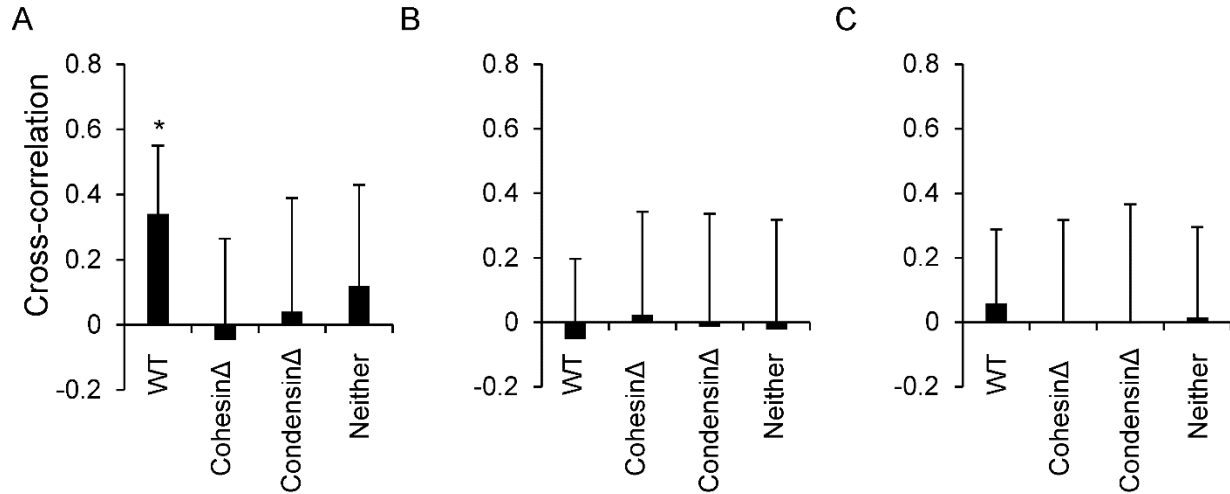


Figure 2.7. – Correlated motion of simulated 6.8 lacO/LacI-GFP array

Cross-correlation analysis of cohesin-linked chromatin strands (A), neighboring, but un-linked chromatin strands (B), and simulated sister-chromatids (C). Each of the four centromere models were run for greater than 0.1 seconds. The initial 0.05 seconds were not analyzed to allow each model to reach equilibrium. Only the motion parallel to the spindle axis was compared to mimic the measurements from Stephens et al. (Stephens et al., 2013b). Asterisk denotes a significant difference from all other data points except cohesin-linked chromatin strands with neither cohesin nor condensin (A, Neither) by Tukey's honest significant difference test ($P < 0.05$).

Table 2.4 – Cross-correlation values of simulated 6.8 lacO/LacI-GFP arrays for motion parallel to the spindle axis

Comparison	With Cohesin, With Condensin	No Cohesin, With Condensin	With Cohesin, No Condensin	No Cohesin, No Condensin
Cohesin-Linked Neighbors	0.34 ± 0.21	-0.045 ± 0.31	0.040 ± 0.35	0.12 ± 0.31
Unlinked Neighbors	-0.053 ± 0.25	0.023 ± 0.32	-0.013 ± 0.35	-0.022 ± 0.34
Sisters	0.058 ± 0.23	-0.0028 ± 0.32	-0.0043 ± 0.37	0.015 ± 0.28

The initial 0.05 seconds were not analyzed to allow each model to reach equilibrium.

Table 2.5 – Comparison of simulated cross-correlation values with published experimental values

Proteins present in simulation	Corresponding genotype	Trans-correlated Movement		Sister-correlated Movement	
		Simulated Values	Published Values	Simulated Values	Published Values
With Cohesin, With Condensin	WT	0.34 ± 0.21	0.33 ± 0.34	0.058 ± 0.23	0.34 ± 0.33
No Cohesin, With Condensin	<i>mcm21Δ</i>	-0.045 ± 0.31	0.36 ± 0.31	-0.0028 ± 0.32	0.35 ± 0.36
With Cohesin, No Condensin	<i>brn1-9</i>	0.040 ± 0.35	$0.21 \pm 0.35^*$	-0.0043 ± 0.37	0.31 ± 0.31

Values are mean cross-correlation values \pm standard deviation. Published values are from (Stephens et al., 2013b). Simulated values are of cohesin-linked neighbors from Table 3.

Cohesin and condensin confine centromeric chromatin

Probability distribution of population images of the 6.8 kb lacO/LacI-GFP array revealed that depletion of pericentric cohesin (*mcm21Δ*) or condensin (*brn1-9^{ts}*), increases the radial displacement of the array and increased the variance of the positions in the population, i.e. expands the area over which the 6.8 kb array can occupy (Stephens et al., 2011). To test if depletion of cohesin and/or condensin would have a similar effect on simulated lacO arrays in the pericentromere, we created centromere models without cohesin, condensin, and without both. We constructed probability distributions from positions of the simulated 6.8 kb arrays on each outer chromatin sub-loop (Figure 2.8). In the absence of cohesin, the radial displacement decreased slightly, 140 to 134 nm, while the distance from the proximal spindle pole body (SPB) decreased from 419 nm to 336 nm. In the absence of condensin, radial displacement increased from 140 nm to 163 nm, while the distance from the proximal SPB decreased from 419 nm to 395 nm. In the absence of both cohesin and condensin, the radial displacement increased from 140 to 186 nm, while the distance from the proximal SPB decreased from 419 to 345. In all deletions, variance (i.e., area-of-exploration) increased (Table 2.6), as found in experimental (Stephens et al. (2011)). The increased radial displacement and variance was also seen in the tips of the loops and the bases of the loops (Tables 2.7 and 2.8). Although, loss of cohesin had little effect on the base beads (Table 2.8). Thus, both cohesin and condensin function to confine DNA loops around the spindle in an area more compact than is thermodynamically favorable.

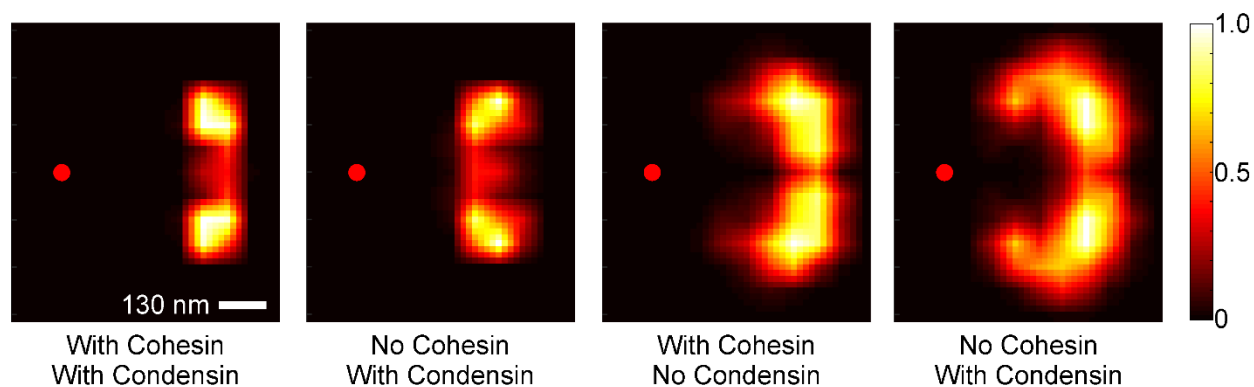


Figure 2.8 – Cohesin and Condensin confine radial loop fluctuations

Probability maps (heatmaps) of a simulated 6.8 kb array (10 kb lacO/LacI-GFP array centered 6.8 kb from CEN15) with both cohesin and condensin, lacking cohesin, lacking condensin, and lacking both cohesin and condensin. The initial 0.05 seconds were not analyzed to allow each model to reach equilibrium. For each simulated heatmap the spindle pole body (red dot) was placed 635 nm from the center of the pericentric model to mimic the average experimental spindle length of 1.27 μm .

Table 2.6 – The average and standard deviation of the axial and radial displacement of the simulated 6.8 kb array

	Radial Displacement		Distance from SPB	
	Average (nm)	Std. (nm)	Average (nm)	Std. (nm)
ATP-depleted cells, 6.8 kb array	134	74	331	178
With Cohesin and Condensin	140	51	419	29
With Condensin, No Cohesin	134	60	336	45
With Cohesin, No Condensin	163	71	395	76
No Cohesin, No Condensin	186	78	345	94

The first 0.05 seconds of each simulation was discarded to allow time for each centromere model to reach equilibrium. Each simulation was run for at least 0.1 seconds of simulation time.

Table 2.7 – The average and standard deviation of the axial and radial displacement of the tips of the radial sub-loops

	Radial Displacement		Distance from Proximal SPB	
	Average (nm)	Std (nm)	Average (nm)	Std (nm)
Tips WT	167	81	193	61
Tips No Cohesin	158	84	287	81
Tips No Condensin	166	82	227	91
Tips No Cohesin No Condensin	196	89	288	112

The first 0.05 seconds of each simulation was discarded to allow time for each centromere model to reach steady state. Each simulation was run for at least 0.1 seconds. Only the tips (most radial bead) of the outermost loops (loops closest to either end) were measured so results could be compared to the simulated 6.8 kb array. SPB = spindle pole body.

Table 2.8 – The average and standard deviation of the axial and radial displacement of the bases of the radial sub-loops

	Radial Displacement		Distance from Proximal SPB	
	Average (nm)	Std (nm)	Average (nm)	Std (nm)
Base WT	98.4	15	395	3.2
Base No Cohesin	99.5	14	395	3.3
Base No Condensin	198	88	763	88
Base No Cohesin No Condensin	246	117	833	116

The first 0.05 seconds of each simulation was discarded to allow time for each centromere model to reach steady state. Each simulation was run for at least 0.1 seconds. Only the bases (least radially displaced bead) of the outermost loops (loops closest to either end) were measured so results could be compared to the simulated 6.8 kb array. SPB = spindle pole body.

Radial side chains and cohesin can extend chromatin

The structure of the centromere model, radially displaced sub-loops relative to a central primary loop resembles a bottle-brush polymer, in which multiple side chains emanating from a single primary chain repel each other resulting in extension of the primary axis. This is contrary to the behavior of a linear polymer chain (Figure 2.9) that collapses into a random coil. In the bottle brush polymer, all chains are trying to collapse to a random coil. However, the radial chains are crowded such that the primary chain is extended, and tension is generated along the primary chain (Figure 2.10 A). Bottle-brush polymers with side chains of long lengths and high density (number of side chains divided by length of the primary chain) can generate tension along the primary chain in the nanoNewton range, which are sufficient to sever covalent bonds within the primary chain (Lebedeva et al., 2012; Panyukov et al., 2009a; Panyukov et al., 2009b). To determine the density and length of side chains required for extensional effects, we measured the average radius of gyration (R_g) of a 1 μm (101 bead) primary chain (Figure 2.10 B) of bottle brush polymers with increasing densities of 200 nm (20 bead) side chains. R_g essentially measures the volume a polymer occupies and is defined as, $R_g^2 \stackrel{\text{def}}{=} \frac{1}{N} \sum_{k=1}^N (r_k - r_{\text{mean}})^2$ where N is the number of spherical masses, r_k is the position of an individual mass, and r_{mean} is the mean position of all the spherical masses. The polymers were allowed 0.04 seconds to collapse into a random coil before calculating the R_g . The R_g increased when more than 10 side chains were added. Beyond 40 side chains the primary axis begins to approach an apparent maximal R_g (190 nm or 76% of the initial R_g of 250 nm, Figure 2.10 C). Thus, the density of side chains, within the range and density predicted for loops in vivo (4 loops x 32 chromatids = 128 over ~ 1 micron) is sufficient to extend and stiffen chromatin along the primary axis. To explore the effects of side chain length, we started with a density of 100 side chains on a 1 μm chain and increased the side chain lengths in 10 nm increments (Figure 2.10 D). The R_g gradually increased until ~180 nm or 72% of the initial R_g (Figure 2.10 D). The length of loops is within the radial distance of experimental loops (~100 nm from the central axis).

In addition to the radial sub-loops that function as side chains in the model, bead-rings, e.g. cohesin, may function to extend chromatin along the primary axis. To test this hypothesis, we constructed a chromatin ring 1 μm in diameter (314 beads, equivalent to ~43 kb) with increasing numbers of cohesin rings (~51 nm diameter). We found that increasing the number of cohesin molecules also resulted in an

increase in the R_g (Figure 2.10, E and F). The R_g was doubled with 70 cohesin rings, corresponding to one cohesin ring every 620 bp. In vivo in budding yeast, cohesin rings are spaced every 9-15 kb, and shows 3X further enrichment in the pericentric region (Blat and Kleckner, 1999; Glynn et al., 2004; Laloraya et al., 2000; Weber et al., 2004). Thus ring-like proteins at sufficient density can stiffen chromatin, providing a mechanism for shaping chromatin structure *in vivo*. This points to a novel function for ring-like protein complexes that may have significant biological implications.

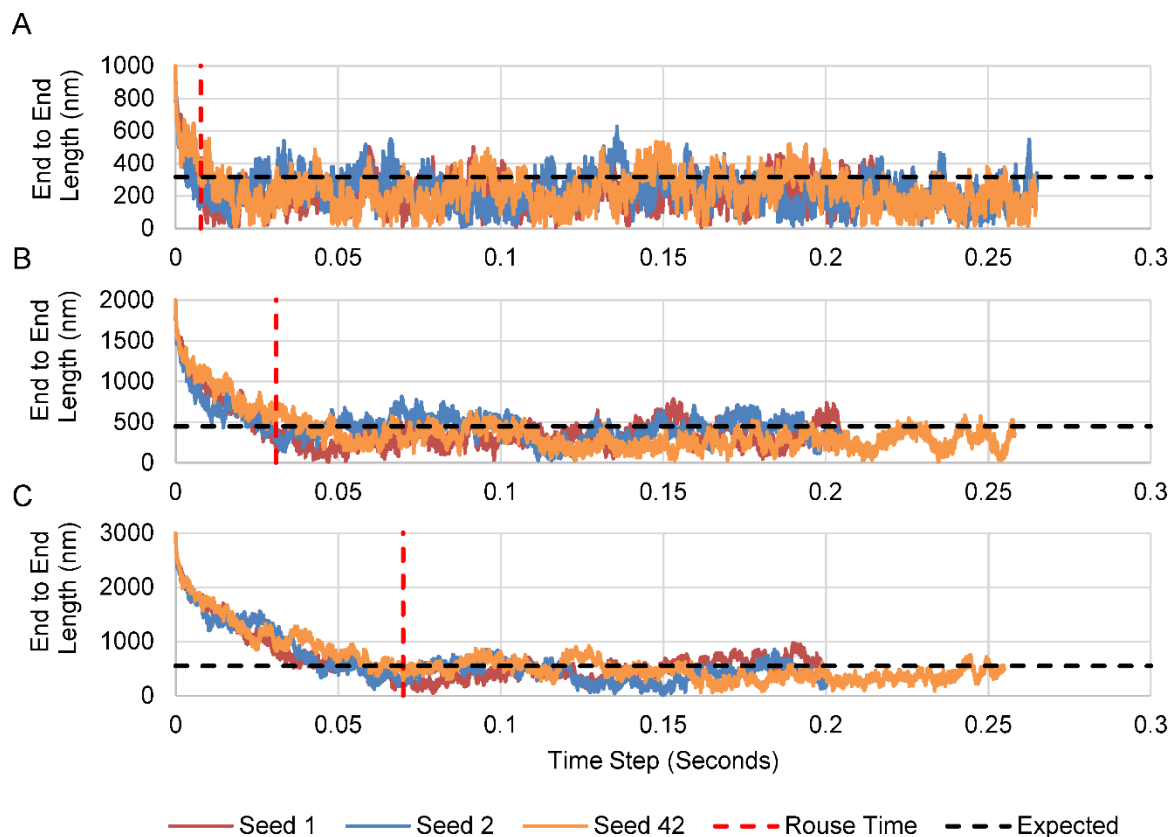


Figure 2.9 – End to end length of simulated chains

End to end lengths of a 1 μm chain (A), 2 μm chain (B), and 3 μm chain (C). Dotted black line is the expected end to end length from the equation $\langle R \rangle = \sqrt{Nb^2}$, where b is Kuhn length and N is the number of segments (Rubinstein and Colby, 2003). Rouse time is the time for a linear polymer to collapse into a random coil calculated by, $\tau_R = \frac{\eta b^3}{\pi k_b T} N^2$ where η is viscosity, b is Kuhn length, k_b the Boltzmann constant, T temperature, and N the number of Kuhn length segments in the chain (Rouse, 1953; Rubinstein and Colby, 2003).

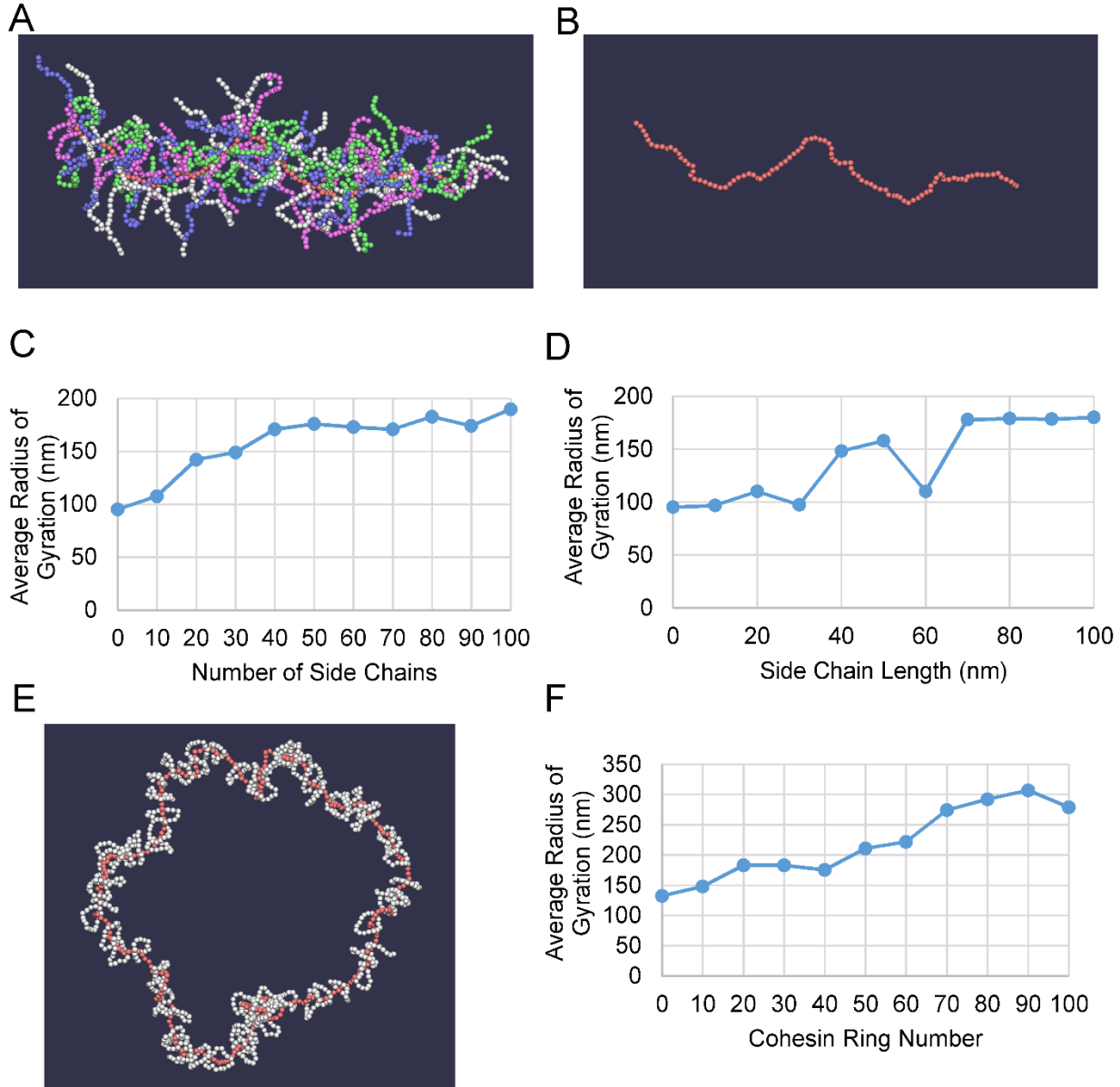


Figure 2.10 – Side chains and cohesin rings can extend chromatin

(A) Bottle-brush polymer model of chromatin with side-chains. The primary axis (B) is in red. The average radius of gyration of the primary axis for bottle-brush polymers with a different number of 200 nm side chains (C) and different side chain length with a density of 100 side chains (D). (E) Ring polymer model of chromatin (1 μm in diameter, ~43 kb). The chromatin is in red. Cohesin rings are in white. (F) The average radius of gyration of the chromatin ring alone with increasing numbers of cohesin molecules. All simulations were run for 0.08 seconds. Only the radii of gyration were from 0.04 seconds to 0.08 seconds were averaged, to allow time for the polymer to reach a steady state. Error bars are standard deviation.

Discussion

A new model for higher-order chromatin structure and dynamics

Thermal forces are ubiquitous and have a dominant influence on molecular dynamics. Chromatin is a dynamic structure, and the particular geometries (loops, crumples, bodies, etc.) will adopt unique configurations not necessarily intuitive in the absence of molecular modeling. Here we describe a computational tool for exploring how specific chromatin geometries are altered in the presence of thermal motion. Using ChromoShake researchers can generate models of chromatin and explore the consequences of thermal force on predicted structure. ChromoShake data can be compared with experimental data to determine the structure and forces affecting chromatin in living cells. Our model of the yeast centromere illustrates how chromatin structure can affect protein and DNA distribution, and reveals functional attributes not previously reported.

Size and position of tetO/lacO arrays affect their observed motion

Tandem repeat arrays of lac/tet operons have been used to label chromatin for decades (Michaelis et al., 1997; Robinett et al., 1996; Straight et al., 1996). In the pericentromere we have used these arrays to demonstrate that on average, the DNA, like cohesin, is radially displaced from the spindle axis (Anderson et al., 2009; Stephens et al., 2011). A major difference in the motion of DNA arrays *in vivo* vs. *in silico* is that the *in vivo* motion is greater than that found *in silico* (Figure 2.5 vs Figure 2.2). While depletion of ATP *in vivo* largely recapitulates the *in silico* motion (Figure 2.2 B), the biological condition is much more violent than in simulation. Factors such as remodeling complexes, chaperones, crowding, etc. are constantly bombarding the chromatin. The net effect is increased motion with a random signature, due to the random trajectory of the sum of a number of different inputs. This can be simulated by increasing temperature *in silico*. One of the outstanding questions is whether there is information in the *in vivo* trajectories that might reveal hierarchies in the source of this noise.

A second insight from ChromoShake is that size of the tracer (lacO) influences the slope and magnitude of the MSD curve (Figure 2.6). MSD is a widely used metric for deducing the form of motion (sub-diffusional, diffusional, ballistic), and the degree of confinement (for cell work in particular). The size of the array influences the magnitude due to the averaging that is inherent as the arrays increase in size. The observed motion of one bead will be greater than the motion of the average of 10 beads. A simple

analogy would be motion of a crowd in a stadium. The average motion of the entire crowd is static, the stadium remains full. However, the motion of any given individual will vary greatly. This phenomena was recently reported by Parry et al. (2014) and recapitulated herein. Thus, in studies where time constants are being deduced for models of motion, the size of the arrays must be considered in the resolution of the measurements.

Homogeneity and function of cohesin in vivo

Cohesin is widely-cited for its function in holding sister chromatids together until the appropriate transition from metaphase to anaphase. In the centromere, cohesin is enriched (3X) (Blat and Kleckner, 1999; Weber et al., 2004) yet sister centromeres are on average 800 nm apart (Pearson et al., 2001). In addition, cohesin appears as a homogeneous structure radially displaced from the spindle axis (Stephens et al., 2011; Yeh et al., 2008). There is little understanding of the positional determinants or the functional attributes for cohesin enrichment at the centromere. ChromoShake provides critical predictions for these conundrums. Firstly, the distribution of cohesin rings represents the thermodynamically favored position that depends on the size of DNA loops. Both cohesin rings and chromatin loops jiggle towards their entropically favored positions. Cohesin rings proximal to the primary axis initially migrate radially outward (Figure 2.3 C, 180 and 200 nm barrels), away from the crowded primary axis. Conversely, chromatin loops crumple toward the axis, pushing cohesin rings toward the primary axis (Figure 2.3, A and B). While it is likely that additional biological components may contribute to its function in cells, the thermodynamic argument reveals that no other components are required for its unique homogeneity and radial position. Secondly, we show that cohesin functions to stiffen the DNA to which it is bound (Figure 2.10, E and F). This is presumably through an excluded volume effect, restricting the DNA from adopting a random coil. Considering the function of centromere as a spring between sister kinetochore and its role in tension sensing, the role of cohesin in stiffening the spring has important biological consequences.

Biological consequences of a slip-link network

Ring complexes cross-linking radial loops impart correlated motion across the centromere (Figure 2.7). In the model, the cohesin rings cross-link different chromatin strands and are free to migrate along the strands. This is a slip-link pulley, reminiscent of “topological gels” that maintain form and flexibility over orders of magnitude of volume changes. Topological gels retain their elastic and tensile moduli

properties over several length scale as well (Granick and Rubinstein, 2004; Okumura and Ito, 2001). The cross-linked organization of the centromere has the effect of dissipating changes in motion at the individual kinetochore microtubule attachments sites across the 32 DNA strands. The time-scale of DNA motion (Figure 2.9) is much faster than the relatively slow microtubule dynamics (micron/min). Therefore, the ensemble of protein rings and individual chromatids behave as a cross-linked network. Cross-linking the network has the attribute of equalizing stochastic dynamics in microtubule growth and shortening across the 16 sister kinetochores. Rather than reading the micromechanics at 32 individual kinetochore-microtubule attachment sites, the mechanics of the system are averaged across multiple kinetochores. This feature reveals the SMC complexes create local networks or domains within a single or multiple chromosomes for specific regulatory processes, such as segregation. Thus, the concentration of SMC's in the pericentromere have the capacity to mold a multi-chain chromosome domain into a topological network uniquely tuned to integrate the stochastics of microtubule dynamics into a singular output for informing the cell of the state of chromosome attachment.

Thermodynamic consequences of radial loops

While the radial-loop structure of chromosomes was first noted over a century ago (Hertwig, 1910) and studied in detail (Diaz et al., 1981), the thermodynamic consequences of that structure remain poorly understood. ChromoShake allows researchers to study how the chromatin structure affects chromosome dynamics in detail. We find that a radial sub-loop structure excludes cohesin molecules from the primary axis as cohesin molecules placed near the primary axis quickly migrate radially outward (Figure 2.3 C). This results is reminiscent of the finding that histones are more quickly turned over in the pericentric region than in the arm region of chromosomes (Verdaasdonk et al., 2012). In addition, the bottle-brush-like shape could also explain the increased turnover of histones as a bottle-brush polymer has increased tension on the primary axis (Lebedeva et al., 2012; Panyukov et al., 2009a; Panyukov et al., 2009b). This tension is evident in our bottlebrush chromatin models as they fail to collapse into a random coil (Figure 2.10, A-D).

ChromoShake has provided novel insights into centromere function. The centromere is not a passive DNA element, but the unique configuration of loops and rings impart stiffness to the structures that undoubtedly are critical elements in the force-balance required for faithful chromosome segregation.

Materials and Methods

ChromoShake workflow and parameters

The ChromoShake simulator parses a configuration file that contains the coordinates of the spherical masses and the polymer and environmental parameters. These configuration files are generated by C++ programs. Users can specify if ChromoShake is run on a CPU or GPU, the frequency that output is written out, and the duration of the simulation. ChromoShake outputs a .out text file that can be parsed by various analysis programs and by programs that render the model. An overview of ChromoShake's workflow is provided in Figure 2.11. A full list of tunable parameters is in Table 2.9.

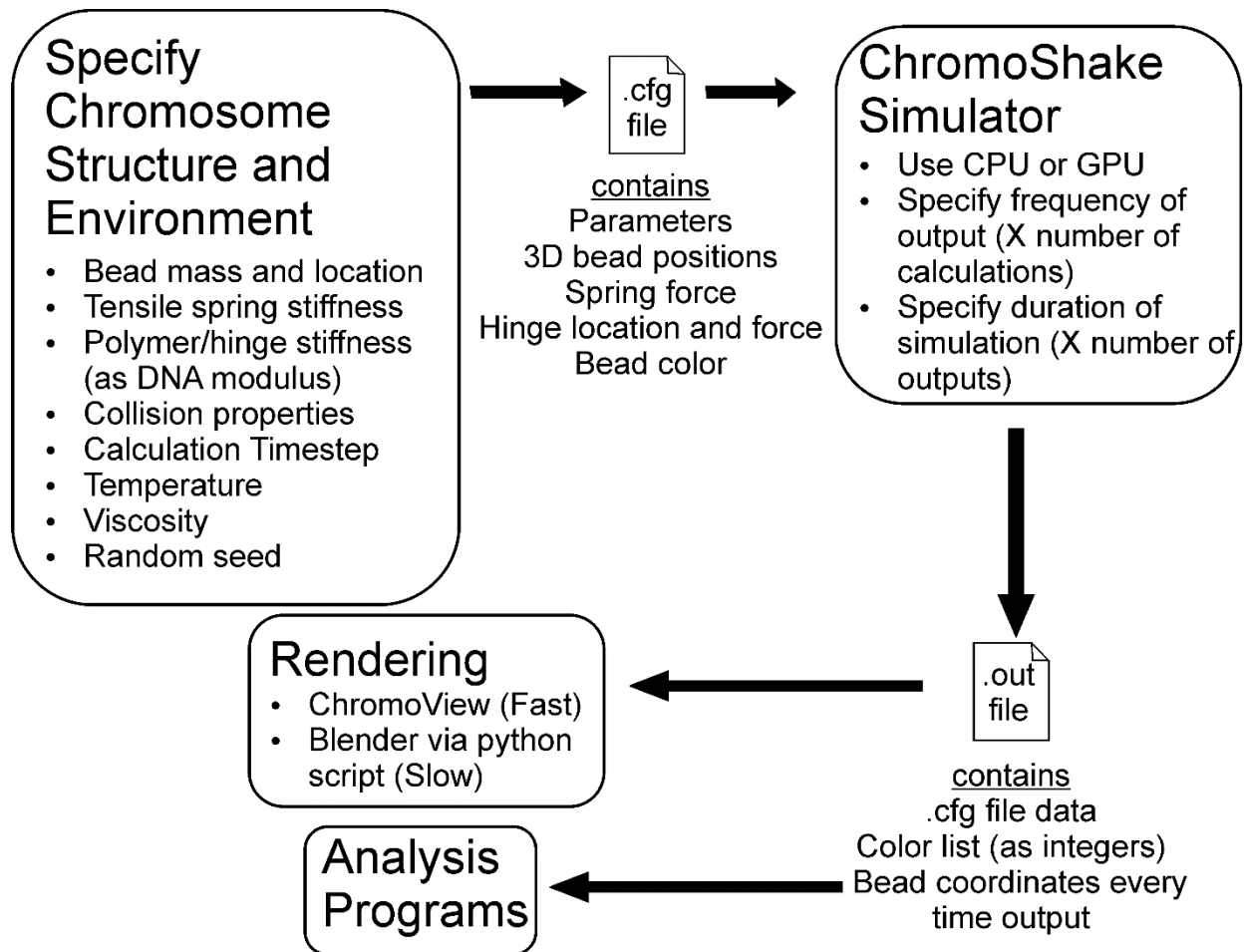


Figure 2.11 – ChromoShake workflow diagram

Polymer dynamics mathematical model

We model a given polymer's conformation by approximating the polymer structure as a number of spherical masses. The dynamics of the polymer's conformation is modeled as the result of deterministic and stochastic forces acting on the masses, yielding a system of stochastic differential equations which can be numerically integrated to simulate the polymer system. We proceed to describe these forces, which model the bending rigidity and tensile stiffness of the polymer, the friction and thermal fluctuations the polymer experiences, and the result of collisions involving the polymer.

Bending rigidity

The polymer model possesses the bending rigidity of B-form DNA. *In vivo*, DNA is compacted into chromatin fibers. The reported bending rigidity of chromatin, typically expressed as a persistence length, is only marginally different than the 50 nm for B-form DNA (Cui and Bustamante, 2000; Dekker et al., 2002), indicating the bending mechanics is dominated by the DNA linkers. We therefore use the DNA bending rigidity values as the default value for our simulation parameters. The bending rigidity parameters for the simulation are determined by first treating the DNA as an elastic beam and applying standard Euler-Bernoulli beam theory (Figure 2.12). The restoring forces as determined through the continuum picture are then translated into a hinge rigidity within the discretized model of the simulation.

We estimate the bending induced restoring forces for each mass within the bent chain using Euler-Bernoulli beam bending theory. Our estimate is based on the case of a simply supported beam (Figure 2.12) with force applied at its center. These boundary conditions provide well defined restoring forces at each end and at the center of the beam. For the simply supported beam with central load case shown in Figure 2.12, the relation between the central loading force and the resultant tangent angle at each end is given by (Roark and Young, 1989):

$$F = \frac{4EI}{d^2} \theta \quad (1)$$

Where E and I are the Young's modulus and moment of area of the beam respectively ($I = \pi r^4/4$ for a beam of circular cross section) and d is the half length of the beam and is a variable that can be tuned within the simulator. For our simulations we use 2 GPa for the Young's modulus, 0.6 nm as the radius of B-form DNA, and 10 nm for d.

Within the model, there will be an elastic restoring force at each mass proportional to the relative angle of adjacent straight segments connecting that mass to its neighbors and in a direction of the bisector of the included angle between segments. A force of half this magnitude and in the opposite direction is applied to both neighboring masses (φ in Figure 2.12 D). Figure 2.12 illustrates how within the mass chain each hinge angle is defined and the corresponding restoring forces associated with each hinge bend. The force magnitude associated with each hinge bend is given by

$$F_N = \frac{2EI}{d^2} \varphi_N \quad (2)$$

is applied to the central and adjacent masses as indicated in Figure 2.12 D.

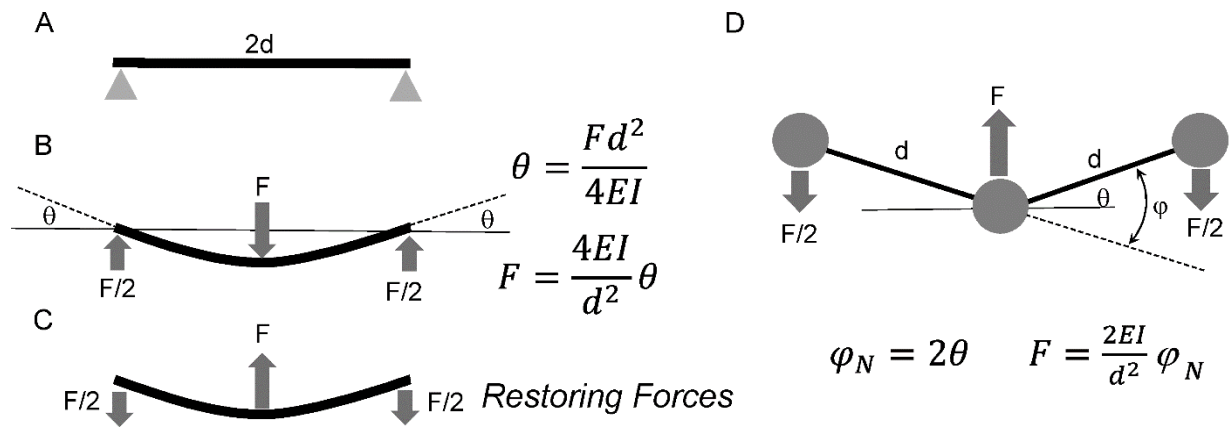


Figure 2.12 – Illustration of hinge forces

(A) Beam simply supported at both ends. (B) Simply supported beam with center load, F . The equations indicate the relationship between the load force and the tangent angle at the beam ends. (C) Beam elastic restoring forces opposing external forces. (D) Translation of continuum model parameters to discretized simulation model with the hinge forces within a simulated chain.

Tensile stiffness

The chain includes a tensile stiffness that resists extension of the segments connecting each mass. Again, we used the literature values for the Young's modulus of DNA to set the magnitude of the segment stiffness. The standard stress vs. strain equation describes tensile stretching of a beam

$$\sigma = E\epsilon \quad (3)$$

$$\sigma = \frac{F}{A} \quad (4)$$

$$\epsilon = \frac{\Delta L}{L_0} \quad (5)$$

Substituting (4) and (5) into (3) and rearranging yields the restoring force for tensile extension, ΔL , of the segments joining each mass.

$$F = \left(\frac{EA}{L_0} \right) \Delta L \quad (6)$$

The quantity within the parentheses of (6) acts as a spring constant for the segments joining the masses. Like a conventional spring, it scales inversely with the length of the segment. For the chosen DNA parameters $E=2\text{GPa}$ and $r=0.6\text{ nm}$, this yields a “spring” constant for each segment of

$$k = \frac{EA}{L_0} = \frac{2.3\text{ nN}}{L_0} \quad (7)$$

Drag force

We describe a drag force on a spherical mass moving with velocity, \vec{v} , by $\vec{F} = -\gamma\vec{v}$, where γ is the drag constant. Due to the spherical shape of the masses and the small Reynolds number system, we obtain the drag constant as a function of our viscosity (η) and the radius of the sphere (a) according to Stokes Law: $\gamma = 6\pi\eta a$. By default, a is 8 nm ($0.8 \times$ node separation of 10 nm).

Thermal fluctuations

The result of thermal fluctuations is inherently stochastic, yielding a Brownian-like motion on individual particles. These fluctuations can be modeled as a normally distributed random force averaged over any chosen time interval, Δt . To estimate the magnitude of the random forces, we first consider the root mean squared (RMS) displacement of a freely-diffusing particle in one dimension:

$$\Delta x_{RMS} = \sqrt{\langle \Delta x^2 \rangle} = \sqrt{2D\Delta t} \quad (8)$$

where Δx_{RMS} is the RMS displacement, D is the diffusion constant of the particle, and Δt is the time interval. The diffusion constant is given by

$$D = \frac{k_B T}{\gamma} \quad (9)$$

where γ is the drag coefficient of the particle. This is the Stokes-Einstein equation relating diffusion with viscous drag. For a real diffusing particle, the thermal force will fluctuate in magnitude and direction and will have a non-zero time average over a given time interval resulting in finite displacement. This time averaged thermal force can be estimated by approximating the motion of the particle over the time interval as directed motion through a viscous fluid. The motive force required to balance the drag force of a sphere moving at speed $v = \Delta x / \Delta t$ is given by

$$F = \gamma v = \gamma \frac{\Delta x}{\Delta t} \quad (10)$$

We set the standard deviation of the random force in one dimension equal to the force in the previous equation. This yields:

$$F_B = \sqrt{\frac{2\gamma k_B T}{\Delta t}} \quad (11)$$

The drag coefficient for a sphere is:

$$\gamma = 6\pi\eta R \quad (12)$$

where η is the fluid viscosity and R is the radius of the sphere (set as bead separation). Thus, over chosen intervals Δt , we model the thermal fluctuations on each sphere as a normally distributed random force with mean centered at zero with a standard deviation of F_B in each dimension.

Collision force

While the spring and hinge forces prevent neighboring masses of the polymer model from crossing through each other, they do not prevent distant sections of the polymer from overlapping. To prevent such behavior, an additional collision force is included in the model. This collision force is modeled as a repulsive Hookean spring force between spheres when they are closer than an equilibrium distance, discouraging spheres from overlapping or crossing through each other. The repulsive force is defined as

$$\vec{F}_c = k_c x \quad (13)$$

where \vec{F}_c is the collision force, k_c is the universal collision spring constant and

$$x = 2R_c - l \quad (14)$$

where R_c is the collision radius and l is the distance between the center of the two masses. When spheres are further apart than the equilibrium distance, $l \geq 2R_c$, the collision force is zero.

Creating geometric models

When constructing the model, we must specify the locations of all the spherical masses and the respective parameters of the forces holding them together. Several spherical masses are defined in three dimensions in external model configuration files that are parsed by ChromoShake. The model configuration files can be created by C++ programs and provide ChromoShake with the relevant polymer information (mass and location of the spherical masses, location and strength of hinges and springs, etc.) and environmental information (temperature and viscosity) to construct and simulate thermal forces on a polymer model. The geometric model of the yeast centromere was based on a 3D geometric model we originally produced using the open-source *Blender* rendering program (Frankel and DePace, 2012). The control points of the splines (sub-loops) were taken from the Blender model and a C++ program was created that generated Non-uniform rational B-splines (NURBs) to re-create its loops. The code was adapted from programs in “An introduction to NURBS” (Rogers, 2001).

ChromoShake program

ChromoShake loads a three-dimensional polymer model, introduces thermal forces, and evolves the state of the model with respect to time by solving the differential equations of motion at a given temperature and viscosity. The solver keeps track of the state (positions and velocities) of a system of multiple spherical masses. Forces are generated to model different types of interactions, which are summed for each mass. Jacobian matrices of the derivative of the forces with respect to the positions and velocities are computed and solved implicitly. The solver describes how the sums of these forces and Jacobians affect the evolution of the system state over discrete time steps. Given the potentially large number of masses (>20,000) in the polymer models, ChromoShake was written in OpenCL to enable parallelization of the code with graphics processing units (GPUs). ChromoShake’s solver uses the conjugate gradient method to solve the linearized implicit equation for position and velocity. The solver was constructed using the ViennaCL sparse linear algebra library <http://viennacl.sourceforge.net/>, enabling it to run in parallel using OpenCL. Moreover, ViennaCL enabled the use of compressed sparse

row sparse matrix data structure, significantly simplifying the differential equation solver algorithm for faster performance.

Collision detection

Given the large number of masses in a polymer model, accelerated collisions detected can be used for large (mass number $\gg 100$) polymer models. Collisions can be detected in two ways using ChromoShake. The simplest but most computationally expensive method is to compare the location of each sphere to the location of every other sphere. To accelerate collision detection, a spatial subdivision scheme was implemented to divide the space in the simulation into a finite grid of three dimensional boxes. The size of these boxes is set so that a mass with whose center is one box can only intersect with masses whose centers are either in the same box or one of the 26 adjacent boxes. The scheme uses a partially parallelized collision detection algorithm for use with GPUs, based off of the GPU gems 3, chapter 32 (Nguyen and NVIDIA Corporation., 2008). This scheme is much faster and is the default scheme for machines with GPUs.

ChromoShake output

The output file from ChromoShake contains three parts. The first is the configuration file that was used to generate and run the model. The second is a series of integers that specify the color of each mass when rendered (used to visually segment the model). The last section contains the X, Y, and Z coordinates of all the simulated masses at each time point.

Rendering ChromoShake output

ChromoShake output files can be rendered in two ways. The first is using the *ChromoView* program that is packaged in the included Windows installer. The second uses a custom python script to convert ChromoShake's output file into a .blend file for the open-source rendering software Blender (<http://www.blender.org>).

Diffusion validation

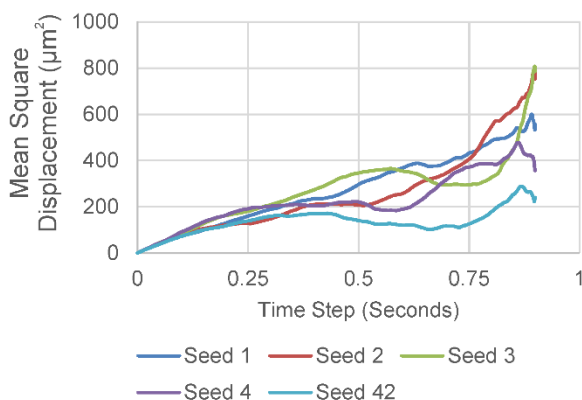
An automated C++ program runs the ChromoShake simulator on 100 spherical masses with collision detection turned off. The lack of collisions therefore makes diffusion from thermal forces the only external force acting on the masses and provides 100 independent replicates per run. The squared displacement of each the beads are calculated over a specified time step. The default time step is 9 ns

with each bead taking 10 steps prior to a mean squared displacement (MSD) calculation. Then the distribution of each beads MSD are compared to the expected values based on

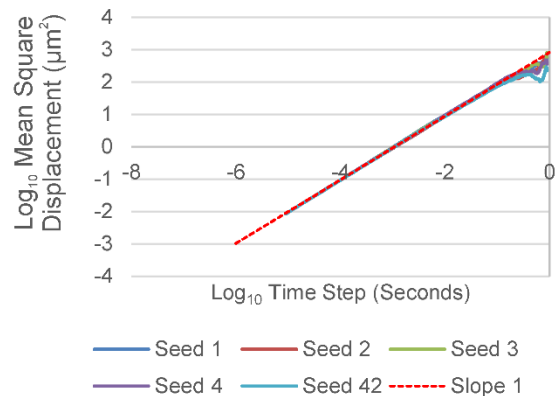
$$\langle r^2 \rangle = \frac{k_B T}{\pi \eta R} \Delta t \quad (15)$$

where k_B is the Boltzmann constant, T is temperature, η is viscosity, R is the radius of the spherical bead, and Δt is the elapsed time (time step times step number, 90 ns) (Figure 2.13). Figure 2.13 B shows that the beads are freely diffusing since plots of the $\log \langle r^2 \rangle / \log \Delta t$ have a slope of approximately 1 (Rubinstein and Colby, 2003; Saxton, 1994). Because diffusion is a random process, given enough iterations approximately half of the values should be below the expected value and half should be above. We define a diffusion simulation as successful if more than 10% of calculated MSDs are greater than and more than 10% are less than the expected value, i.e. the values are distributed around the expected value (Figure 2.13 C).

A



B



C

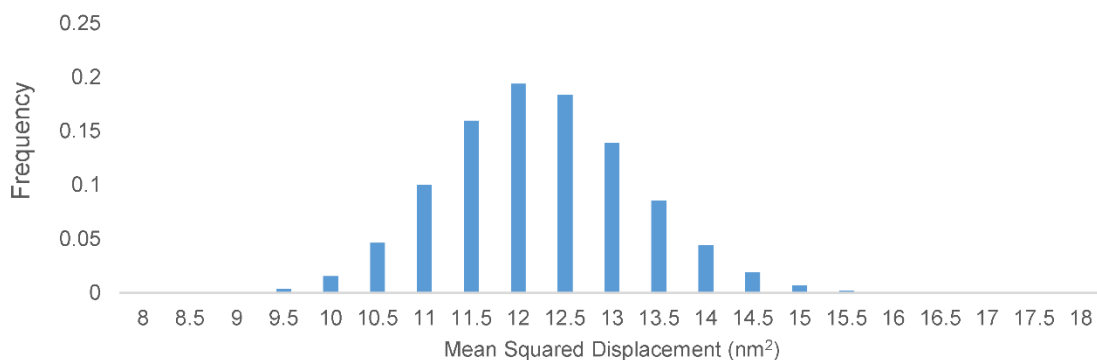


Figure 2.13 – Diffusion Validation

(A) Mean squared displacement curves of diffusing spherical masses. Five separate simulations of a single spherical mass, each with a different random number seed were allowed to diffuse for 0.9 seconds of simulation time. (B) $\text{Log}_{10}/\text{Log}_{10}$ plots of the mean squared displacement curves in A. The slope of 1 is provided to model normal diffusion (Rubinstein and Colby, 2003; Saxton, 1994). (C) Distribution of mean squared displacement of 1 million beads with a 9 ns time step allowed to step 10 times. Expected displacement is 11.8 nanometers squared based on $\langle r^2 \rangle = \frac{k_b T}{\pi \eta R} \Delta t$, where k_b is the Boltzmann constant, T is temperature, 298.15 K, η is viscosity, 0.001 Pa*s, R is the radius of the spherical bead, 10 nm, and Δt is the change in time, 90 ns (time step times step number).

Rouse relaxation time validation

The linear chain models are generated in an extended state and then collapse into a random coil; therefore, we can compare the time it takes for a chain to collapse against the predicted Rouse relaxation time (Rouse, 1953; Rubinstein and Colby, 2003). The Rouse relaxation time is

$$\tau_R = \frac{\eta b^3}{\pi k_B T} N^2 \quad (16)$$

where η is viscosity, b the Kuhn length, k_B the Boltzmann constant, T temperature, and N the number of Kuhn length segments in the chain. The time to collapse, determined by viewing a plot the radii of gyration and end to end lengths over time, were consistent with the calculated Rouse relations times (Figure 2.9). The good agreement between measured and predicted values is a strong indicator that our simulation accurately models polymer dynamics.

Radius of gyration and end-to-end distance validation

Linear polymer models were generated and simulated using ChromoShake. The radius of gyration

$$R_g^2 \stackrel{\text{def}}{=} \frac{1}{N} \sum_{k=1}^N (r_k - r_{\text{mean}})^2 \quad (17)$$

where N is the number of spherical masses, r_k is the position of an individual mass, and r_{mean} is the mean position of all the spherical masses, and end-to-end length, distance between the end masses, was calculated for 1, 2 and 3-micron chains. Radii of gyration and end to end lengths were measured after twice the Rouse time and compared to expected values given

$$\langle R_g \rangle = \sqrt{\frac{Nb^2}{6}} \quad (18)$$

and

$$\langle R \rangle = \sqrt{Nb^2} \quad (19)$$

where b is Kuhn length and N is the number of segments (Rubinstein and Colby, 2003). Average radii of gyration and end to end lengths were similar to expected values (Table 2.10, Figure 2.9).

Table 2.10 – Radius of gyration and average end to end length

	1μm Chain		2μm Chain		3μm Chain	
	Expected	Measured	Expected	Measured	Expected	Measured
Radius of Gyration (nm)	129	95 ± 3	183	148 ± 16	224	183 ± 18
End-to-end length (nm)	316	221 ± 6	447	349 ± 51	548	454 ± 107

Radii of gyration and end to end lengths are $\langle R_g \rangle = \sqrt{\frac{Nb^2}{6}}$ and $\langle R \rangle = \sqrt{Nb^2}$ respectively, where b is Kuhn length and N is the number of segments (Rubinstein and Colby, 2003). All values are averages of three independent simulation runs shown with standard deviation between the runs.

Strain information and growth conditions

The strains KBY8065 (MATa CEN(15)(1.8)-GFP[10kb] ade2-1, his3-11, trp1-1, ura3-1, leu2-3,112, can1-100, LacI-NLSGFP:HIS3, lacO::URA3, Spc29-RFP:Hyg) and KBY9471 (MATa, YEF473a, trp1-63 leu2-1 ura3-52 his3-200 lys2-801, Spc29-RFP:Hyg, Smc3-GFP:URA(pLF639), were grown in rich YPD media with 0.5 mg additional adenine per mL of media to logarithmic phase at 24⁰ C. To deplete ATP from KBY8065, 20 minutes prior to imaging cells were washed and resuspended in YC-complete media containing 0.5 mg additional adenine per mL of media, 0.02% sodium azide, and 1 μ M of deoxy-glucose and incubated at 24⁰ C.

Prior to timelapse imaging, KBY8088 (MATa CEN(3)(1.1)-GFP[1.7kb] ade1 met14 ura3-52 leu2-3, 112 his3-11,15 lys2 Δ ::lacI-GFP-NLS-NAT 1.1 Kb-CEN3::lacO-KAN Spc29-RFP::Hyg) and KBY8065(MATa CEN(15)(1.8)-GFP[10kb] ade2-1, his3-11, trp1-1, ura3-1, leu2-3,112, can1-100, LacI-NLSGFP:HIS3, lacO::URA3, Spc29-RFP:Hyg) were grown in YPD at 24⁰C to log phase.

Microscopy

Cells containing lacO/LacI-GFP (KBY8065) were imaged in in YC-complete media containing 0.02% sodium azide, and 1 μ M of deoxy-glucose for 10 minutes every 30 seconds using a Nikon Eclipse Ti wide-field inverted microscope with a 100x Apo TIRF 1.49 NA objective (Nikon, Melville, New York, USA) and Andor Clara CCD camera (Andor, South Windsor, Connecticut, USA) using Nikon NIS Elements imaging software (Nikon, Melville, New York, USA) at room temperature (25°C). At each interval a 7 Z-plane section image stack with a 400 nm step-size were taken.

Cells containing fluorescently labeled cohesin (KBY9471) were imaged in YC-complete media with 2% filter-sterile glucose using a an inverted, widefield microscope (Eclipse TE2000-U; Nikon) with a 100x Plan Apo 1.4 NA digital interference contrast oil emersion lens with an Orca ER camera (Hamamatsu Photonics, Bridgewater, NJ) with MetaMorph 6.1 software at room temperature (25°C). At each interval a 5 Z-plane section image stack with a 300 nm step-size were taken.

Timelapse microscopy

Cells containing a 1.7 kb lacO/LacI-GFP array 1.1 kb from CEN3 (KBY8088) or a 10 kb lacO/LacI-GFP array 1.8 kb from CEN15 (KBY8065) with spindle pole bodies labeled with Spc29-RFP were imaged in in YC-complete media containing 2% glucose for 180 seconds every 3 seconds. Images

were acquired using a Nikon Eclipse Ti wide-field inverted microscope with a 100x Apo TIRF 1.49 NA objective (Nikon, Melville, New York, USA) and Andor Clara CCD camera (Andor, South Windsor, Connecticut, USA) using Nikon NIS Elements imaging software (Nikon, Melville, New York, USA) at room temperature (25°C). At each interval a single image plane was taken for GFP, 600 ms exposure, and RFP, 600 ms exposure.

Image analysis

The ND2 files were converted to TIFF file format using either Nikon NIS Elements or ImageJ (Rasband, W.S., ImageJ, U. S. National Institutes of Health, Bethesda, Maryland, USA, <http://imagej.nih.gov/ij/>, 1997-2014.). The in-focus planes for each GFP and RFP foci for each Z-stack were determined for each time point and then combined into separate image stacks using Metamorph 7.7 imaging software (Molecular Devices, Sunnyvale, CA, USA). The in-focus GFP and RFP signals were tracked using the MATLAB program Speckle Tracker (Wan et al., 2012; Wan et al., 2009) which is a graphical user interface that detects RFP and GFP foci in an image, tracks the foci through the timelapse, performs 2D Gaussian fitting on a 5x5 pixel region using MATLAB's nonlinear curve-fitting methods (*lsqcurvfit*), and exports the subpixel X and Y coordinate to an Excel spreadsheet (Microsoft, Redmond, WA, USA). The in-focus plane of the cohesin barrel (Smc3-GFP) was defined as the plane with the highest spindle pole body signal intensity using MetaMorph 7.7.

Mean squared displacement analysis

LacO/LacI-GFP and Spc29-RFP foci from timelapse images were tracked using the Speckle Tracker program in MATLAB (The Mathworks; (Wan et al., 2012; Wan et al., 2009). Nuclear/cell motion and microscope drift was removed from the motion of the LacO/LacI-GFP array by subtracting the coordinates of the Spc29-RFP foci from the lacO/LacI-GFP coordinates. The mean squared displacement of the Spc29-RFP subtracted lacO/LacI-GFP coordinates was calculated for timesteps of 3 to 99 seconds from 180 second timelapse images.

Statistical analysis

Calculation of radial displacement was performed using the C++ program cohesin_analysis.cpp. This program calculates all of the distances from the origin (center of the model in Figure 1C) for the beads specified by an input file. The program then calculates the mean distance, the max distance, and

the minimum distance for each time point and then prints the information. Calculating the average position for multiple bead arrays was done using the C++ `coord_summary.cpp`. Mean squared displacement of bead position and the average positions of arrays was calculated using the PERL script `MSD_3D.pl`. The correlated motion of the average position of the simulated 6.8 kb array was performed using a custom MATLAB (The Mathworks, Natick, MA, USA) script with the *corrcoef* function. Heatmaps of experimental and simulated data were generated using two custom MATLAB scripts. Heatmaps of experimental data were performed on the sub-pixel coordinates generated from the Speckle Tracker MATLAB program. Heatmaps of the simulation were generated using a custom MATLAB program that parsed the coordinates from a ChromoShake output file, calculated the distance of each X-coordinate from the proximal spindle pole body, and calculated the distance of each Y-coordinate from the spindle axis. The spindle length was set as the average spindle length, 1.27 μm , from population of the azide and deoxy-glucose treated cells. Both experimental and simulated heatmaps were mirrored about the Y-axis. Only the center 200 nm of the Z-axis was sampled for simulated heatmaps. Radius of gyration analysis of bottle brush polymers and the circular chromatin polymer was performed using a custom MATLAB script. Radius of gyration analysis for polymer chains was performed using the C++ program `radius_of_gyration.cpp`. Tukey's honest significant difference test was performed using the functions *anova1* and *multcompare(stats,'alpha',0.05,'ctype','hsd')* in MATLAB. The mean diameter of individual cohesin rings were calculated by multiplying the mean radius of gyration that was calculated using custom MATLAB programs by two. For cohesin not encompassing chromatin, three independent simulations were run for 0.05 seconds of simulation time. For cohesin encompassing a single chromatin strand, one simulation with 10 cohesin rings on the same circular chromatin strand was run for 0.08 seconds of simulation time. For cohesin encompassing two chromatin strands, the 48 cohesin rings of the centromere model that was run for 0.10653 seconds of simulation time were measured. The mean diameter for the final 2000 timepoints of each simulation were calculated. The ensemble mean and standard deviation between the time-averaged diameters of each cohesin ring were reported in Table 2.1.

REFERENCES

- Anderson, M., J. Haase, E. Yeh, and K. Bloom. 2009. Function and assembly of DNA looping, clustering, and microtubule attachment complexes within a eukaryotic kinetochore. *Mol Biol Cell*. 20:4131-4139.
- Blat, Y., and N. Kleckner. 1999. Cohesins bind to preferential sites along yeast chromosome III, with differential regulation along arms versus the centric region. *Cell*. 98:249-259.
- Bloom, K.S. 2008. Beyond the code: the mechanical properties of DNA as they relate to mitosis. *Chromosoma*. 117:103-110.
- Chacon, J.M., S. Mukherjee, B.M. Schuster, D.J. Clarke, and M.K. Gardner. 2014. Pericentromere tension is self-regulated by spindle structure in metaphase. *J Cell Biol*. 205:313-324.
- Cui, Y., and C. Bustamante. 2000. Pulling a single chromatin fiber reveals the forces that maintain its higher-order structure. *Proc Natl Acad Sci U S A*. 97:127-132.
- D'Ambrosio, C., C.K. Schmidt, Y. Katou, G. Kelly, T. Itoh, K. Shirahige, and F. Uhlmann. 2008. Identification of cis-acting sites for condensin loading onto budding yeast chromosomes. *Genes Dev*. 22:2215-2227.
- Dekker, J., K. Rippe, M. Dekker, and N. Kleckner. 2002. Capturing chromosome conformation. *Science*. 295:1306-1311.
- Diaz, M.O., G. Barsacchi-Pilone, K.A. Mahon, and J.G. Gall. 1981. Transcripts from both strands of a satellite DNA occur on lampbrush chromosome loops of the newt *Notophthalmus*. *Cell*. 24:649-659.
- Frankel, F., and A.H. DePace. 2012. Visual strategies : a practical guide to graphics for scientists & engineers. Yale University Press, New Haven Conn. ; London. 153 p. pp.
- Glynn, E.F., P.C. Megee, H.G. Yu, C. Mistrot, E. Unal, D.E. Koshland, J.L. DeRisi, and J.L. Gerton. 2004. Genome-wide mapping of the cohesin complex in the yeast *Saccharomyces cerevisiae*. *PLoS Biol*. 2:E259.
- Granick, S., and M. Rubinstein. 2004. Polymers: a multitude of macromolecules. *Nat Mater*. 3:586-587.
- Haase, J., A. Stephens, J. Verdaasdonk, E. Yeh, and K. Bloom. 2012. Bub1 kinase and Sgo1 modulate pericentric chromatin in response to altered microtubule dynamics. *Curr Biol*. 22:471-481.
- Hertwig, O. 1910. Lehrbuch der Entwicklungsgeschichte des Menschen und der Wirbeltiere. G. Fischer, Jena., xvi,786p. pp.
- Hu, B., T. Itoh, A. Mishra, Y. Katoh, K.L. Chan, W. Upcher, C. Godlee, M.B. Roig, K. Shirahige, and K. Nasmyth. 2011. ATP hydrolysis is required for relocating cohesin from sites occupied by its Scc2/4 loading complex. *Curr Biol*. 21:12-24.
- Laloraya, S., V. Guacci, and D. Koshland. 2000. Chromosomal addresses of the cohesin component Mcd1p. *J Cell Biol*. 151:1047-1056.
- Lawrimore, J., P.A. Vasquez, M.R. Falvo, R.M. Taylor, 2nd, L. Vicci, E. Yeh, M.G. Forest, and K. Bloom. 2015. DNA loops generate intracentromere tension in mitosis. *J Cell Biol*. 210:553-564.

- Lebedeva, N.V., A. Nese, F.C. Sun, K. Matyjaszewski, and S.S. Sheiko. 2012. Anti-Arrhenius cleavage of covalent bonds in bottlebrush macromolecules on substrate. *Proc Natl Acad Sci U S A*. 109:9276-9280.
- Megee, P.C., C. Mistrot, V. Guacci, and D. Koshland. 1999. The centromeric sister chromatid cohesion site directs Mcd1p binding to adjacent sequences. *Mol Cell*. 4:445-450.
- Michaelis, C., R. Ciosk, and K. Nasmyth. 1997. Cohesins: chromosomal proteins that prevent premature separation of sister chromatids. *Cell*. 91:35-45.
- Nguyen, H., and NVIDIA Corporation. 2008. GPU gems 3. Addison-Wesley, Upper Saddle River, NJ. I, 942 p. pp.
- Okumura, Y., and K. Ito. 2001. The polyrotaxane gel: A topological gel by figure-of-eight cross-links. *Adv Mater*. 13:485-+.
- Panyukov, S., E.B. Zhulina, S.S. Sheiko, G.C. Randall, J. Brock, and M. Rubinstein. 2009a. Tension amplification in molecular brushes in solutions and on substrates. *J Phys Chem B*. 113:3750-3768.
- Panyukov, S.V., S.S. Sheiko, and M. Rubinstein. 2009b. Amplification of tension in branched macromolecules. *Phys Rev Lett*. 102:148301.
- Parry, B.R., I.V. Surovtsev, M.T. Cabeen, C.S. O'Hern, E.R. Dufresne, and C. Jacobs-Wagner. 2014. The bacterial cytoplasm has glass-like properties and is fluidized by metabolic activity. *Cell*. 156:183-194.
- Pearson, C.G., P.S. Maddox, E.D. Salmon, and K. Bloom. 2001. Budding yeast chromosome structure and dynamics during mitosis. *J Cell Biol*. 152:1255-1266.
- Quammen, C.W., A.C. Richardson, J. Haase, B.D. Harrison, R.M. Taylor, 2nd, and K.S. Bloom. 2008. FluoroSim: A Visual Problem-Solving Environment for Fluorescence Microscopy. *Eurographics Workshop Vis Comput Biomed*. 2008:151-158.
- Roark, R.J., and W.C. Young. 1989. Roark's formulas for stress and strain. McGraw-Hill, New York. xiv, 763 p. pp.
- Robinett, C.C., A. Straight, G. Li, C. Wilhelm, G. Sudlow, A. Murray, and A.S. Belmont. 1996. In vivo localization of DNA sequences and visualization of large-scale chromatin organization using lac operator/repressor recognition. *J Cell Biol*. 135:1685-1700.
- Rogers, D.F. 2001. An introduction to NURBS : with historical perspective. Morgan Kaufmann Publishers, San Francisco. xvii, 324 p. pp.
- Rouse, P.E. 1953. A Theory of the Linear Viscoelastic Properties of Dilute Solutions of Coiling Polymers. *Journal of Chemical Physics*. 21:1272-1280.
- Rubinstein, M., and R.H. Colby. 2003. Polymer physics. Oxford University Press, Oxford ; New York. xi, 440 p. pp.
- Saxton, M.J. 1994. Anomalous diffusion due to obstacles: a Monte Carlo study. *Biophys J*. 66:394-401.
- Snider, C.E., A.D. Stephens, J.G. Kirkland, O. Hamdani, R.T. Kamakaka, and K. Bloom. 2014. Dyskerin, tRNA genes, and condensin tether pericentric chromatin to the spindle axis in mitosis. *J Cell Biol*.

- Stephens, A.D., J. Haase, L. Vicci, R.M. Taylor, 2nd, and K. Bloom. 2011. Cohesin, condensin, and the intramolecular centromere loop together generate the mitotic chromatin spring. *J Cell Biol.* 193:1167-1180.
- Stephens, A.D., C.E. Snider, J. Haase, R.A. Haggerty, P.A. Vasquez, M.G. Forest, and K. Bloom. 2013. Individual pericentromeres display coordinated motion and stretching in the yeast spindle. *J Cell Biol.* 203:407-416.
- Straight, A.F., A.S. Belmont, C.C. Robinett, and A.W. Murray. 1996. GFP tagging of budding yeast chromosomes reveals that protein-protein interactions can mediate sister chromatid cohesion. *Curr Biol.* 6:1599-1608.
- Tanaka, T., M.P. Cosma, K. Wirth, and K. Nasmyth. 1999. Identification of cohesin association sites at centromeres and along chromosome arms. *Cell.* 98:847-858.
- Verdaasdonk, J.S., R. Gardner, A.D. Stephens, E. Yeh, and K. Bloom. 2012. Tension-dependent nucleosome remodeling at the pericentromere in yeast. *Mol Biol Cell.* 23:2560-2570.
- Verdaasdonk, J.S., P.A. Vasquez, R.M. Barry, T. Barry, S. Goodwin, M.G. Forest, and K. Bloom. 2013. Centromere tethering confines chromosome domains. *Mol Cell.* 52:819-831.
- Wan, X., D. Cimini, L.A. Cameron, and E.D. Salmon. 2012. The coupling between sister kinetochore directional instability and oscillations in centromere stretch in metaphase PtK1 cells. *Mol Biol Cell.* 23:1035-1046.
- Wan, X., R.P. O'Quinn, H.L. Pierce, A.P. Joglekar, W.E. Gall, J.G. DeLuca, C.W. Carroll, S.T. Liu, T.J. Yen, B.F. McEwen, P.T. Stukenberg, A. Desai, and E.D. Salmon. 2009. Protein architecture of the human kinetochore microtubule attachment site. *Cell.* 137:672-684.
- Weber, S.A., J.L. Gerton, J.E. Polancic, J.L. DeRisi, D. Koshland, and P.C. Megee. 2004. The kinetochore is an enhancer of pericentric cohesin binding. *PLoS Biol.* 2:E260.
- Weber, S.C., A.J. Spakowitz, and J.A. Theriot. 2012. Nonthermal ATP-dependent fluctuations contribute to the in vivo motion of chromosomal loci. *Proc Natl Acad Sci U S A.* 109:7338-7343.
- Yeh, E., J. Haase, L.V. Paliulis, A. Joglekar, L. Bond, D. Bouck, E.D. Salmon, and K.S. Bloom. 2008. Pericentric chromatin is organized into an intramolecular loop in mitosis. *Curr Biol.* 18:81-90.

CHAPTER 3: ROTOSTEP: A CHROMOSOME DYNAMICS SIMULATOR REVEALS MECHANISMS OF LOOP EXTRUSION¹

Summary

ChromoShake is a three-dimensional simulator designed to explore the range of configurational states a chromosome can adopt based on thermodynamic fluctuations of the polymer chain. Here, we refine ChromoShake to generate dynamic simulations of a DNA-based motor protein such as condensin walking along the chromatin substrate. We model walking as a rotation of DNA-binding heat-repeat proteins around one another. The simulation is applied to several configurations of DNA to reveal the consequences of mechanical stepping on taut chromatin under tension versus loop extrusion on single-tethered, floppy chromatin substrates. These simulations provide testable hypotheses for condensin and other DNA-based motors functioning along interphase chromosomes. Our model reveals a novel mechanism for condensin enrichment in the pericentromeric region of mitotic chromosomes. Increased condensin dwell time at centromeres results in a high density of pericentric loops that in turn provide substrate for additional condensin.

Introduction

There has been a revolution in understanding the higher-order structure and organization of chromosome in the past decade. Several major approaches (3C, ChromEMT, and super-resolution microscopy) are indicative of a disordered array of loopy fibers that emanate from an axial core (Dostie and Bickmore, 2012; Dekker et al., 2013; Ou et al., 2017). The hierarchical models of structural intermediates building from 11 to 30 nm and larger fibers are not borne out in these recent 3D and live-cell studies (Ou et al., 2017). DNA looping was first observed in squash preparations of salamander eggs

¹ This chapter previously appears as an article in Cold Spring Harbor Symposia on Quantitative Biology, Volume LXXXII. The original citation is as follows: Lawrimore, J., B. Friedman, A. Doshi, and K. Bloom. 2017. RotoStep: A Chromosome Dynamics Simulator Reveals Mechanisms of Loop Extrusion. Cold Spring Harb Symp Quant Biol.

under the light microscope by the embryologist Oskar Hertwig in the early 1900s (Hertwig, 1906). Paulson and Laemmli (1977) observed DNA loops when examining chromosome spreads in isolated mammalian cells. In metaphase, the loops emanate from a protein-rich chromosome scaffold. The chromosome scaffold is enriched in topology-adjusting proteins, such as topoisomerase II and the SMC (structural maintenance of chromosomes) proteins, known as condensin (Earnshaw et al., 1985; Hirano, 2006).

Loops are a natural consequence of the entropic fluctuations and excluded volume interactions of tethered polymer chains in a confined space, such as the nucleus (Vasquez et al., 2016). If we consider the genome as a ball of yarn, the formation of loops can be appreciated as chains that randomly collide and wiggle around one another. Energy-requiring processes are also involved in loop formation. The earliest suggestion of loop extrusion came from the trombone model of DNA replication (Sinha et al., 1980; Alberts et al., 1983) and direct visualization of DNA looping at the replication fork (Park et al., 1998). More recently, SMC proteins (e.g., cohesin and condensin), which bind and hydrolyze ATP, have been cited as having loop extrusion potential (Alipour and Marko, 2012). Condensin has garnered attention based on recent studies showing it to be a DNA translocase (Terekawa et al., 2017).

Condensin is composed of five subunits, two coiled-coils SMC2 and 4, a kleisin (Brn1), and two heat-repeat containing proteins (Ycs4 and Ycg1). The heat-repeat proteins are likely to be sites of DNA-binding within the condensin complex. Terekawa et al. (2017) showed the ability of condensin to move processively along linear DNA sheets (Fazio et al., 2008). The challenge ahead is to understand, first, how local motion and topological constraints of the DNA exerted by condensin will be dissipated along the length of a long-chain polymer and, second, how the fluctuating, loopy genome feeds back to the ability of condensin to translocate processively.

ChromoShake is a statistical mechanics model depicting the motions of arrays of bead-springs (DNA) that show Brownian dynamics in a viscous environment (Lawrimore et al., 2016). The simulation has been applied to the centromere in budding yeast to reveal how the density of pericentromeric loops stiffen centromeric chromatin, imparting an active function to the centromere in mitosis (Lawrimore et al., 2016). In previous studies condensin was implemented as static springs (Lawrimore et al., 2016). Here, we introduce a new model, RotoStep, as a first-principles statistical mechanics approach to simulate condensin dynamics. Terekawa et al. (2017) have recently examined the behavior of single condensin

molecules on DNA sheets. Terekawa et al. (2017) provides critical experimental metrics for evaluating results from simulation. Using RotoStep to simulate hand-over-hand motion (e.g., microtubule-based kinesin motor (Kull et al., 1996), our simulations indicate that condensin can translocate along taut linear DNA and compact singly tethered DNA chains. The dynamics of condensin stepping along single-tethered DNA result in extrusion of DNA loops. The same parameters for motor stepping result in drastically different geometries that are dictated by chromatin substrate dynamics. These simulations provide the first glimpse of how loop extrusion might work in living organisms.

Results

Model assumptions

Condensin is a DNA-based motor protein with the ability to translocate along double-stranded DNA at relatively high velocities (60 bp/sec) (Terekawa et al., 2017). To simulate condensin tracking DNA we used the array of bead-springs to depict both the DNA (long chain linear bead-spring configuration) and condensin (bead-spring chain). There are 11 beads in the condensin holocomplex; each bead is ~10 nm in diameter. Condensin is a very flexible molecule, showing a persistence length of ~4 nm (Eeftens et al., 2016), about one-tenth that of DNA (50 nm). The chains of the antiparallel coiled-coils fold back on one another to length of 45 nm. The complex adopts a number of configurations, including circular, V-shaped, and globular. The SMC protein coiled-coils are represented by beads 2–8. To achieve DNA binding, we assert that the heat-repeat proteins (Ycs4, Ycg1) bind DNA (Piazza et al., 2014). These are beads 1 (representing Ycg1, red in Fig. 1) and beads 9 and 10 (representing Ycs4, white and red in Figure 3.1) in simulations. The kleisin (Brn1) is represented as bead 11 (pink, Figure 3.1) between the heat-repeat proteins connected via springs (not shown). This feature provides mechanical linkage between the leading and trailing points of contact.

The RotoStep program parses the coordinates, spring attachments, and indices of all beads in a ChromoShake simulation model. The binding mechanics of condensin changes when the condensin molecule becomes extended. We consider condensin-DNA binding unstable if the distance between 3 beads 2 and 8 is greater than 30 nm. If the distance between beads 2 and 8 is less than 30 nm (Figure 3.1 A), the program determines the distances of the Ycs4-beads, 9 and 10 (right-most white and red beads, Figure 3.1 A), to the Ycg1-bead, 1 (left-most red bead, Figure 3.1 A). The closest Ycs4-bead to

the Ycg1-bead is labeled proximal, and the other distal. A vector is drawn from the center of the proximal Ycs4-bead to the center of the distal Ycs4-bead and extended 10 nm. The proximal Ycs4-bead is bound to the closest DNA bead to this point in space as the previous proximal Ycs4-bead DNA attachment is removed. This results in condensin stepping along the substrate resulting in loop extrusion (Figure 3.1 B).

If the distance between beads 2 and 8 is greater than 30 nm (Figure 3.1 C), the spring constant of the spring connecting the Ycg1-bead to the DNA is weakened 1000-fold. ChromoShake is then run to introduce thermal noise, allowing the springs between kleisin and beads 2 and 8, to pinch the condensin molecule together (Figure 3.1 D). On the next iteration of RotoStep, the Ycg1-bead is joined to the nearest DNA bead with a spring as the previous weak spring is simultaneously deleted. This results in the destabilization of the previous condensin-mediated-loop and causes the Ycg1 end of condensin to bind DNA at a new location. After every iteration of RotoStep, ChromoShake is run on simulations to input thermal noise. The springs and kleisin-based threshold (30 nm) are set to yield processive motion on a doubly tethered substrate (Figure 3.2), as described in Terekawa et al., (2017).

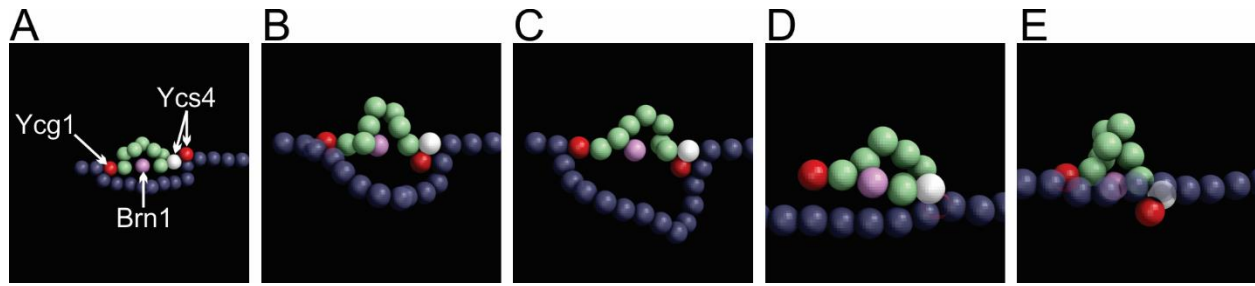


Figure 3.1 – Simulated step and release algorithm

(A) Coiled-coil α -helices of SMC proteins (SMC2,4) are in green. Heat-repeat proteins Ycg1 (left red bead) and Ycs4 (white and right red beads) are bound to DNA (purple beads). The kleisin, Brn1 (pink bead), bridges the SMC containing subunits. (B) One heat-repeat in Ycs4 (white bead) detaches and rebinds DNA depending on the projection of vector (10 nm) between the two heat repeats in Ycs4 relative to Ycg1 (see text). (C) When springs linking kleisin (pink bead) to beads 2 and 8 in the SMC coiled-coils are extended ~ 30 nm, Ycg1 (trailing red bead) is released (shown in D). (E) Rebinding of Ycg1 to DNA following kleisin spring recoil. This results in directed motion on a taut chain.

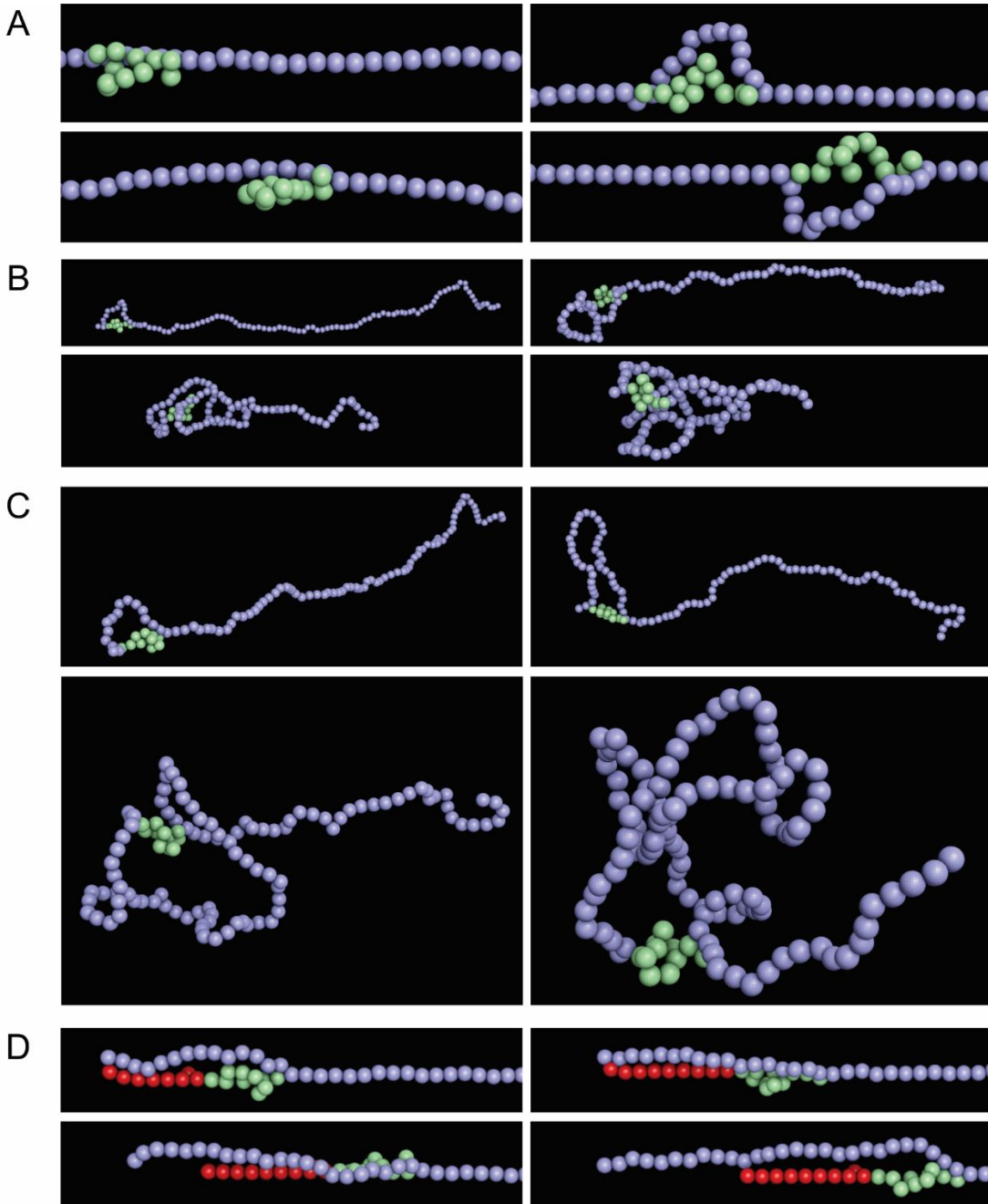


Figure 3.2 – Simulation of condensin walking along a chromatin substrate

(A) Stepping: The DNA (purple beads) with a single condensin (green beads). The DNA ends are tethered to watch how a single condensin molecule steps along the DNA. (B) Looping: The DNA is only tethered at one end, so that its behavior is more like a fluctuating chain *in vivo*. Note that when condensin steps, loops are extruded as a consequence of the floppiness of the chain. (C) Looping (different camera perspective from B). (D) Translocation: Condensin can bind in *cis* (the same molecule) or in *trans* (different molecules). When it binds in *trans* and takes steps, it will move one DNA strand relative to the other. This is a cross-linking and mobilization function. The two DNA strands are depicted in purple and red. The red strand is fluctuating but is equivalent to the mass of lambda DNA (Terekawa et al., 2017), $\sim 10\times$ greater than the mass of the purple beads.

Consequences of processive motion on tethered substrate with cis- and trans-binding

We set our condensin parameters (see materials and methods) such that a single condensin could processively walk on an extended and pinned DNA substrate with a translocation speed of 60 bp/sec as reported in Terekawa et al. (2017). As shown in Figure 3.2 A and Figure 3.3 A–C, upon loading condensin at one end, it processively migrates to the other end of the polymer chain.

Terekawa et al. (2017) reported a singly pinned DNA substrate incubated with condensin resulted in compacted DNA. We confirmed that our RotoStep simulation caused a singly tethered strand to compact (Figure 3.2 B and C, and Figure 3.3 D and E). We added a single condensin to the tethered end of a singly tethered strand (Figure 3.3 D and E). Given that the kleisin spring never becomes taut, the strand is extruded as a loop. After several steps, a loop is spontaneously extruded as the strand adopts a random coil. Despite the random orientation of the floppy strand, which we hypothesized would cause condensin to flip its stepping orientation, a single condensin is able to extrude a loop in a processive manner with simple, proximity-based binding mechanics. This simulation demonstrates loop extrusion is a consequence of processive motion on a floppy substrate. This is an important insight and provides a mechanism for how condensin alters the topology of DNA in vivo to form chromosomes.

Last, Terekawa et al. (2017) reported that condensin is able to proceed along an extended DNA substrate while bound to a separate DNA strand. We replicated this processive motion of a trans-substrate by placing the Ycs4 beads on a doubly tethered strand and the Ycg1 bead on the other strand. In this situation (Figure 3.2 D), as condensin walks, the trans-associated molecule is transported along the substrate molecule, recapitulating the phenomena discovered in Terekawa et al. (2017).

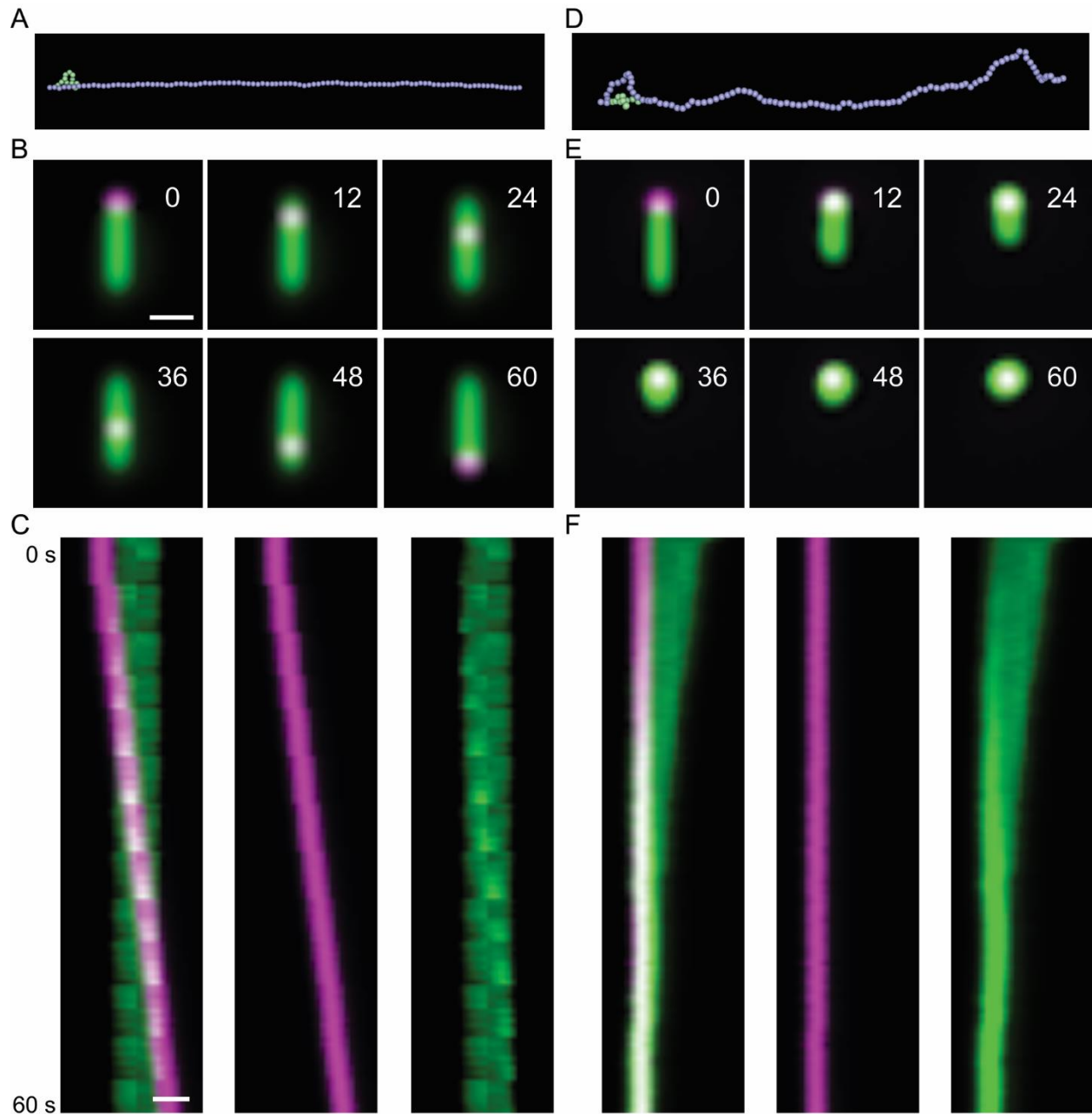


Figure 3.3 – Kymographs of simulated motion convolved through objective point spread function
 Rendering of double-tethered DNA (A) and single-tethered DNA (D), simulations containing a single condensin. Condensin is green; DNA is blue. Time series of simulated fluorescence images of double-tethered (B) and single-tethered (E) simulations. Condensin is magenta; DNA is green. Kymographs of double-tethered DNA (C) and single-tethered DNA (F) simulations. Time is in seconds.

Model convolution

To translate simulations into experimental images, we implement a method known as model convolution (Gardner et al., 2010). We use the microscope objective point spread function to render the simulation into a format that can be directly compared with microscope images of live cells. Figure 3.3 shows the behavior of condensin walking on a pinned DNA substrate. Note the correspondence between this image and those obtained by Terekawa et al. (2017) for condensin translocating on DNA. The extrusion of DNA loops when condensin translocates along an unpinned substrate readily shows that the DNA compacts into a diffraction-limited spot (Figure 3.3 E and F). These simulations (Figure 3.2) and model convolution (Figure 3.3) provide proof of principle that RotoStep can recapitulate the behavior of condensin *in vitro*.

Strand compaction via multiple condensins

In vivo, there are multiple condensin molecules on each chromosome. In budding yeast, the density of condensin is about 1 molecule/10 kb in the bulk of the chromosome and about 1 molecule/3 kb in the pericentromere. We placed 10 molecules of condensin on a single-tethered chain (5 μm , 15 kb). The rules for condensin steps are as previously described, and the step orientation for each molecule is random (Figure 3.4). As individual condensin's take steps, loops are extruded along the strand (as shown for a single molecule, Figure 3.2 C and D), and the strand is rapidly compacted into a chromosome structure. Loop extrusion is independent of the direction that condensin steps. With multiple condensin molecules, as multiple loops form, overall chain length shortens. The backbone is fed into the loops via the step function of each molecule. The surprise is that no new features were implemented beyond the simplest of step functions. Compaction is simply the transfer of the backbone chain into extruded loops (Figure 3.4).

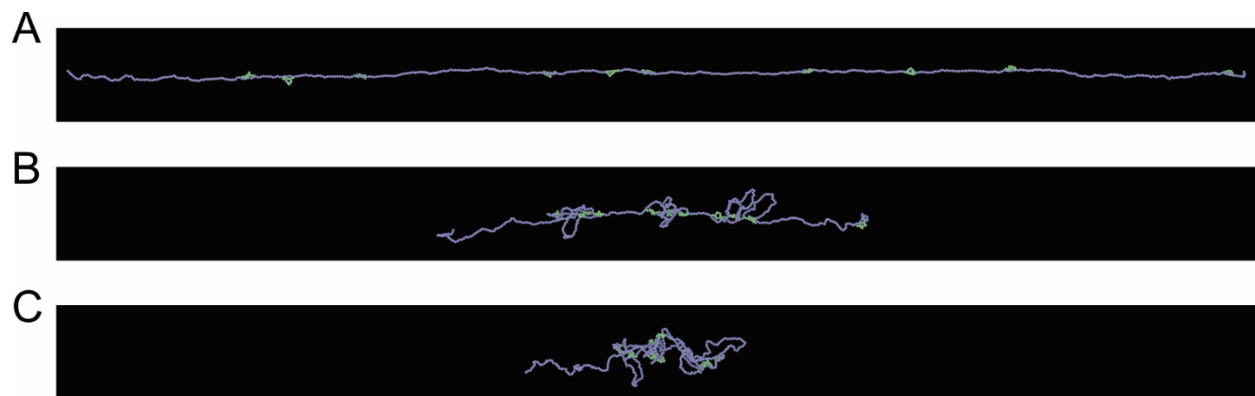


Figure 3.4 – Chromosome compaction

Several condensin molecules were distributed in random position and direction. The DNA molecule is unpinned. As condensin steps (A–C, over time), the DNA gets reeled in and the entire ensemble rapidly condenses into a dense aggregate of DNA and condensin.

Tension along the DNA polymer in a metaphase configuration results in transient, pericentric loops

Centromere DNA is tethered to microtubules via their kinetochore attachment sites. The enrichment of condensin can be visualized *in vivo* as a bar or one or two foci along the spindle axis (Bachellier-Bassi et al., 2008; Stephens et al., 2011; Stephens et al., 2013). To try to gain insight into the thermodynamics governing condensin localization within the pericentromere we provided a dicentric plasmid substrate (two centromeres) for simulation. The actual plasmid is 11.4 kb (~3.86 micron, 386 beads in simulation). The position of the two centromeres (tethered ends) are indicated as pink beads (Figure 3.5) and lie 800 nm from one another, roughly the distance between separated sister kinetochores in budding yeast metaphase (Pearson et al., 2001). The color of beads on the polymer reflect yeast DNA (blue) and a repeat array of tetracycline operator (white) as described in Lawrimore et al. (2015).

In our simulations, condensin walks along the chain as described above, randomly oriented with respect to one another (Figure 3.5). It is difficult for condensin to step through the centromere (simulated as tether sites in pink) because of the geometry of the beads, which increased the dwell time of condensin near the centromeres. Thus, there is kinetic delay for a single condensin molecule at the centromere. This reflects the situation in cells, in which the centromere is at the apex of a stereotypic loop where the kinetochore attaches to microtubules (Yeh et al., 2008). Over time, additional condensin molecules arrive, also extruding loops. The concentration of loops increases and now each condensin can “jump” from one loop to another, amplifying the kinetic delay. The emergent phenomenon is that condensin tends to accumulate near the centromere tether sites. This reflects the density of loops at tether sites. We predict that the accumulation of loops at the centromere reflects the *in vivo* situation. Because of stochastic motion in the loops and condensin stepping, a single condensin molecule will escape one position and start toward the other centromere. At this juncture, the loop density decreases, which biases the remaining condensin molecules to “follow” the initial escapee. *In silico*, this results in condensin molecules “chasing” one another until they accumulate at the other centromere and the cycle continues.

There are several *in vivo* behaviors that now can be accounted for. Condensin appears as foci that could have been interpreted as oligomerization. The alternative explanation based on simple

thermodynamics is that the concentration of condensin reflects the local density of loops. Where loop density is high, condensin will accumulate because of the increase in substrate concentration. The second behavior is the directional instability observed in vivo. This can be accounted for through stochastics of a single molecule that escapes the region of loops. As one molecule leaves, the loop density is reduced triggering a cascade that will allow it to escape and accumulate on the other side.

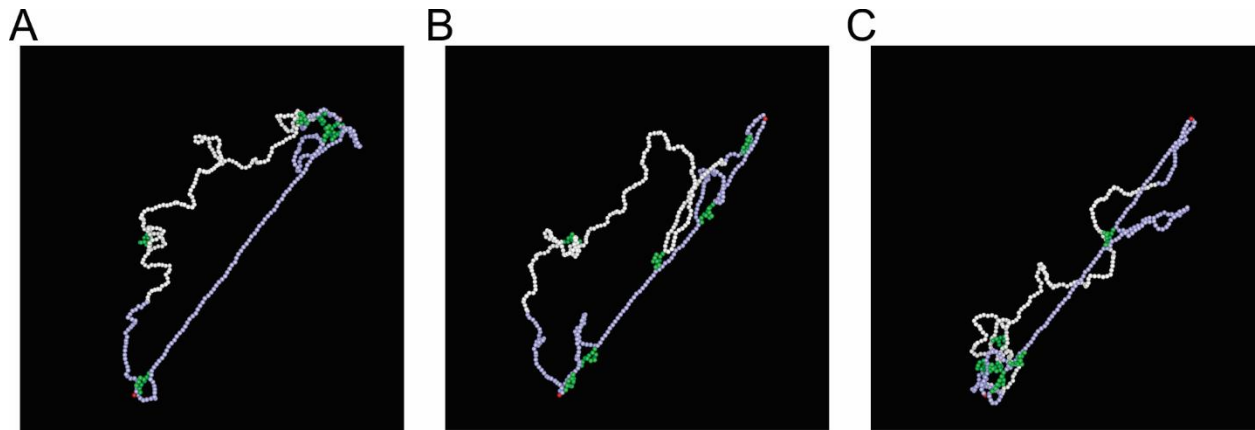


Figure 3.5 – Motion on a dicentric plasmid

A dicentric plasmid in metaphase is simulated by tethering two DNA beads at the position of centromeres within the plasmid (DNA/bead coordinates) and in space at the position of separated kinetochores in yeast metaphase (Lawrimore et al., 2015). The purple beads represent plasmid DNA sequences, the white beads the position of repeat arrays of Tet operator used to visualize with plasmid with TetR-GFP. The number of condensin molecules (green) represents the average density of condensin within the pericentric region of the centromere. Condensin is randomly positioned with respect to DNA sequence and direction. Upon simulated motion (A–C, over time), condensin travels from one tether to the other. Condensin aggregates at the tethers, as a function of the number of loops (i.e., beads). Random fluctuations result in individual molecules migrating from one tether to the other. Once one condensin escapes the aggregate, the DNA density decreases (fewer loops, i.e., fewer beads), biasing additional molecules to migrate away. The appearance is that condensins chase one another. This phenocopies what is observed in live cells, although we cannot observe the behavior of single molecules.

Condensin stepping creates condensin-rich DNA loops near tethered centromeres

We performed statistical analysis on two dicentric plasmids with the same initial placement of condensin, but with mobile (Figure 6 A and B) and immobile condensin (Figure 6 C and D). The probability distribution of condensin (Figure 6 A and C) and DNA beads (Figure 6 B and D) over all time points of the simulations are shown. In simulations with dynamic condensin there is a greater correlation between condensin number and DNA-strand density than immobile condensin (Figure 6 E). Mobile condensin colocalizes with centromeres more often than immobile condensin (Figure 6 F). The enrichment of condensin observed at centromeres may be due to the increased condensin dwell time at tether sites, resulting in the accumulation of centromere-proximal DNA loops. These DNA loops in turn increase the concentration of condensin near centromeres, providing a positive-feedback loop. This pattern of condensin is consistent with that observed *in vivo* (Lawrimore et al., 2015). With static condensin, there is more condensin along the axis (Figure 6 A and C). Consequently, the DNA has more freedom of movement, which is reflected in the DNA density distribution being radially displaced from the axis (Figure 6 B and D), recapitulating *in vivo* experiments of the temperature-sensitive condensin mutation *brn1-9* (Stephens et al., 2011).

Figure 3.7 demonstrates that the motion of the substrate confounds the analysis of condensin turnover because of motion of the substrate. Paradoxically, even a highly processive motor does not appear to recover after photobleaching because of a dense, floppy DNA substrate.

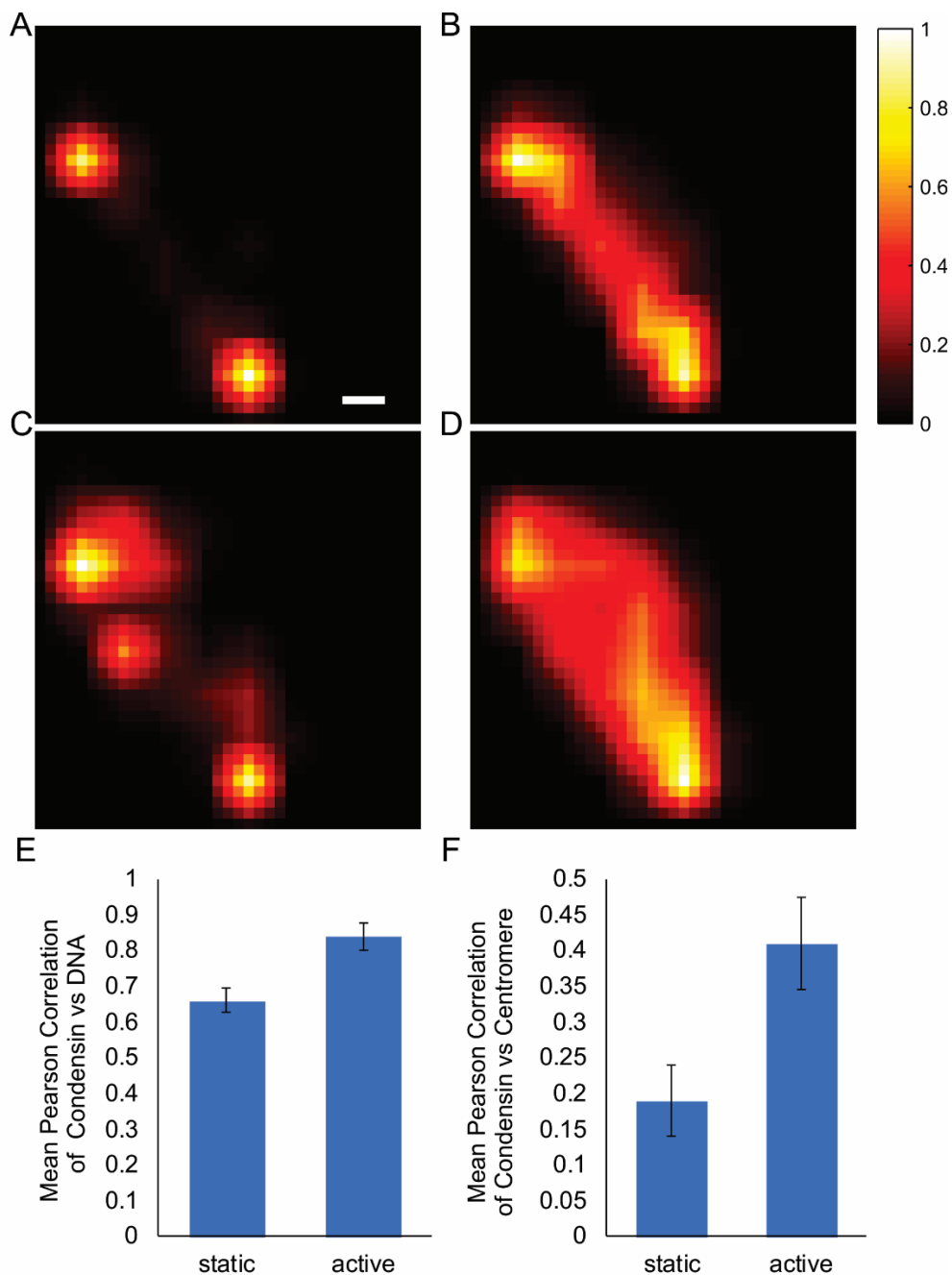


Figure 3.6 – Condensin enrichment at centromere-proximal DNA loops in simulation with mobile vs. immobile condensin

The DNA substrate is the dicentric plasmid described in Figure 3.5 (both ends pinned at centromeres). Condensin is randomly positioned and oriented along the dicentric molecule. Condensin can step along the DNA in A and B, but is static in C and D. The starting positions of condensin are the same in both simulations. A probability density map of condensin is shown in A and C and the plasmid DNA in B and D. (E and F) Statistical analysis of the correlation of condensin with DNA (E) and centromere (tethered beads) (F). Mobile condensin tends to accumulate at the sites of tethering near the centromeres, resulting in condensin-rich, centromere-proximal DNA loops. DNA tends to show greater radial freedom of motion in simulation with mobile condensin (width of B vs. D). Scale bar, 100 nm.

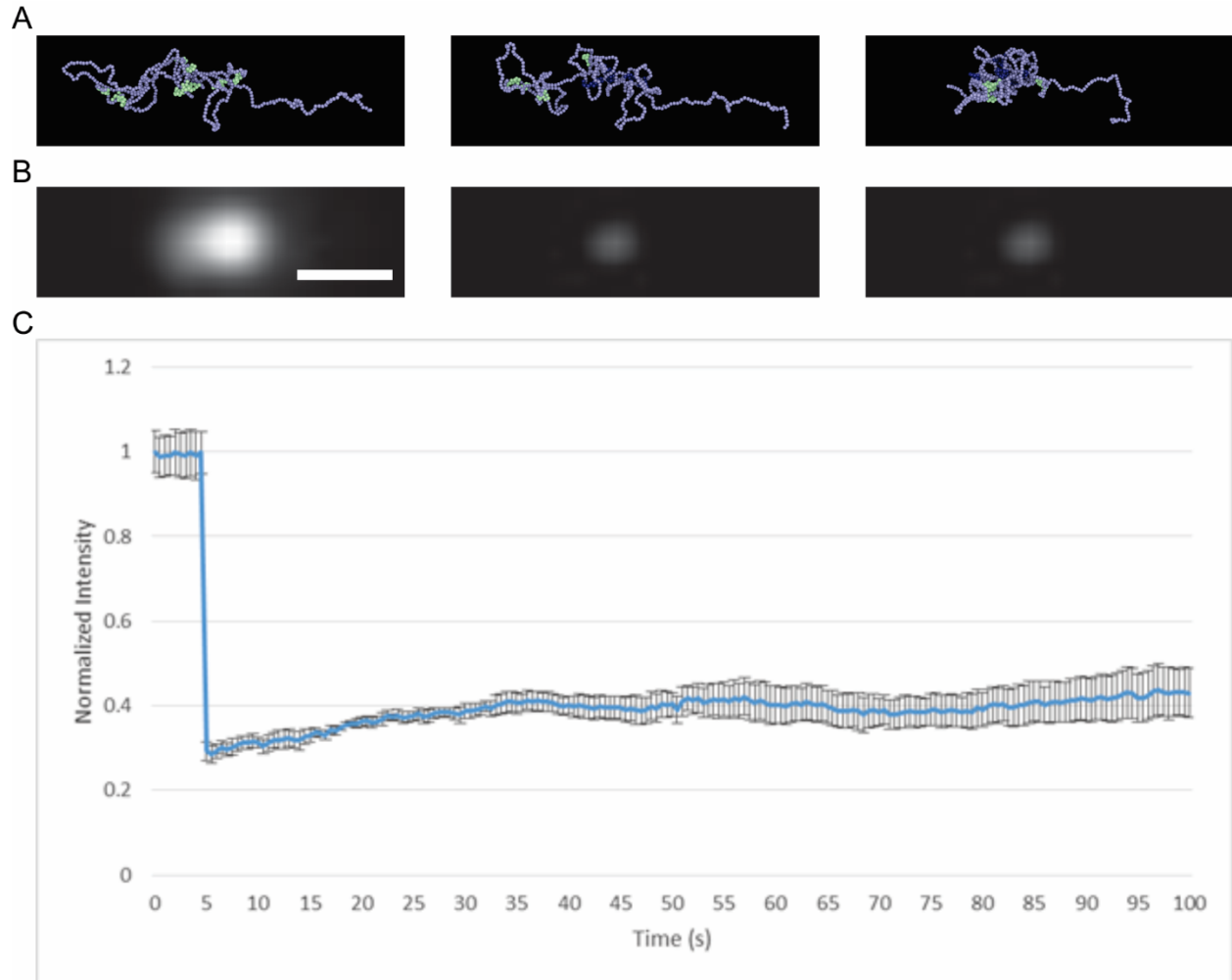


Figure 3.7 – Simulated FRAP experiment by model convolution

Condensin molecules randomly positioned on a 5-kb DNA chain and convolved with the point spread function (PSF) (described above) to simulate a microscopic image. (A) A diffraction limited spot (~250 micron) was drawn around several condensin molecules. Bleaching was simulated by marking these molecules dark (blue). (B) Fluorescence pre- and postbleach (from left to right). Scale bar, 0.5 μm . (C) Mean normalized quantitative fluorescence recovery. Curve is mean of three normalized recovery curves. Error bars are standard error of the mean. The finding in simulation is that any recovery can be attributed to fluctuation of the chain (and associated condensin) into the bleach zone. Thus, FRAP is confounded by the thermodynamics of the substrate. (Compare B to Figure 1.7)

Discussion

We have used a statistical mechanics model of chromatin to examine the consequences of translocation of a motor protein such as condensin on a floppy chromatin substrate. Terekawa et al. (2017) recently reported that condensin is a mechanochemical motor protein. Through simulations that recapitulate in vitro findings we are able to query the consequences of motor stepping on a thermodynamically mobile substrate. Unlike the behavior of motor proteins on DNA sheets under flow, or kinesin-like microtubule-based motor proteins walking on a rigid microtubule, the behavior of the chromatin substrate has a disproportionate contribution to the behavior of a generic DNA-based translocase. Translocation along a floppy substrate is more akin to the random walk of a segment of a fluctuating polymer chain (i.e., subdiffusive Rouse chain (Rubinstein and Colby, 2003)). As the translocase steps, the underlying substrate undergoes fluctuations that randomize the direction of the next step (compare Figures 3.2 and 3.3).

At each step, the chromatin is constantly exploring configurations that maximize entropy. In other words, thermal motion is driving the chain toward a random coil. The net consequence is the extrusion of DNA loops (Figure 3.2 B and C). A key parameter in terms of cell physiology is the stiffness of the chromatin substrate, which can be altered by tethers and the presence of other DNA motors/loop extruders generating regions of taut substrate. If the local substrate is floppy, there will be little if any directed motion. In contrast, if the substrate is stiffer because of extension, the motor will be more prone to display directed motion. The behavior is also dependent on whether the substrate ends are tethered. If not, even a flexible translocase will enhance the ability of the substrate to adopt a random coil (Figure 3.3 E). It is reported that condensin is very flexible (Eeftens et al., 2016) (short persistence length, 4 nm), and thus may show bursts of directed motion in vivo, depending on the distribution of tethers along the chromosome.

A second feature of translocation along a floppy substrate is compaction. Because there is no vectorial motion, the motor will decrease the time required for the chain to adopt a random coil. This may be perceived as active condensation, but it is a natural consequence of random stepping on a thermally fluctuating chain. Likewise, condensin can appear to concentrate in particular locations, such as within the pericentromere and the nucleolus (Bachellier-Bassi et al., 2008; Stephens et al., 2013; Snider et al.,

2014). This has been interpreted as oligomerization between condensin holoenzymes or other cross-linking proteins. The alternative interpretation from the statistical mechanics model is that the concentration of DNA loops increases because of condensin's inability to quickly traverse the centromere region. As condensin steps and extrudes loops, in an environment where there is a plethora of molecules, condensin on one loop can readily step to a physically adjacent loop. This is evident in Figure 3.6, showing accumulation of condensin at sites of tethers, corresponding with increased concentration of DNA loops. Thus, perceived condensin accumulation may reflect the propensity for loops to congregate condensin, which produces more loops. Condensin's ability to step from one loop to another provides a positive-feedback mechanism to increase the duration of these transient events and the local concentration of DNA loops. However, the stochastics of the system will result in occasional molecules escaping sites of loop accumulation by traversing the taut regions of the substrate. As shown in Figure 3.5, when one molecule escapes, the loop density decreases, thus biasing additional molecules to exit sites of loop accumulation. This unstable positive-feedback loop may contribute to condensin's enrichment at the pericentromere and nucleolus *in vivo*. Such a transient, positive feedback may explain the existence of TADs in population studies, but not in single cells (Flyamer et al., 2017). In essence, the organization of the DNA biases the occasional enrichment of condensin based on the presence of a tether causing a loop.

The statistical mechanics of polymer behavior and protein translocation provides a powerful tool to build intuition for understanding experimental observation and making physically accurate hypotheses. Using the simple assumptions of proximity-based substrate binding and extensional-dependent substrate unbinding, we provide alternative explanations for several experimental observations and make new predictions about the rules for loop persistence and extrusion. The model highlights potential new functions for tethers along the chromosome and how the distribution of tethers will be intimately involved in loop formation at a distance (Figure 3.3 B and E). Finally, the mechanical feedback between loops in the same proximity provides new perspectives on interchromosomal communication.

Materials and Methods

RotoStep parameter description

Persistence length of DNA is 50 nm, set by hinge force. Persistence length of condensin is unset, no hinge force on condensin due to estimates of persistence length of 4 nm. Two heat-repeat subunit are beads 9 and 10. Condensin-to-DNA spring strength is same as DNA (2 GPa), with a rest length of 10 nm. One heat-repeat subunit is bead 1. The subunit contains two binding states to DNA beads. The strong state is 2 GPa. The weak state is 2 MPa. The rest length is 10 nm for both states. The weak state is activated when kleisin spring extension is >30 nm. Kleisin is represented by the distance between beads 2 and 8. Beads 2 and 8 are joined by bead 11 and two springs (i.e., 2-11-8). Spring strength is 200 MPa. The rest length of springs are 10 nm. Beads 9 and 10 will rotate about each other every 35 μ sec of simulation time for one bead to bind to a new DNA bead. Simulations are run at a viscosity of 0.01 P. Given an estimated nuclear viscosity of 141 Poise (Fisher et al. 2009), 35 μ sec of simulation time is equivalent to 0.5 sec. Given that the most common step size is one bead per rotation, this results in a step rate of 2 beads per second. Each bead represents \sim 30 bp, so condensin has a step rate of 60 bp/sec, as described in Terekawa et al. (2017).

REFERENCES

- Alberts, B.M., J. Barry, P. Bedinger, T. Formosa, C.V. Jongeneel, and K.N. Kreuzer. 1983. Studies on DNA replication in the bacteriophage T4 in vitro system. *Cold Spring Harb Symp Quant Biol.* 47 Pt 2:655-668.
- Alipour, E., and J.F. Marko. 2012. Self-organization of domain structures by DNA-loop-extruding enzymes. *Nucleic Acids Res.* 40:11202-11212.
- Bachellier-Bassi, S., O. Gadai, G. Bourout, and U. Nehrbass. 2008. Cell cycle-dependent kinetochore localization of condensin complex in *Saccharomyces cerevisiae*. *J Struct Biol.* 162:248-259.
- Dekker, J., M.A. Marti-Renom, and L.A. Mirny. 2013. Exploring the three-dimensional organization of genomes: interpreting chromatin interaction data. *Nat Rev Genet.* 14:390-403.
- Dostie, J., and W.A. Bickmore. 2012. Chromosome organization in the nucleus - charting new territory across the Hi-Cs. *Curr Opin Genet Dev.* 22:125-131.
- Earnshaw, W.C., B. Halligan, C.A. Cooke, M.M. Heck, and L.F. Liu. 1985. Topoisomerase II is a structural component of mitotic chromosome scaffolds. *J Cell Biol.* 100:1706-1715.
- Eeftens, J.M., A.J. Katan, M. Kschonsak, M. Hassler, L. de Wilde, E.M. Dief, C.H. Haering, and C. Dekker. 2016. Condensin Smc2-Smc4 Dimers Are Flexible and Dynamic. *Cell Rep.* 14:1813-1818.
- Fazio, T., M.L. Visnapuu, S. Wind, and E.C. Greene. 2008. DNA curtains and nanoscale curtain rods: high-throughput tools for single molecule imaging. *Langmuir.* 24:10524-10531.
- Fisher, J.K., M. Ballenger, E.T. O'Brien, J. Haase, R. Superfine, and K. Bloom. 2009. DNA relaxation dynamics as a probe for the intracellular environment. *Proc Natl Acad Sci U S A.* 106:9250-9255.
- Flyamer, I.M., J. Gassler, M. Imakaev, H.B. Brandao, S.V. Uljanov, N. Abdennur, S.V. Razin, L.A. Mirny, K. Tachibana-Konwalski. 2017. Single-nucleus Hi-C reveals unique chromatin reorganization at oocyte-to-zygote transition. *Nature* 544:110–114.
- Gardner, M.K., B.L. Sprague, C.G. Pearson, B.D. Cosgrove, A.D. Bicek, K. Bloom, E.D. Salmon, and D.J. Odde. 2010. Model Convolution: A Computational Approach to Digital Image Interpretation. *Cell Mol Bioeng.* 3:163-170.
- Hertwig, O. 1906. *Lehrbuch der Entwicklungsgeschichte des Menschen und der Wirbeltiere* (Textbook of developmental history of humans and vertebrates).
- Hirano, T. 2006. At the heart of the chromosome: SMC proteins in action. *Nat Rev Mol Cell Biol.* 7:311-322.
- Kull, F.J., E.P. Sablin, R. Lau, R.J. Fletterick, and R.D. Vale. 1996. Crystal structure of the kinesin motor domain reveals a structural similarity to myosin. *Nature.* 380:550-555.
- Lawrimore, J., J.K. Aicher, P. Hahn, A. Fulp, B. Kompa, L. Vicci, M. Falvo, R.M. Taylor, 2nd, and K. Bloom. 2016. ChromoShake: a chromosome dynamics simulator reveals that chromatin loops stiffen centromeric chromatin. *Mol Biol Cell.* 27:153-166.
- Lawrimore, J., P.A. Vasquez, M.R. Falvo, R.M. Taylor, 2nd, L. Vicci, E. Yeh, M.G. Forest, and K. Bloom. 2015. DNA loops generate intracentromere tension in mitosis. *J Cell Biol.* 210:553-564.

- Ou, H.D., S. Phan, T.J. Deerinck, A. Thor, M.H. Ellisman, and C.C. O'Shea. 2017. ChromEMT: Visualizing 3D chromatin structure and compaction in interphase and mitotic cells. *Science*. 357.
- Park, K., Z. Debyser, S. Tabor, C.C. Richardson, and J.D. Griffith. 1998. Formation of a DNA loop at the replication fork generated by bacteriophage T7 replication proteins. *J Biol Chem*. 273:5260-5270.
- Paulson, J.R., and U.K. Laemmli. 1977. The structure of histone-depleted metaphase chromosomes. *Cell*. 12:817-828.
- Pearson, C.G., P.S. Maddox, E.D. Salmon, and K. Bloom. 2001. Budding yeast chromosome structure and dynamics during mitosis. *J Cell Biol*. 152:1255-1266.
- Piazza, I., A. Rutkowska, A. Ori, M. Walczak, J. Metz, V. Pelechano, M. Beck, and C.H. Haering. 2014. Association of condensin with chromosomes depends on DNA binding by its HEAT-repeat subunits. *Nat Struct Mol Biol*. 21:560-568.
- Rubinstein, M., and R.H. Colby. 2003. *Polymer Physics*. Oxford University Press, Oxford. 441 pp.
- Sinha, N.K., C.F. Morris, and B.M. Alberts. 1980. Efficient in vitro replication of double-stranded DNA templates by a purified T4 bacteriophage replication system. *J Biol Chem*. 255:4290-4293.
- Snider, C.E., A.D. Stephens, J.G. Kirkland, O. Hamdani, R.T. Kamakaka, and K. Bloom. 2014. Dyskerin, tRNA genes, and condensin tether pericentric chromatin to the spindle axis in mitosis. *Journal of Cell Biology*. 207.
- Stephens, A.D., J. Haase, L. Vicci, R.M. Taylor, 2nd, and K. Bloom. 2011. Cohesin, condensin, and the intramolecular centromere loop together generate the mitotic chromatin spring. *J Cell Biol*. 193:1167-1180.
- Stephens, A.D., C.W. Quammen, B. Chang, J. Haase, R.M. Taylor, 2nd, and K. Bloom. 2013. The spatial segregation of pericentric cohesin and condensin in the mitotic spindle. *Mol Biol Cell*. 24:3909-3919.
- Terekawa, T., S. Bisht, J.M. Eeftens, C. Dekker, C.H. Haering, and E.C. Greene. 2017. The condensin complex is a mechanochemical motor that translocates along DNA. *bioRxiv*.
- Vasquez, P.A., C. Hult, D. Adalsteinsson, J. Lawrimore, M.G. Forest, and K. Bloom. 2016. Entropy gives rise to topologically associating domains. *Nucleic Acids Res*. 44:5540-5549.
- Yeh, E., J. Haase, L.V. Paliulis, A. Joglekar, L. Bond, D. Bouck, E.D. Salmon, and K.S. Bloom. 2008. Pericentric chromatin is organized into an intramolecular loop in mitosis. *Curr Biol*. 18:81-90.

CHAPTER 4: CHROMATIN LOOPS CAUSE GEOMETRIC PARTITIONING OF COHESIN AND CONDENSIN¹

Summary

SMC (structural maintenance of chromosomes) complexes condensin and cohesin are crucial for proper chromosome organization. Condensin has been reported to be a mechanochemical motor capable of forming chromatin loops, while cohesin passively diffuses along chromatin to tether sister chromatids. In budding yeast, the pericentric region is enriched in both condensin and cohesin. As in higher eukaryotic chromosomes, condensin is localized to the axial chromatin of the pericentric region, while cohesin is enriched in the radial chromatin. Thus, the pericentric region serves as an ideal model for deducing the role of SMC complexes in chromosome organization. We find condensin-mediated chromatin loops establish a robust chromatin organization, while cohesin limits the area that chromatin loops can explore. Upon biorientation, extensional force from the mitotic spindle drives condensin-bound chromatin from its equilibrium position to the axial core of pericentric chromatin, resulting in amplified axial tension. The axial localization of condensin depends on condensin's ability to bind to chromatin, while the radial localization of cohesin depends on cohesin's ability to diffuse along chromatin. The different chromatin-tethering modalities of condensin and cohesin result in their geometric partitioning in the presence of an extensional force on chromatin.

Introduction

A key characteristic of chromosome organization in higher eukaryotes is a Condensin II rich axial core with more radial distribution of Condensin I (Hirano, 2016). Addition of reconstituted Condensin I to condensin-depleted extracts resulted in the formation of chromosomes with condensin localizing to chromosome axes (Kinoshita et al., 2015). Even upon depletion of nucleosomes in *Xenopus* egg extracts,

¹ This chapter is a manuscript that is currently under review at Molecular Biology of the Cell. The full citation is as follows: Lawrimore, J., Doshi, A., Friedman, B., Yeh, E., and Bloom, K. (2018) Geometric partitioning of cohesin and condensin are a consequence of chromatin loops. Mol Biol Cell. Under Review.

chromatid-like structures formed with condensin present along their axes (Shintomi et al., 2017). Loss of condensin in DT40 cells resulted in larger fluctuations in inter-kinetochore distance during metaphase of mitosis (Ribeiro et al., 2009), demonstrating that condensin enables chromatin to be more resistive to deformation. Studies using 5C and Hi-C techniques have concluded that mitotic chromosomes of higher eukaryotes are composed of a series of chromatin loops (Naumova et al., 2013; Gibcus et al., 2018). Unlike condensin I and II, cohesin, another SMC (structural maintenance of chromosomes) complex, is peripheral to the chromosome axis during early prophase of mitosis in chromosomes of higher eukaryotes (Losada et al., 2000; Hirano, 2012; Liang et al., 2015; Hirano, 2016). The molecular mechanism that localizes condensin but not cohesin to the chromosome axis is not currently understood.

In budding yeast both condensin and cohesin are enriched in the pericentric region (Megee et al., 1999; Tanaka et al., 1999; Glynn et al., 2004; Weber et al., 2004; D'Ambrosio et al., 2008; Hu et al., 2011). As in higher-eukaryotic chromosomes, condensin localizes to the axial core of the pericentric region (Stephens et al., 2011). Disruption of condensin in budding yeast increased fluctuations in spindle length during metaphase (Stephens et al., 2011), demonstrating yeast condensin stiffens axial pericentric chromatin during mitosis. The observation that lacO/LacI-GFP arrays placed within pericentric region of budding yeast were radial when they appeared as foci, but were axial when they appeared extended, lead to the discovery that the pericentric region was highly looped (Stephens et al., 2011). Cohesin is radially displaced from the axis to form a barrel-like distribution (Yeh et al., 2008), indicating cohesin is in the periphery of chromatin loops in yeast. Both higher-eukaryotic chromosomes and the pericentric region have axial condensin, increased resistivity to chromatin deformation due to condensin, a high density of chromatin loops, and radial cohesin. We posit that the pericentric region of budding yeast serves a model of chromosome organization in higher eukaryotes.

Recent studies have shown condensin binds to DNA (Piazza et al., 2014), and can both extrude DNA loops and translocate across taut DNA in a highly processive manner (Terakawa et al., 2017). Simulations of condensin that can translocate across DNA revealed that the mechanism that allows for translocation on a taut substrate also results in loop extrusion on a slack substrate (Lawrimore et al., 2017). In contrast, cohesin has been shown to passively diffuse along taut DNA (Stigler et al., 2016). Here, we combine live-cell microscopy studies with polymer simulations of chromatin enriched with

simulated condensin and cohesin. We find that the different chromatin binding modalities of condensin and cohesin directly influence their geometric localization within chromatin. In the presence of an extensional force, such as a pulling force from the mitotic spindle after biorientation, condensin-mediated chromatin loops drive condensin to the axial region of pericentric chromatin.

Results

Cohesin confines pericentric chromatin

We measured the dynamics of pericentric chromatin using a 10-kb lacO/LacI-GFP array placed 1.8 kb from CEN15 (Figure 4.1 A and B). To separate thermal from ATP-dependent chromatin motion, we depleted cells of ATP by treatment with sodium azide and deoxy-glucose. We imaged metaphase cells every 30 seconds for 10 minutes and tracked the motion of separated sister chromatids relative to each other (Chacon et al., 2014) using Gaussian fitting to determine the centroids of the LacO/LacI-GFP sister foci (Wan et al., 2009; Verdaasdonk et al., 2013; Lawrimore et al., 2015). The 10-kb lacO/LacI-GFP foci localize to the periphery of the pericentric region, colocalize with cohesin, and are radially displaced from condensin (Stephens et al., 2011). Only small-budded cells with bi-oriented sister-chromatid foci with both spindle pole bodies (SPC29-RFP) within the mother were measured (Figure 4.1 B). We quantified the motion and confinement of the of the lacO/LacI-GFP foci by calculating mean squared displacement over time (Figure 4.1 C) and the mean radius of confinement for each strain (Figure 4.1 D). The radius of confinement is based on the variance of the positions of the lacO/LacI-GFP foci over time, and, like MSD, represents the area over which the foci can freely diffuse (Verdaasdonk et al., 2013; Lawrimore et al., 2015). To determine our measurement accuracy, we fixed yeast cells with formaldehyde and tracked the motion of separated lacO/LacI-GFP foci. The mean squared displacement (MSD) curve of the fixed cells exhibited a maximum MSD of 371 nm², well below the curves of the ATP-depleted cells (Figure 4.1 C). Both the MSD curves and the radii of confinement show that lacO/LacI-GFP foci explore a greater area upon depletion of pericentric cohesin (mcm21Δ (Eckert et al., 2007; Ng et al., 2009; Stephens et al., 2011)). However, lacO/LacI-GFP foci do not explore a significantly greater area upon disruption of condensin (brn1-9 (Lavoie et al., 2000)) (Figure 4.1 C and D).

We reasoned that a more deformable pericentric region, due to loss of cohesin or condensin, would allow lacO/LacI-GFP foci to fluctuate more persistently towards or away from each other,

representing compression and extension of the pericentric region respectively. We measured the mean rate of sister chromatin fluctuations by calculating how far the sister foci traveled either toward or away from each other without switching direction and divided that distance by the duration of the persistent motion. Both the cohesin-depleted (*mcm21Δ*) and condensin-disrupted (*brn1-9*) strains had significantly higher mean rates of sister foci fluctuations than WT strains (Figure 4.1 E). These results demonstrate both cohesin and condensin enable pericentric chromatin to resist deformation, but cohesin achieves this by confining the motion of chromatin while condensin does not.

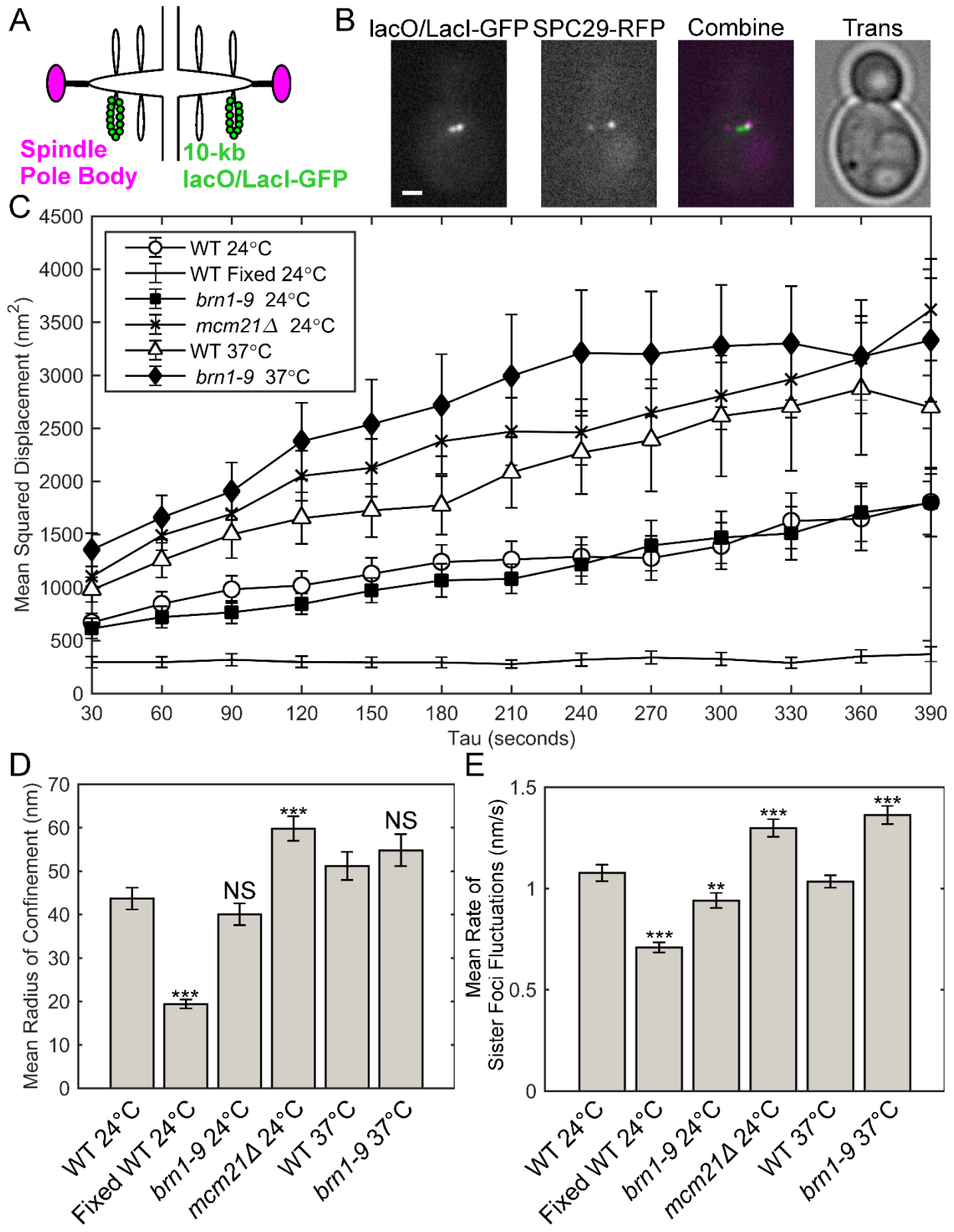


Figure 4.1 – Motion analysis reveals cohesin confines pericentric chromatin while both cohesin and condensin limit rate of sister foci fluctuations

(A) Schematic of the 10-kb *lacO/LacI-GFP* array in the pericentric region during metaphase. (B) Representative images (in-focus planes) of ATP-depleted (sodium azide and deoxy-glucose treated) budding yeast cells in metaphase containing *lacO/LacI-GFP* (green) and *SPC29-RFP* (magenta). Scale bar is 1 μ m. Mean squared displacement curves (C) and bar chart of mean radius of confinement (D) of sister *lacO/LacI-GFP* foci in ATP-depleted, metaphase, cells. WT 24° C n = 36, fixed WT 24° C n = 42, *brn1-9* 24° C n = 46, *mcm21 Δ* 24° C n = 40, WT 37° C n = 49, and *brn1-9* 37° C n = 42 timelapses. Wilcoxon rank-sum test (two-sided) p-values: WT 24 °C vs Fixed WT 24° C = 2×10^{-12} , WT 24 °C vs *brn1-9* 24° C = 0.2, WT 24 °C vs *mcm21 Δ* 24° C = 2×10^{-5} , WT 37 °C vs *brn1-9* 37° C = 0.4. (E) Bar chart of mean rate of sister foci fluctuations. WT 24° C n = 459, fixed WT 24° C n = 538, *brn1-9* 24° C n = 546, *mcm21 Δ* 24° C n = 459, WT 37° C n = 605, and *brn1-9* 37° C n = 543 persistent motion events. Wilcoxon rank-sum test (two-sided) p-values: WT 24 °C vs Fixed WT 24° C = 1×10^{-15} , WT 24 °C vs *brn1-9* 24° C = 0.002, WT 24 °C vs *mcm21 Δ* 24° C = 9×10^{-6} , WT 37 °C vs *brn1-9* 37° C = 2×10^{-8} . All error bars are SEM. Bonferroni correction applied to WT 24° C comparisons such that NS $p \geq 0.017$. *, $p < 0.017$. **, $p < 0.003$. ***, $p < 0.0003$ (see Materials and Methods).

Condensin stiffens centromere proximal chromatin in endogenous chromosomes

To distinguish the roles of cohesin and condensin near the centromere, we obtained population images of cells with a 1.2 kb lacO/LacI-GFP array centered 1.7 kb from CEN3 (Figure 4.2 A and B) in cells with depleted pericentric cohesin (*mcm21Δ*) and disrupted condensin (*brn1-9*). The 1.7-kb array (Figure 4.2 A) is more proximal to the centromere, which defines the pericentric chromatin axis, than the 10-kb array (Figure 4.1 A). Previously, this probe has been used to measure changes in chromatin tension (Pearson et al., 2003; Chacon et al., 2014). Both cohesin depletion (*mcm21Δ*) and condensin disruption (*brn1-9*) caused a significant increase in mean sister foci separation (Figure 4.2 C). However, only condensin disruption (*brn1-9*) resulted in a significant increase in stretch frequency (Figure 4.2 D). These results demonstrate that both cohesin and condensin enable pericentric chromatin to resist deformation, but condensin achieves this by preventing stretching of chromatin while cohesin does not.

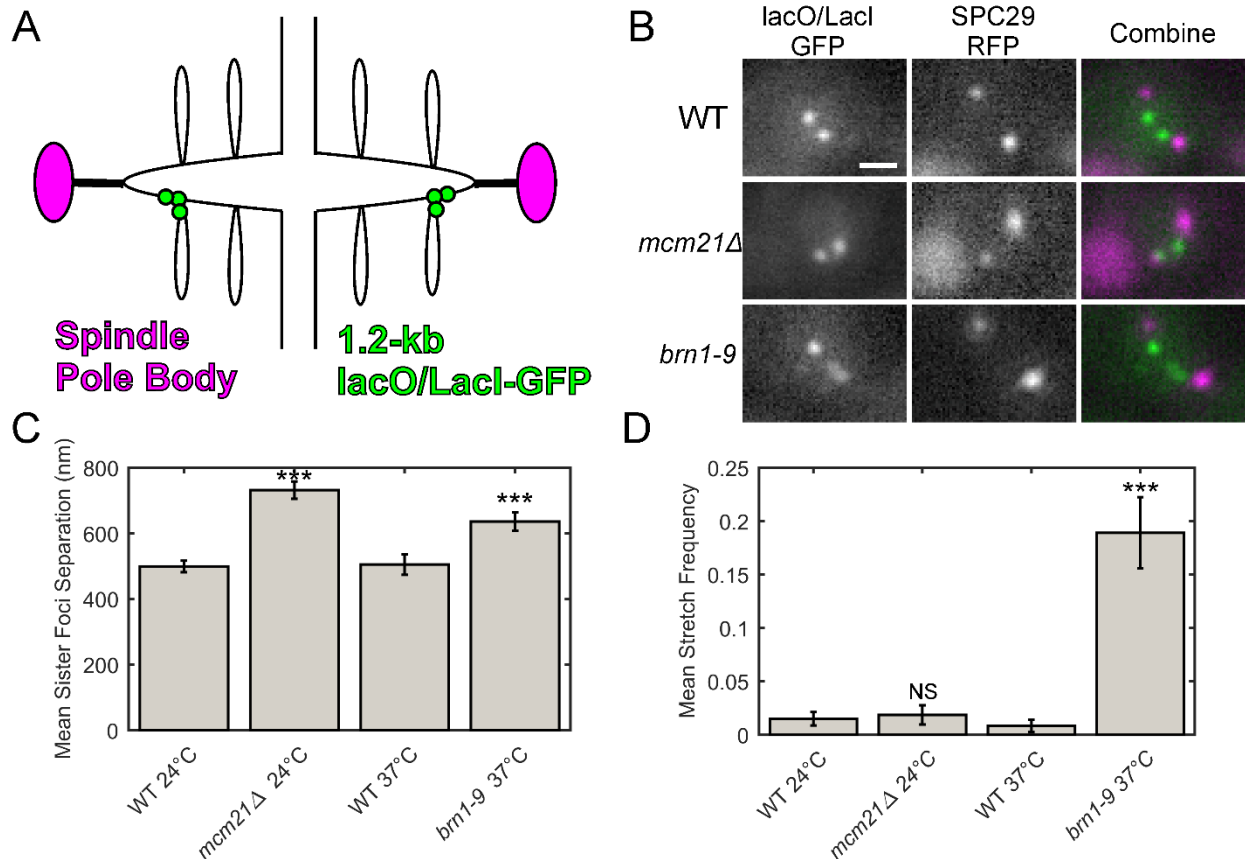


Figure 4.2 – Condensin, not cohesin, stiffens endogenous pericentric chromatin

(A) Schematic of the 1.2-kb lacO/LacI-GFP array in pericentric region during metaphase. (B) Representative images of lacO/LacI-GFP array (green in combine) and SPB protein SPC29-RFP (magenta in combine). Scale bar is 1 μ m. (C) Bar chart of mean sister foci separation. WT 24°C n = 164, *mcm21Δ* 24°C n = 156, WT 37°C n = 74, *brn1-9* 37°C n = 97 cells. Wilcoxon rank-sum test (two-sided) p-values: WT 24°C vs *mcm21Δ* 24°C = 5×10^{-14} , WT 37°C vs *brn1-9* 37°C = 3×10^{-4} . (D) Bar chart of mean stretch frequency. WT 24°C n = 18, *mcm21Δ* 24°C n = 11, WT 37°C n = 16, *brn1-9* 37°C n = 16 image sets. Wilcoxon rank-sum test (two-sided) p-values: WT 24°C vs *mcm21Δ* 24°C = 0.6, WT 37°C vs *brn1-9* 37°C = 1×10^{-5} . All error bars are SEM.

Condensin functions on axial chromatin in the pericentric region

To differentiate the effects of cohesin and condensin on axial chromatin, we obtained timelapses of a conditionally dicentric plasmid labeled with a 5.5-kb tetO/TetR-GFP array (Dewar et al., 2004; Lawrimore et al., 2015) (Figure 4.3 A). After loss of the ARS sequence (see Methods), the plasmid is a single, contiguous molecule of DNA with two active centromeres. Thus, the plasmid acts as a molecular tensometer. We imaged cells every 30 seconds for 20 minutes and measured the length of the tetO/TetR-GFP signals (Figure 4.3 B). The length and aspect ratio of the tetO/TetR-GFP signals and the spindle length were measured using a custom MATLAB GUI (see Materials and Methods).

We found that condensin-disrupted cells (*brn1-9*) had a large increase in mean signal length, while cohesin-depleted cells (*mcm21Δ*) had a smaller but significant increase in the mean signal length (Figure 4.3 C). Histograms of the signal length distributions revealed WT 24° C, *mcm21Δ*, and WT 37° C cells' most frequent signals were between 300-400 nm, at the extreme low-ends of the distributions (Figure 4.3 D and E). However, *brn1-9* cells' most frequent signal lengths were at the center of the distribution (Figure 4.3 E). The signal length distributions WT cells and *mcm21Δ* cells have a statistically better fit with a two-term Gaussian distribution than a single Gaussian distribution (Figure 4.4 A-C). The addition of a second Gaussian distribution failed to improve the fit of the *brn1-9* cells' signal length distribution (Figure 4.4 D). The signal lengths distributions indicate that condensin creates a subpopulation of compacted signals.

We measured the mean rate of signal fluctuations in the same manner as the mean rate of sister foci fluctuations. Increases/decreases in signal length were divided by the duration of the extension/compaction event. Condensin-disrupted cells (*brn1-9*) and cohesin-depleted cells (*mcm21Δ*) had an increased mean rate of signal fluctuations (Figure 4.3 F), consistent with the increase in the mean rate of sister foci fluctuations (Figure 4.1 E) upon loss of cohesin or disruption of condensin. Thus, our results are consistent across different chromatin substrates. However, condensin has a greater impact on the plasmid dynamics than cohesin, suggesting condensin plays a crucial role in enabling axial chromatin to resist deformation.

To examine the relationship between chromatin compaction and chromatin dynamics, we created density maps of the change in signal length after 30 seconds versus the initial signal length (Figure 4.3 G-

H). Condensin-disrupted (*brn1-9*) cells showed a radically altered plasmid dynamics profile compared to WT cells. However, cohesin-depleted cells (*mcm21Δ*) showed a similar plasmid dynamics profile compared to WT cells (Figure 4.3 H, leftmost panels). WT and cohesin-depleted cells (*mcm21Δ*) exhibited a dense cluster of 300-400 nm signal lengths with ± 50 nm changes in their signal lengths that the condensin-disrupted (*brn1-9*) cells lacked completely (Figure 4.3 H). Moreover, the density maps reveal that in cells with functional condensin, plasmids of all signal lengths exhibit smaller changes in signal length than cells with disrupted condensin (Figure 4.3 H). Thus, condensin compacts chromatin into an organization that effectively resists deformation.

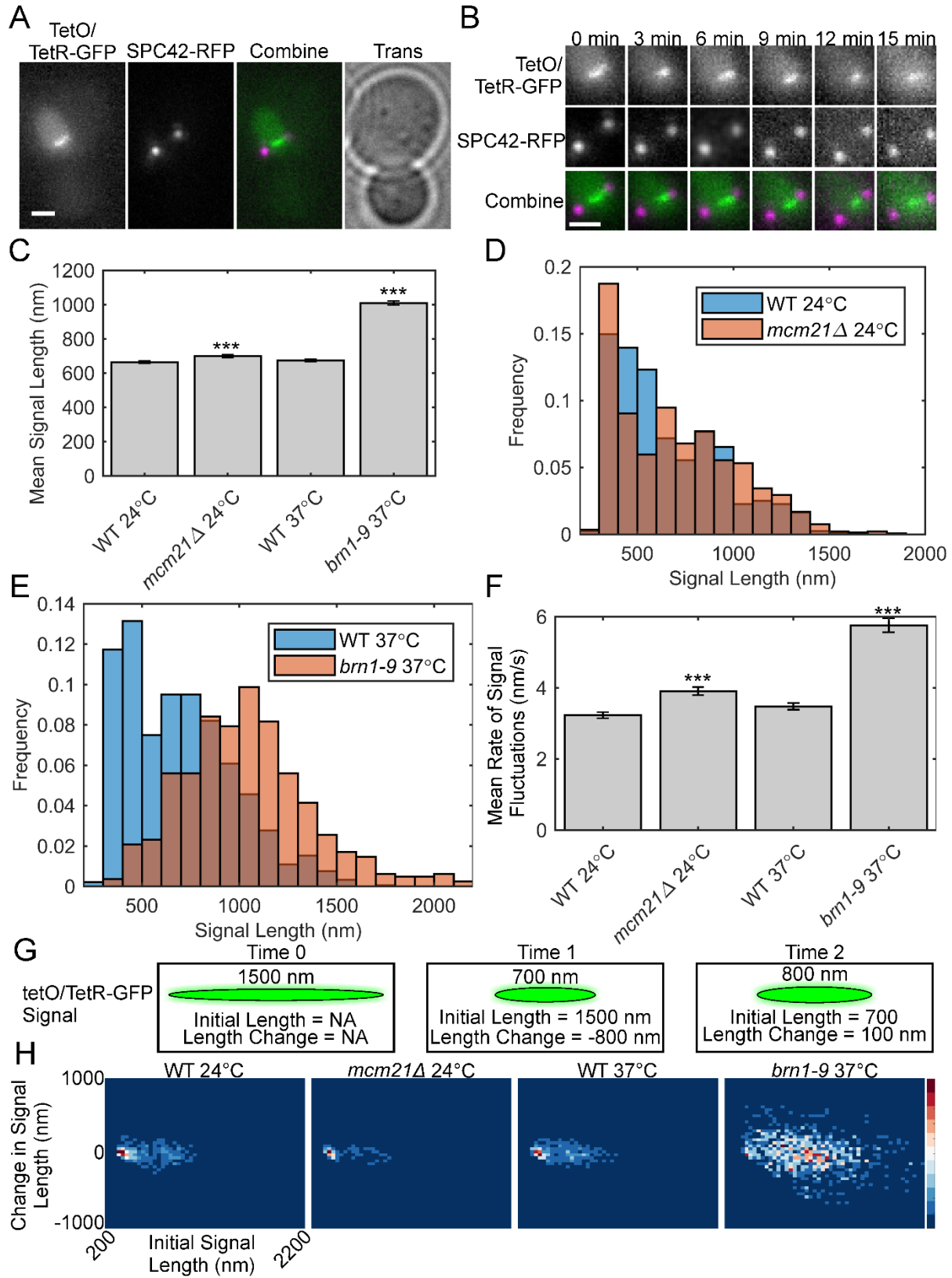


Figure 4.3 – Condensin condenses and stiffens pericentric chromatin

Representative image (A) and montage (B) of a cell containing the fluorescently labeled, conditional dicentric plasmid pT431 and SPB protein SPC42-RFP. The tetO/TetR-GFP image (green in combine) and the SPC42-RFP image (magenta in combine) are maximum intensity projections. The Trans image (A) is in-focus plane. Scale bars are 1 μm . (C) Bar charts of mean signal length of tetO/TetR-GFP array from timelapses. WT 24 $^{\circ}$ C n = 1732, mcm21 Δ 24 $^{\circ}$ C n = 1455, WT 37 $^{\circ}$ C n = 1887, brn1-9 37 $^{\circ}$ C n = 838 plasmid signals. Wilcoxon rank-sum test (two-sided) p-values: WT 24 $^{\circ}$ C vs mcm21 Δ 24 $^{\circ}$ C = 0.01, WT 37 $^{\circ}$ C vs brn1-9 37 $^{\circ}$ C = 3×10^{-121} . (D) Histograms of the signal lengths of the tetO/TetR-GFP arrays for WT cells grown at 24 $^{\circ}$ C (blue) and mcm21 Δ cells grown at 24 $^{\circ}$ C (red). (E) Histograms of the signal lengths of the tetO/TetR-GFP arrays for WT cells grown at 37 $^{\circ}$ C (blue) and brn1-9 cells grown at 37 $^{\circ}$ C (red). (F) Bar charts of mean rate of signal fluctuations of tetO/TetR-GFP array from timelapses. WT 24 $^{\circ}$ C n = 1041, mcm21 Δ 24 $^{\circ}$ C n = 881, WT 37 $^{\circ}$ C n = 1101, brn1-9 37 $^{\circ}$ C n = 495 extension/compaction events. Wilcoxon rank-sum test (two-sided) p-values: WT 24 $^{\circ}$ C vs mcm21 Δ 24 $^{\circ}$ C = 1×10^{-5} , WT 37 $^{\circ}$ C vs brn1-9 37 $^{\circ}$ C = 3×10^{-31} . (G) Cartoon of a three-frame timelapse of a tetO/TetR-GFP array. Initial length refers to the length of the array in the previous timestep. Length change is the amount the signal grew or shrank from the previous timestep. (H) Density maps of change in signal length as a function of initial signal length. Red is most dense, blue is least dense

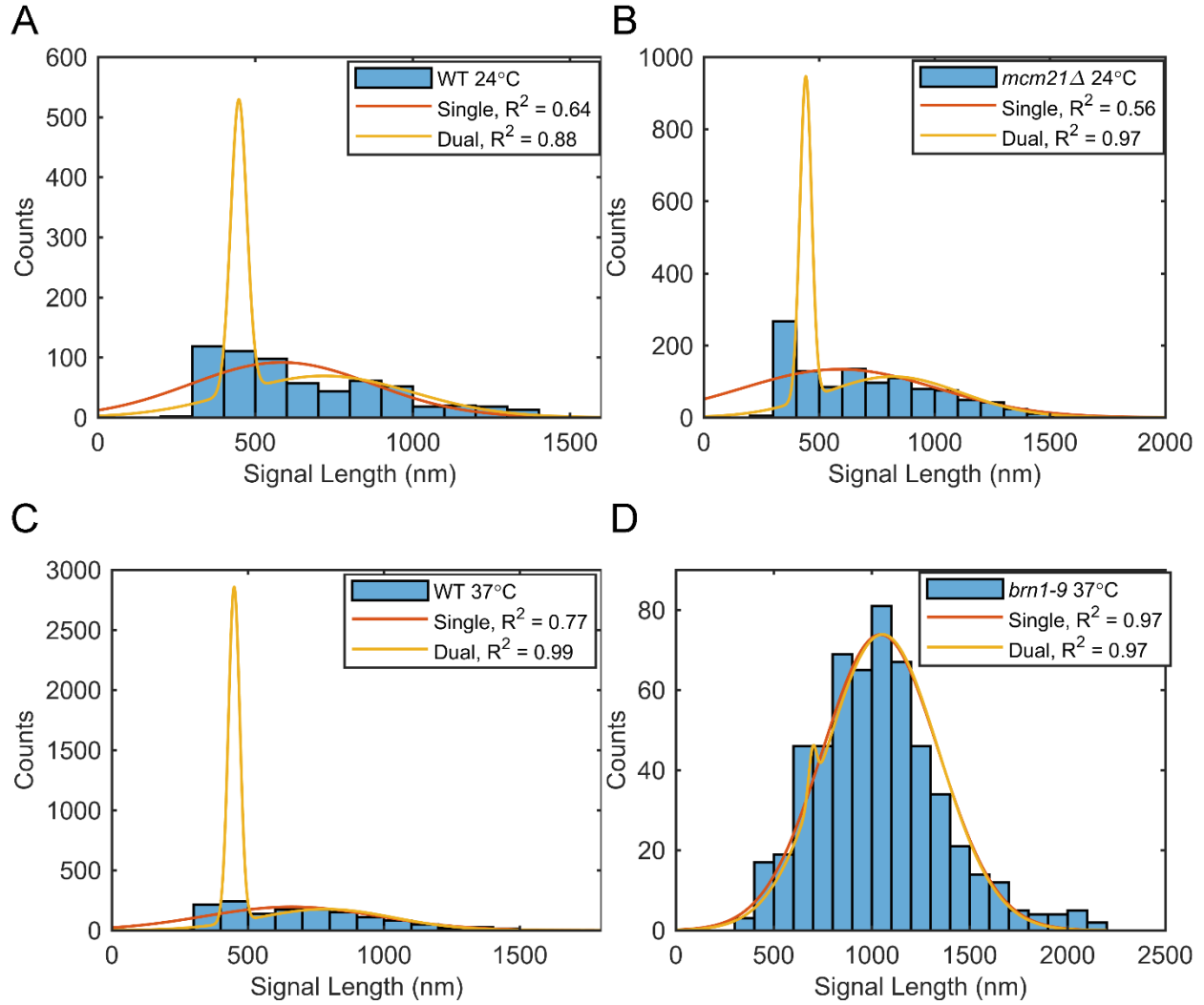


Figure 4.4 – Histograms of dicentric plasmid, tetO/TetR-GFP signal lengths reveals condensin creates subpopulation of compacted signals

Histograms of the signal lengths of the tetO/TetR-GFP array from WT cells grown at 24° C (A), *mcm21Δ* cells grown at 24° C (B), WT cells grown at 37° C (C), and *brn1-9* cells grown at 37° C (D). Histograms were fit with single-term and two-term Gaussian distributions. The goodness of fit is reported as R^2 values.

Simulated dicentric plasmids with condensin-mediated loops condense and stiffen underlying DNA

To determine if a stoichiometric amount of condensin-mediated chromatin loops is sufficient to alter the dynamics of a simulated version of the conditionally dicentric plasmid, we used the polymer dynamics simulator ChromoShake (Lawrimore et al., 2016) to run models of the plasmid with and without condensin complexes. The plasmid simulations do not contain histone compaction. The simulations are based on the length of the plasmid after the ARS sequence is looped out, 11.36 kb. Assuming 0.34 nm per base pair the simulated plasmids are 3860 nm long composed of 386 masses. Given that the typical distribution of condensin is 1 complex per 10 kb with threefold enrichment of condensin within the pericentric region (Megee et al., 1999; Wang et al., 2005; D'Ambrosio et al., 2008), we chose to add 3 condensin complexes to our plasmid simulations. The simulated tetO/TetR-GFP array (green masses, Figure 4.5) was convolved with an experimentally obtained point spread function to generate simulated timelapses of the array (Figure 4.5 D-F). Condensin was simulated as 3 randomly placed linear springs connecting nonconsecutive DNA beads to form static loops (Figure 4.5 B).

Additionally, we simulated condensin as a bead-spring complex capable of extruding loops dynamically on slack chromatin and translocating across taut chromatin (Figure 4.5 C). Each dynamic condensin simulation was run using the chromoShake derived program RotoStep (Lawrimore et al., 2017). RotoStep edits the chromoShake outfile to alter the masses to which condensin binds based on two rules. If the condensin complex is not extended past 30 nm, the two condensin beads that bind to DNA beads, representing Ycs4, rotate to step along the DNA while the condensin bead, representing Ycg1, stays bound to its DNA bead. If the condensin complex is extended past 30 nm, then the Ycg1 bead's connection to the DNA bead weakens 1000-fold, causing condensin's internal spring to bring the Ycg1 bead towards the Ycs4 beads, and then the Ycg1 bead rebinds to the most proximal DNA bead, mimicking condensin "stepping" along the DNA substrate. Condensin's internal spring was set to 0.023 pN to allow condensin to processively step along a taut DNA substrate, not to reflect the stiffness of the condensin holocomplex. We simulated condensin to extrude loops at a rate of 60 bp per second, the same rate as condensin translocation reported in Terekawa et al (2017). The dynamic condensin complexes were not allowed to unbind completely from the DNA in simulations due to the extremely long

dwel time, greater than 10 minutes, of reconstituted condensin on bound to DNA in *in vitro* experiments (Ganji et al., 2018; Terakawa et al., 2017)

Both static and dynamic condensin simulations compacted (Figure 4.6 A) and reduced the mean fluctuations of (Figure 4.6 B) the simulated tetO/TetR-GFP array. The addition of three randomly-positioned, static condensin-mediated loops to the plasmid simulations created a subpopulation of compact array signals (Figure 4.6 C). In contrast, dynamic condensin-mediated loops did not result in a subpopulation of compacted signal lengths. However, fitting the distributions of the simulated signal lengths revealed that the addition of a second Gaussian curve improved the fit of both static and dynamic condensin-mediated loops (Figure 4.7 B and C). However, the dynamic condensin-mediate loop simulations resulted in a second Gaussian peak near the middle of the distribution, while the static condensin-mediated loops placed a second Gaussian peak at more compacted signal lengths like what was observed in WT cells with dicentric plasmids (Figure 4.4 A and C). We combined the simulated signal length distributions with the change in simulated signal length over each 30 timestep to generate heatmaps (Figure 4.6 E). None of the heatmaps of the dicentric plasmid simulations exhibited a large cluster of compacted signals with smaller than average length changes (Figure 4.6 E) that was observed with dicentric plasmids in WT cells (Figure 4.3 H). While both static and dynamic chromatin loops were sufficient to compact and stiffen simulated dicentric plasmids, neither static nor dynamic chromatin loops are sufficient to recapitulate the precise dynamics of a dicentric plasmid within wildtype cells. Thus, in general, loops are sufficient to compact and stiffen chromatin, but additional factors, such as histone dynamics or condensin regulation, are needed to precisely recapitulate chromatin dynamics.

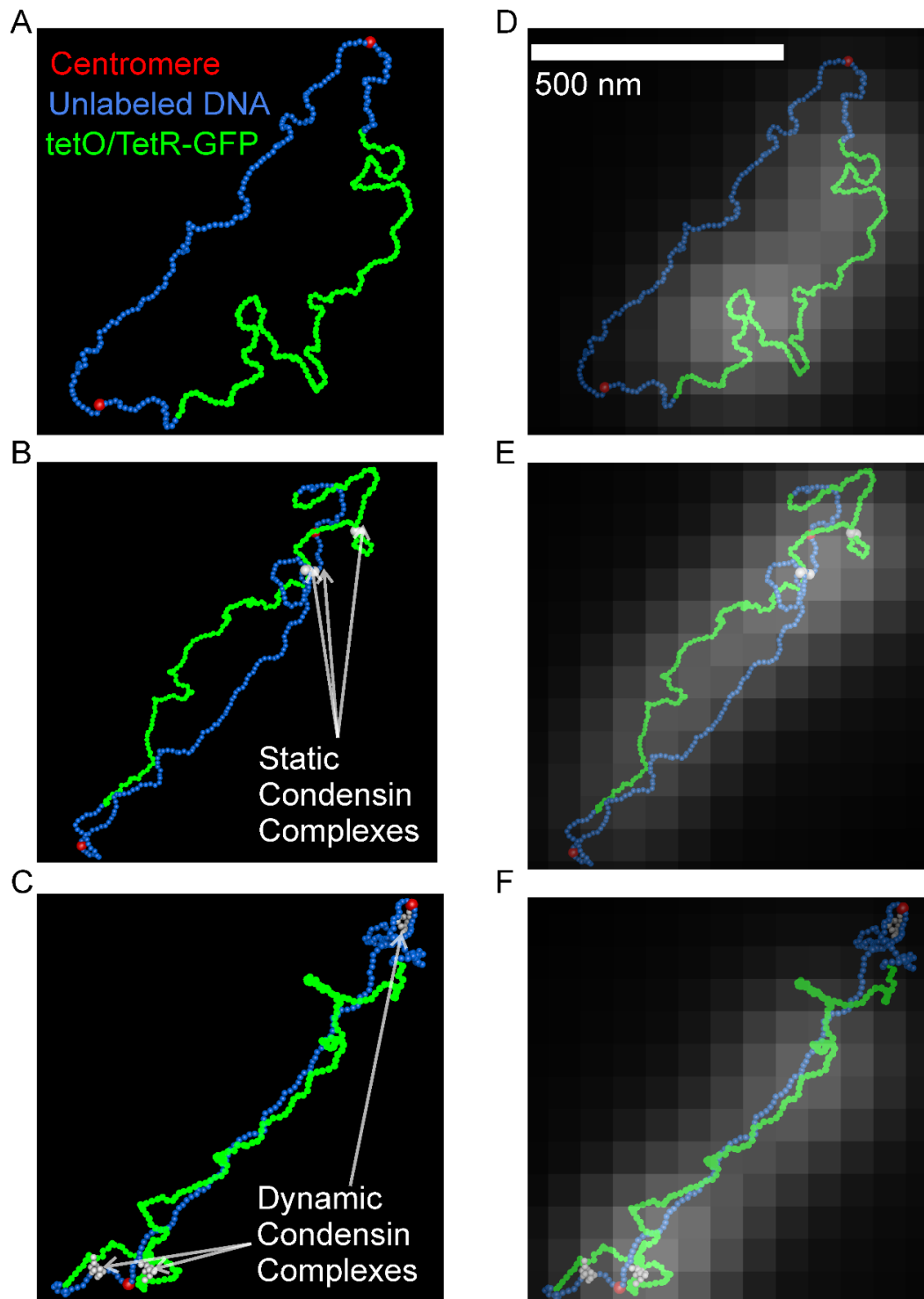


Figure 4.5 Dicentric plasmid models and simulated fluorescent images

Images of simulated dicentric plasmids without condensin (A), with static condensin (white beads) (B), and dynamic condensin (C). (E-F) Dicentric plasmid models overlaid with simulated fluorescent images. Scale bar is 500 nm

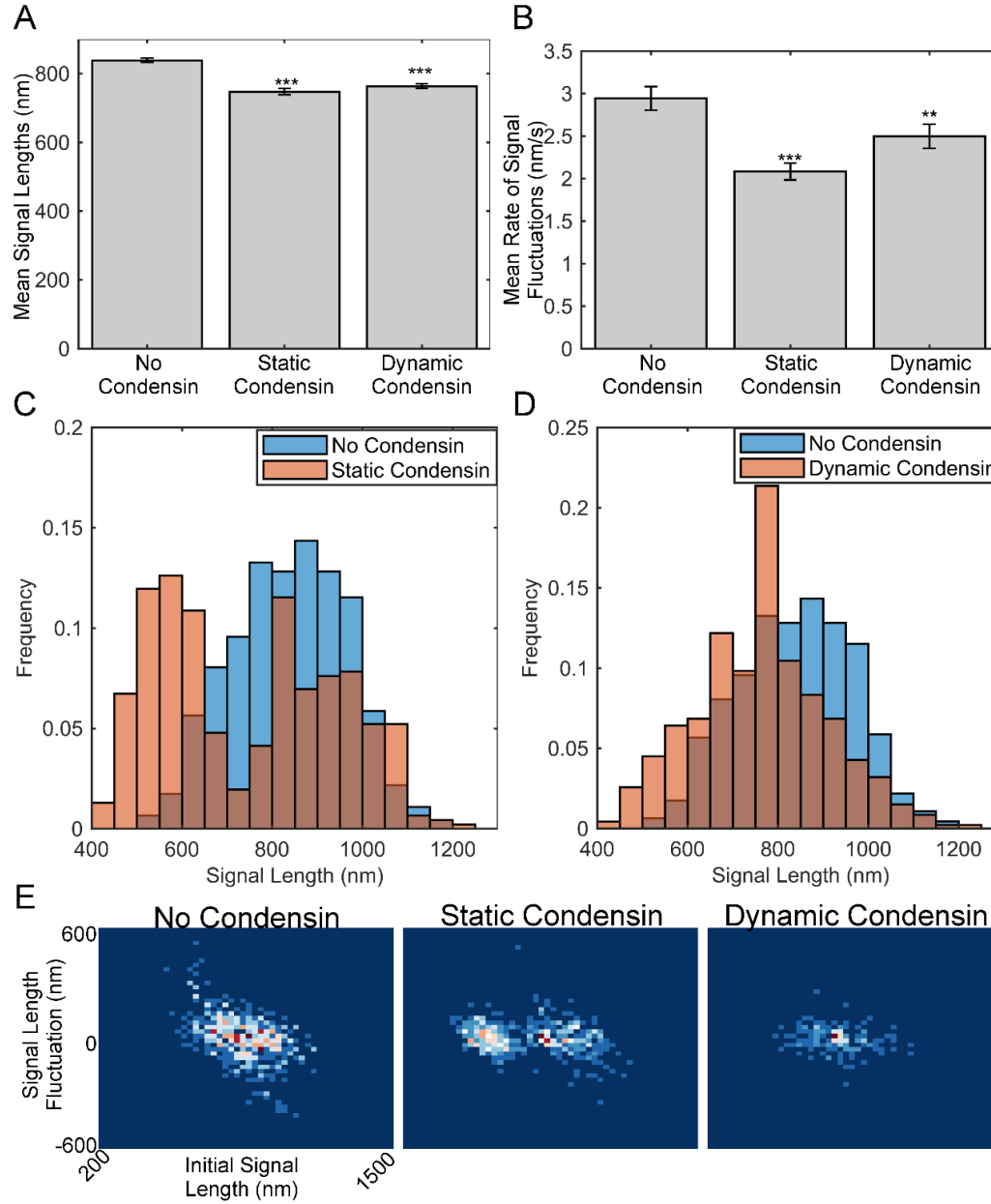


Figure 4.6 – Static and dynamic loop extrusion compact and stiffen simulated dicentric plasmids

(A) Bar charts of mean simulated signal length. Each simulation type was repeated 10 times using different random seeds. No condensin $n=460$, static condensin $n=460$, dynamic condensin $n=468$ simulated plasmid signals. Wilcoxon rank-sum test (two-sided) p -values: none vs static = 1×10^{-13} , none vs dynamic = 1×10^{-16} . (B) Bar charts of mean rate of simulated signal fluctuations. No condensin $n=310$, static condensin $n=293$, dynamic condensin $n=313$ extension/compaction events. Wilcoxon rank-sum test (two-sided) p -values: none vs static = 9×10^{-11} , none vs dynamic = 0.002. Error bars are SEM. Bonferroni correction applied to simulation comparisons such that NS, $p \geq 0.025$. *, $p < 0.025$. **, $p < 0.005$. ***, $p < 0.0005$. Histogram of simulated tetO/TetR-GFP signal length distributions comparing simulations lacking cohesin with simulations with static condensin loops (C) and dynamics condensin loops (D). (E) Density maps of change in simulated signal length as a function of initial simulated signal length.

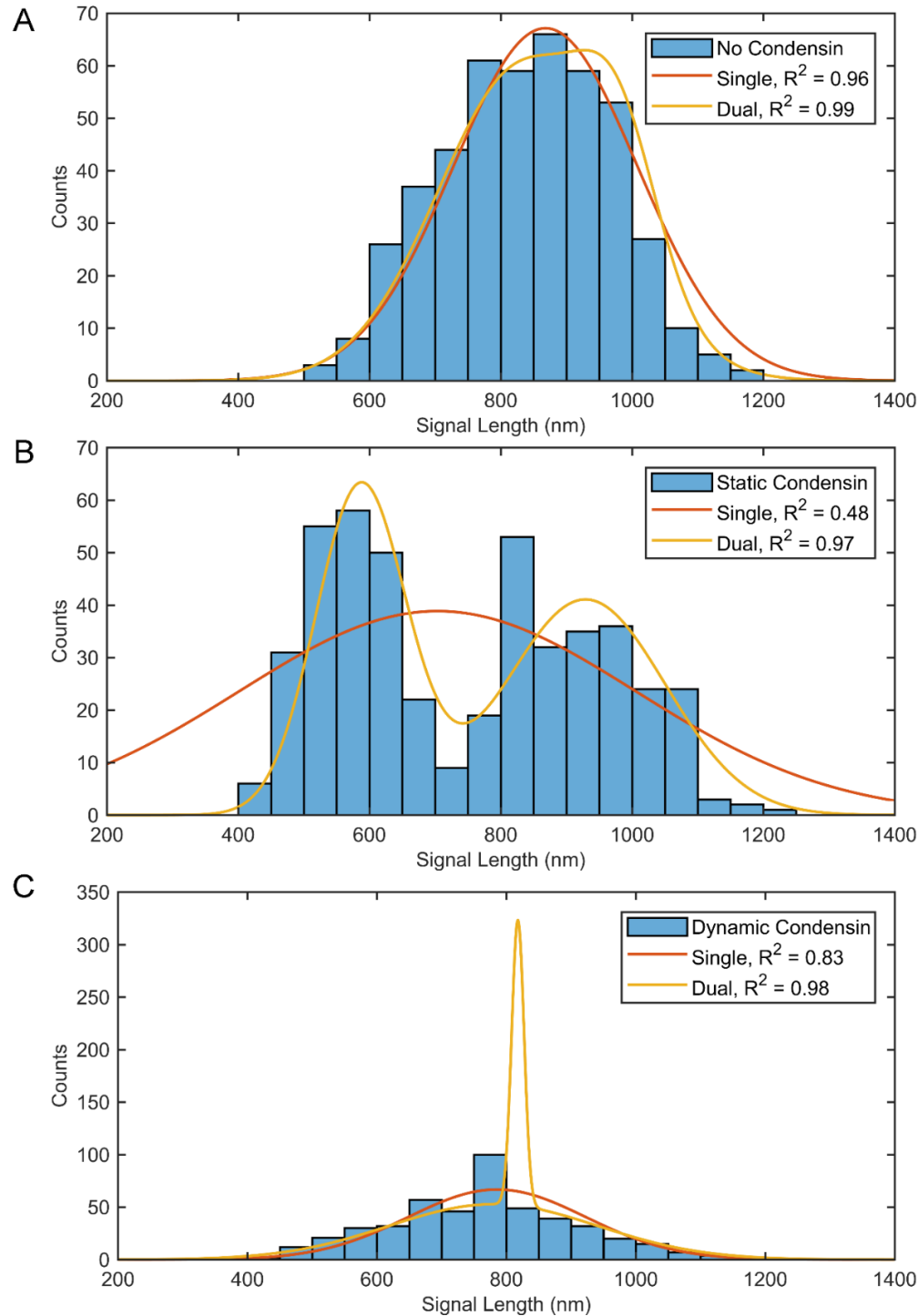


Figure 4.7 – Static and dynamic chromatin loops create subpopulations in the signal lengths of simulated dicentric plasmids

Histograms of the simulated signal lengths of the tetO/TetR-GFP array from dicentric plasmid simulations without condensin (A), with static condensin-mediated loops (B) and dynamic condensin-mediated loops (C). Histograms were fit with single-term and two-term Gaussian distributions. The goodness of fit is reported as R^2 values.

Condensin mutants display decreased heterogeneity and increased turnover

To determine if the reduced resistivity of pericentric chromatin to deformation in cells with the *brn1-9* mutation is due to increased condensin turnover on pericentric chromatin, we performed fluorescence recovery after photobleaching (FRAP) to quantify the dynamics of SMC4-GFP, a condensin subunit, in WT and *brn1-9* yeast strains within the pericentric region. At permissive temperature, 24°C, the SMC4-GFP signal was more homogenous in the *brn1-9* cells (Figure 4.8 A and B). Pericentric SMC4-GFP exhibited greater signal recovery in the *brn1-9* cells than in WT cells, $17 \pm 3\%$ vs $5\% \pm 1\%$ (mean percent recovery \pm SEM, T-test $P=9 \times 10^{-6}$) respectively (Figure 4.8 C and D). Using the mean normalized recovery curves, we calculated a half-life for SMC4-GFP of 3.3 seconds and 7.7 seconds for *brn1-9* and WT cells, respectively. Thus, the *brn1-9* allele disrupts condensin's pericentric enrichment and increases condensin's mobility within the nucleus, suggesting that the altered chromatin dynamics in the *brn1-9* mutant strains are due more rapid turnover of condensin complexes on chromatin.

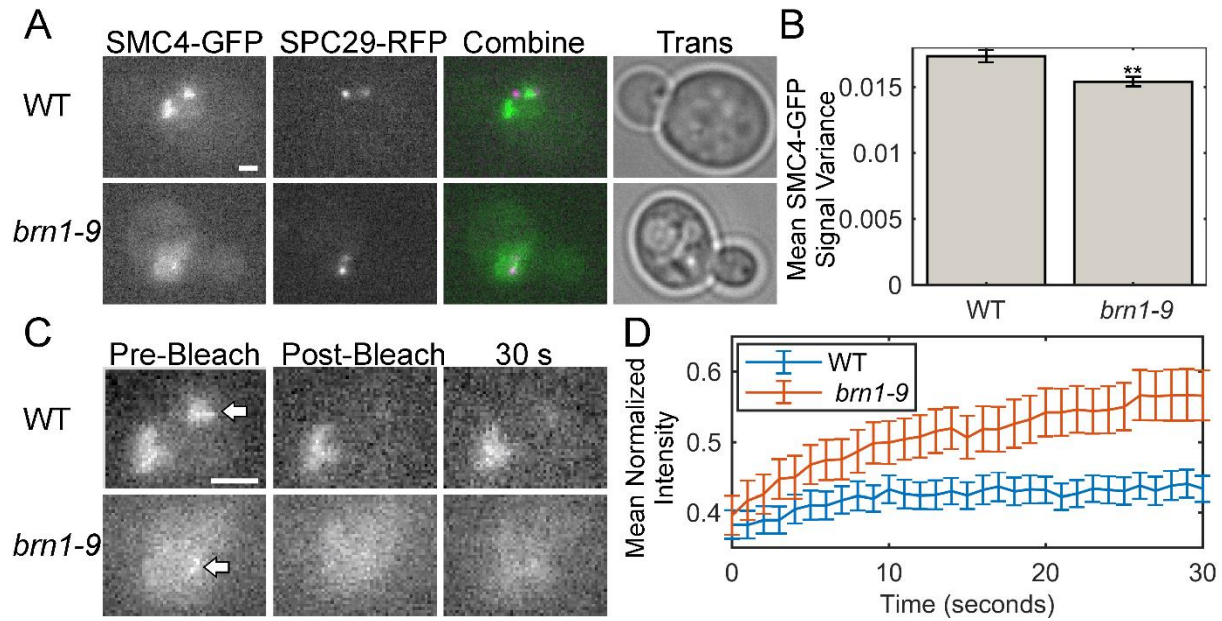


Figure 4.8 – Temperature sensitive allele, *brn1-9*, reduces enrichment and increases turnover of pericentric SMC4-GFP

(A) Representative images (in-focus planes) of labeled condensin subunit, SMC4-GFP (green), and SPB protein, SPC29-RFP (magenta) in budding yeast during metaphase. Scale bar is 1 μ m. (B) Bar charts of mean GFP signal variance in WT cells versus *brn1-9* cells. WT vs *brn1-9* Student's T-test $p = 0.002$. WT $n = 58$, *brn1-9* $n = 56$ cells. Wilcoxon rank-sum test (two-sided) p -values: WT vs *brn1-9* = 0.004. (C) Pre-bleach, post-bleach, and 30 s post bleach images of cells shown in A. Images are enlarged compared to A. White arrows indicate the bleached region centered on the pericentric region between the spindle pole bodies. Scale bar is 1 μ m. (D) Mean normalized intensity recovery curve for pericentric SMC4-GFP. WT $n = 51$, *brn1-9* $n = 38$ timelapses. All error bars are SEM.

Pericentric chromatin simulations reveal condensin-mediated chromatin loops drive condensin to axis upon chromatin extension

To determine how chromatin loops effect the entropic dynamics and organization of pericentric chromatin, we generated pericentromere models that lacked attachment to the mitotic spindle using the polymer simulator ChromoShake (Lawrimore et al., 2016). The loops are formed by condensin, which is modeled as a linear spring connecting non-consecutive DNA beads (white, Figure 4.9 A) on the same DNA strand to form static loops of 73 beads (~10 kb). Cohesin (purple beads, Figure 4.9 A) is modeled as a ring of 16 beads, encircling disparate DNA strands (pink, Figure 4.9 A). Cohesin is free to diffuse along the DNA. Condensin is bound to specific DNA beads at the axial base of the radial chromatin loops (white beads, Figure 4.9 A). Each simulation ran for over 0.05 seconds of simulated time. Assuming a nuclear viscosity of 141 poise (Fisher et al., 2009), the simulations equilibrated for at least 11.75 minutes of real time. After equilibration the centromeres of the pericentromere simulations were attached to simulated kinetochore microtubules (green, Figure 4.9 A) forcing the sister centromeres apart by 800 nm. While pericentromere simulations were not pinned to microtubules, the DNA rapidly compacted along the spindle axis (Y-axis in Figure 4.9 A, top panels vs middle panels) and condensin binding sites expanded radially (X-axis in Figure 4.9 A, top panels vs middle panels). To quantify the expansion of axial chromatin, we calculated the radius of gyration, a metric representing the volume of a distribution of beads (see Materials and Methods), of the condensin binding sites (white) over simulation time (Figure 4.9 B). Simulations lacking either condensin or cohesin exhibited a more rapid increase in the radius of gyration of their condensin binding sites (Figure 4.9 B), demonstrating axial chromatin was able to expand more rapidly in the absence of either condensin or cohesin. The faster motion of the condensin binding sites in simulations lacking condensin or cohesin recapitulates the increased fluctuation rates of the dicentric plasmid signal (Figure 4.3 F) and of the sister foci (Figure 4.1 E) in cells with disrupted condensin or depleted cohesin. Loss of both condensin and cohesin resulted in a more rapid increase in the radius of gyration of condensin binding sites than either loss condensin or cohesin alone (Figure 4.9 B), suggesting that condensin and cohesin act independently. Thus, an increase in DNA tethers, regardless of whether they are intra-strand or inter-strand, increases the amount of time necessary for DNA to fluctuate to an equilibrium position.

To determine whether the condensin-rich axial core of the pericentromere is capable of being reformed after biorientation, we returned the centromeres (the leftmost and rightmost DNA beads of the simulation) back to their initial positions by attaching them to simulated kinetochore microtubule ends (green beads). Unattached pericentromere simulations show condensin binding sites (white) and cohesin (blue) are intermingled (Figure 4.9 A, middle panel). Upon spindle attachment, condensin binding sites (white, Figure 4.9 A) rapidly returned to their initial, axial position if condensin was able to form loops in the simulation (Figure 4.9 B), regardless if cohesin was present (Figure 4.9 A and B) or absent (Figure 4.9 B, Figure 4.10 A). Thus, the pericentric organization resulting in axial condensin and radial cohesin is robust upon biorientation if condensin-mediated chromatin loops are present.

The dramatic change in the localization of condensin binding sites upon simulated biorientation (Figure 4.9 A, white beads, middle vs bottom panels) prompted us to determine how condensin-mediated loops influence the inward force generated by the entropic fluctuations of DNA in bioriented pericentromere simulations. We allowed the simulations to equilibrate for 0.05 seconds of simulated time before calculating the mean inward pulling force generated by each sister centromere pair (see Materials and Methods). We found the simulation with condensin and cohesin had a mean inward force of 1.24 ± 0.0026 pN, the simulation without condensin but with cohesin had a mean inward force of 0.0097 ± 0.0018 pN, an 84-fold decrease (Figure 4.9 C, $P=4 \times 10^{-57}$). The simulation with condensin but without cohesin had a mean inward force of 1.21 ± 0.0037 , statistically lower than the simulation with condensin and cohesin (Figure 4.9 C, $P=4 \times 10^{-6}$). The simulation with neither condensin nor cohesin had a mean inward force of 0.0055 ± 0.00015 , 225-fold less (Figure 4.9 C, $P=1 \times 10^{-57}$) than the simulation with condensin and cohesin. Thus, condensin-mediated loops greatly amplify the inward force on centromeres from the entropic fluctuations of the chromatin, while cohesin's inter-strand tethering contributes less to the inward force on centromeres. The result that condensin-mediated loops greatly increases the inward force of the pericentric chromatin provides mechanistic insight into how condensin compacts axial chromatin during mitosis (Figure 4.2 D and Figure 4.3 C).

ChromoShake simulations of the pericentric chromatin contain a precise record of each bead's location over time. This dataset allows us to calculate the mean tension on each bead in the simulation, enabling us to visualize how tension is distributed across the entire pericentric region in simulations with

microtubule attachment. We measured the mean separation of each bead to its two adjacent beads (end beads were not measured) after the simulations reached equilibrium (0.05 seconds of simulated time). In simulations with condensin, tension was isolated to the axial DNA beads independent of the presence of cohesin (Figure 4.9 D). In simulations without condensin, tension was amplified in the cohesin rings (Figure 4.9 D). In the simulation with neither condensin nor cohesin, tension was distributed evenly along the DNA (Figure 4.9 D). We generated a centromere model with condensin and cohesin but allowed beads to exist in the same location simultaneously, eliminating crowding effects and cohesin function. Eliminating collisions resulted in a small but significant decrease in inward force, 1.19 ± 0.0027 pN compared to the simulation with condensin and cohesin (Figure 4.10, $P = 9 \times 10^{-13}$) and compared to the simulation with condensin but without cohesin (Figure 4.10 B, $P = 2 \times 10^{-4}$), but had no effect on the localization of tension to axial DNA (Figure 4.10 C). Therefore, a major consequence of condensin-mediated chromatin loops is the isolation of tension to axial chromatin. These simulations demonstrate that extensional force from biorientation act disproportionately on condensin-bound DNA, forcing it to the axial core of the pericentric region. This forced axial localization of condensin directly leads to the spatial partitioning of cohesin and condensin in the pericentric region of budding yeast.

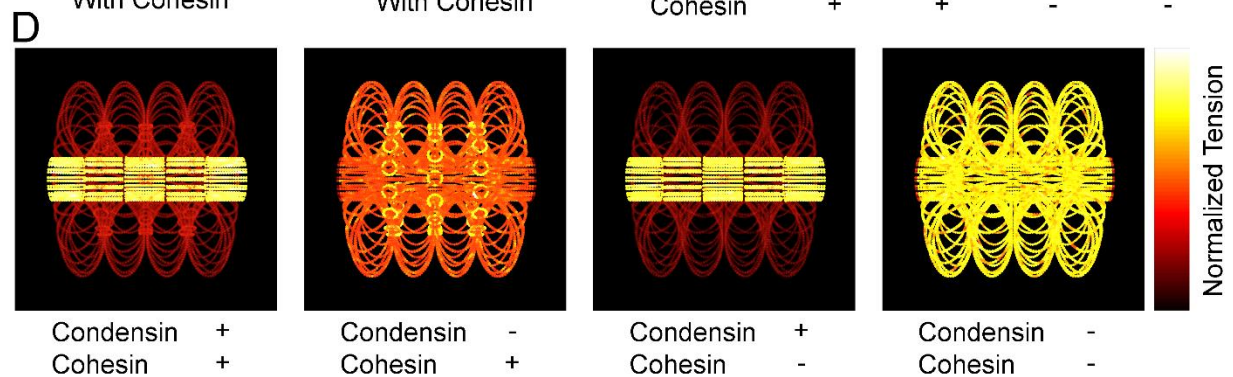
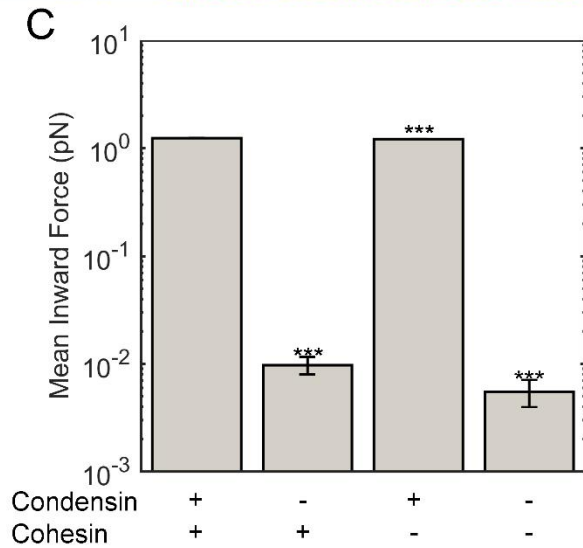
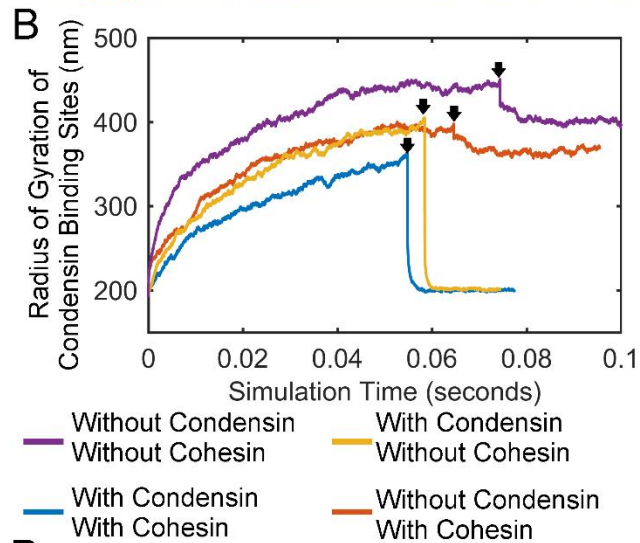
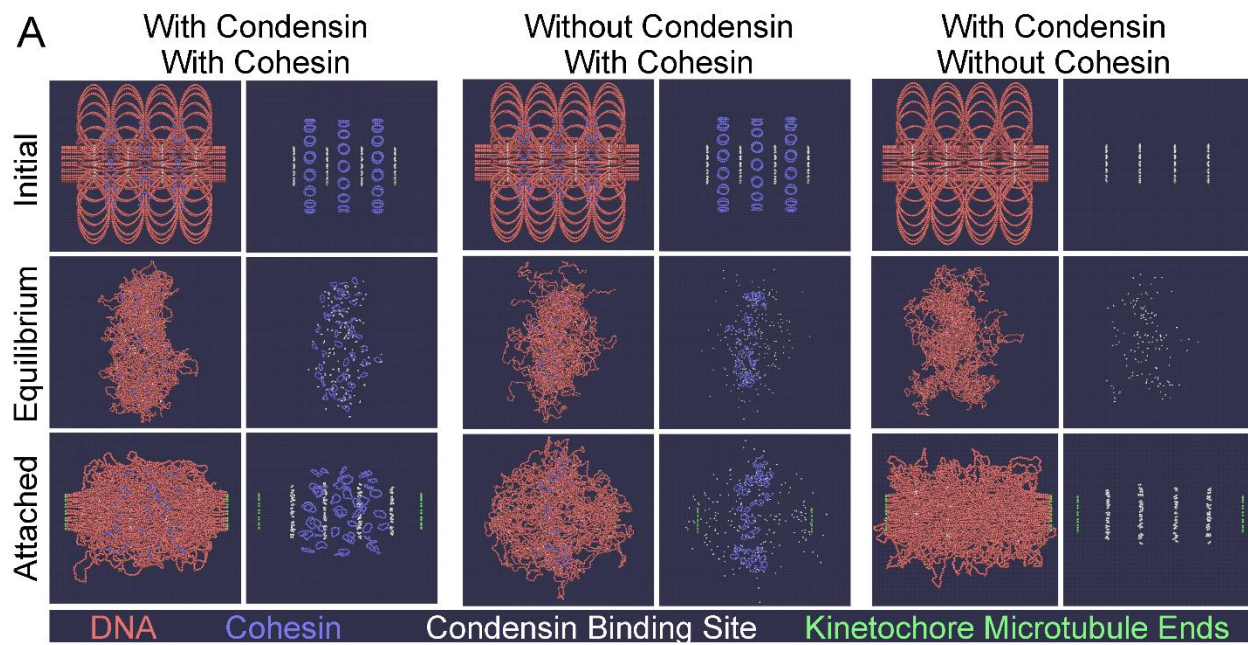


Figure 4.9 – Condensin creates two force regimes in chromatin

(A) ChromoShake simulations of pericentromeres with or without cohesin and condensin. Initial configurations are in upper panel. Centromeres, the leftmost and rightmost beads, are separated by 800 nm. Middle panels correspond to timepoints indicated by black arrows in B. Lower panels correspond to final timepoints in B. Each panel is also shown without DNA for clarity. Condensin binding sites are in white and are shown in each panel. (B) Line plots of radius of gyration of condensin binding sites over simulation time. Black arrows indicate timepoints before attachment to kinetochore microtubules is introduced. (C) Bar chart of mean inward force in pericentromere simulations with permanent attachment to kinetochore microtubules with or without cohesin and/or condensin. All simulations contained $n=16$ sister centromere pairs. Wilcoxon rank-sum test (two-sided) p-values as compared to simulation with condensin and with cohesin: without condensin and with cohesin = 2×10^{-6} , with condensin and without cohesin = 5×10^{-5} , without condensin and without cohesin = 2×10^{-6} . Error bars are SEM. (D) Initial configurations of pericentromere simulations with permanent attachment to kinetochore microtubules where DNA beads are colored based on the mean tension on that bead after the simulation has run for 0.05 s of simulation time. The bead with the most tension in each simulation white, while the bead with the lowest tension is black. The leftmost and rightmost beads are not shown.

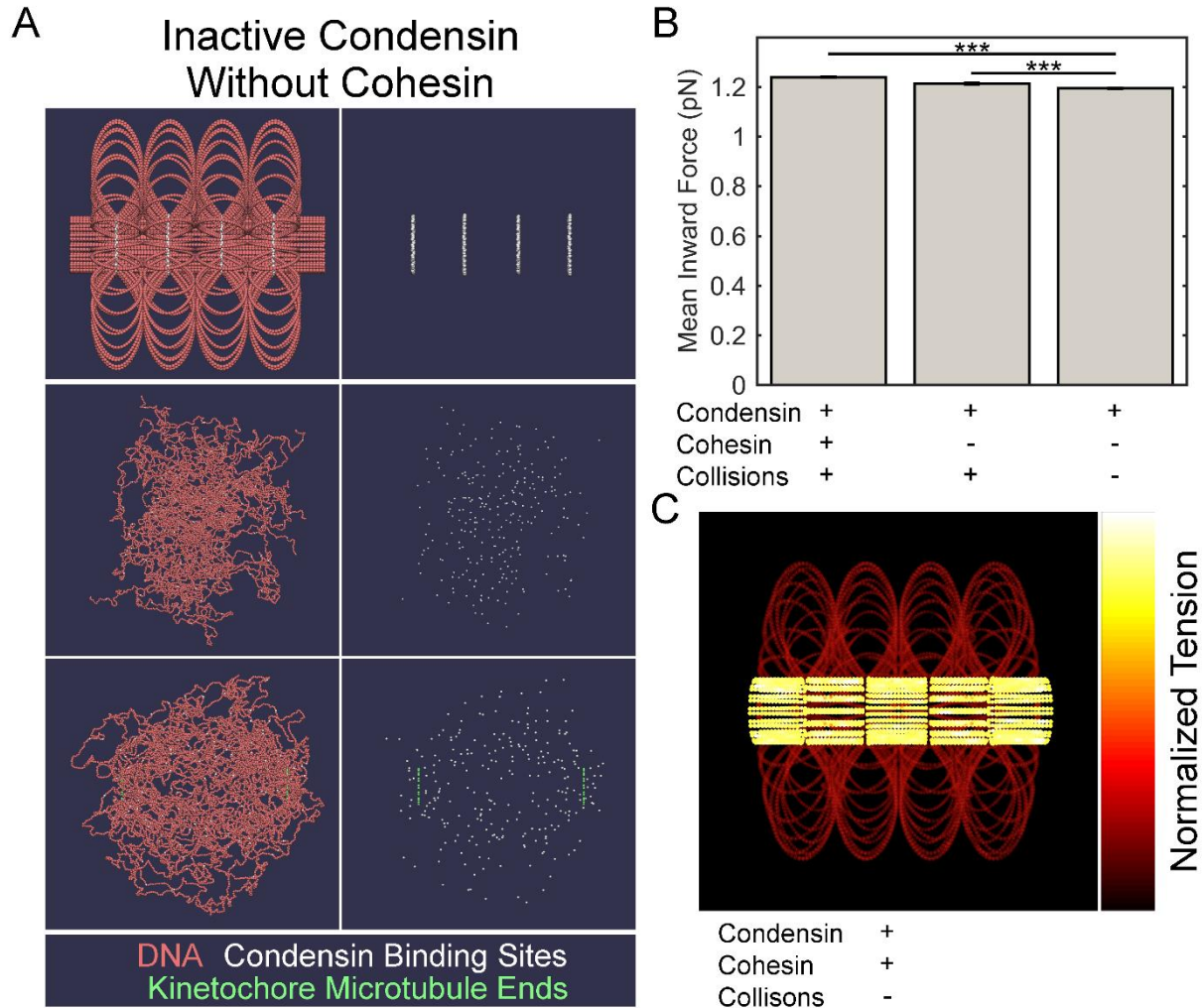


Figure 4.10 – Visualization of simulations with neither condensin nor cohesin, and collisions are not necessary to amplify and isolate tension

(A) ChromoShake simulation of pericentromere with neither cohesin nor condensin. Initial configuration is in upper panels. Centromeres, the leftmost and rightmost beads, are separated by 800 nm. Middle panels correspond to timepoints indicated by black arrows in Figure 4.5 B. Lower panels correspond to final timepoints in Figure 4.5 B. Each panel is also shown without DNA for clarity. Condensin binding sites are in white and are in each panel. (B) Bar chart of mean inward force in pericentromere simulations with permanent attachment to kinetochore microtubules. Cohesin function is dependent on collisions in simulation. All simulations contained $n=16$ sister centromere pairs. Wilcoxon rank-sum test (two-sided) p-values: with cohesin and with collisions vs without cohesin and without collisions = 2×10^{-6} , without cohesin and with collisions vs without cohesin and without collisions = 4×10^{-4} . Error bars are SEM. (C) Initial configuration of pericentromere simulation with permanent attachment to kinetochore microtubules where DNA beads are colored based on the mean tension on each bead after the simulation has run for 0.05 s of simulation time. The simulation contains cohesin and condensin, but lacks collisions, eliminating any effects from molecular crowding. The bead with the most tension in each simulation white, while the bead with the lowest tension is black. The leftmost and rightmost beads are not shown.

Discussion

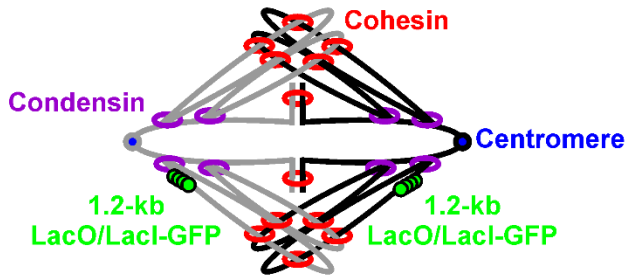
During metaphase, chromosome biorientation separates sister centromeres 800-1000 nm. That distance of sister centromere separation in mitosis is conserved across a range of eukaryotic organisms (Bloom, 2014). In budding yeast, the two classes of SMC complexes, condensin and cohesin, occupy non-overlapping domains within the pericentric region (Stephens et al., 2011). Since both cohesin and condensin are both loaded at centromeres (Uhlmann, 2016), what properties of these ring complexes cause their disparate geometric localizations? Our simulations illustrate that intra-strand tether points, i.e. condensin, are driven to the axial core of DNA substrate in the presence of an extensional force mimicking chromosome biorientation (Figure 4.9 A). Slip-link tethers, i.e. cohesin, diffuse to the radial periphery of the DNA substrate regardless of the presence of an extensional force on the DNA substrate (Figure 4.9 A). Live-cell imaging and FRAP of condensin subunit SMC4-GFP showed that condensin enrichment is lost when condensin turnover increases (Figure 4.8). Thus, a *brn1-9* mutant condensin complex, which cannot act as an intra-strand tether point, does not localize to the axial core of the pericentric region. This result is predicted by the simulations lacking condensin, as condensin-bound DNA remains dispersed even upon attachment of chromatin to the spindle (Figure 4.9 A). The presence of either inter-strand or intra-strand tethers caused simulations of pericentric DNA to fluctuate to their equilibrium positions more slowly (Figure 4.9 B), recapitulating our experimental results that both cohesin and condensin appear to slow changes in the distances between sister foci (Figure 4.1 E) and dicentric plasmid signal length (Figure 4.3 F). Condensin confers resistivity to deformation by forming chromatin loops, while cohesin makes chromatin functions by loosely tethering chromatin loops together (Figure 4.11) The presence of the tethers increases the apparent viscosity of the pericentric chromatin, making the entire pericentric region more resistive to deformation from outside forces. In other words, condensin and cohesin transform the pericentromere into an amalgamated, gelatinous substrate. Extension of this substrate results in amplified tension in its axial core. Under tension, this substrate has a robust organization with condensin at its axial core and cohesin at its radial periphery.

Geometric partitioning of cohesin and condensin in pericentric chromatin requires the presence of an extensional force. In the pericentric region this force is provided by the mitotic spindle. However, in higher eukaryotes this extensional force can be provided by a sufficient density chromatin loops. Bottle-

brush polymers, a highly branched polymer with many sidechains emanating from a single polymer backbone, have high axial tension due to steric repulsion of the sidechains extending the polymer backbone. The magnitude of axial tension is dependent on the density and length of the sidechains (Rubinstein and Colby, 2003; Panyukov et al., 2009a; Panyukov et al., 2009b; Lebedeva et al., 2012). In chromosomes, the condensin rich chromosome axis acts as the polymer backbone and the loops act as the sidechains. Polymer simulations of a 30 Mb chromosome show that condensin-mediated chromatin loop extrusion can convert an isotropic sphere of chromatin into an anisotropic chromosome due to the extensional force from steric repulsion between loops (Goloborodko et al., 2016). Our work predicts that loop repulsion drives the axial localization of condensins in chromosomes of higher eukaryotes (Hirano, 2016). Condensin's persistent binding to chromatin loops entropically drives its axial localization if a sufficiently large extensional force is present in the chromatin. Therefore, the localization of condensin is influenced by condensin's ability to form chromatin loops. The greater the concentration of condensin, the higher the chromatin loop density, and the greater the extensional force that concentrates condensin to the axial core of chromosomes.

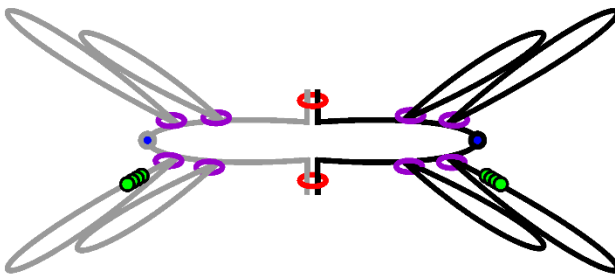
A

Wildtype
With Cohesin, With Condensin



B

mcm21Δ
Depleted Cohesin, With Condensin



C

brn1-9
With Cohesin, Disrupted Condensin

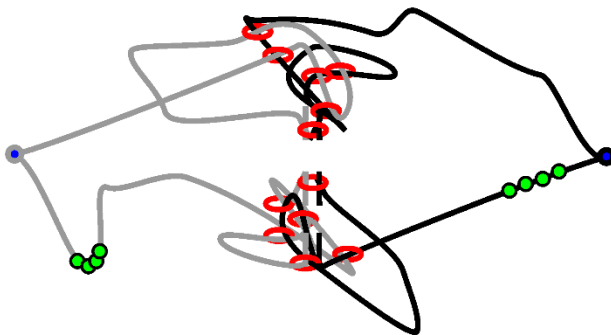


Figure 4.11 – Models of WT, *mcm21Δ*, and *brn1-9* pericentric regions

Models of the pericentric region during metaphase (sister strands are gray and black) labeled with the 1.2-kb lacO/LacI-GFP array (green) centered 1.7 kb from the centromere (blue) with either both cohesin (red) and condensin (purple) (A), depleted cohesin (B), or disrupted condensin (C).

Materials and Methods

Strain growth and imaging preparation

Detailed strain genotypes are in table 4.1. Strain JLY1043-1 had *mcm21* removed using primers AAAGAAAAGAGCTAAGCTGGAGAATGAGGAAATTTTACCAGAACAAGAATGGGTTTTAAAGACCCAG CCACAGCTGAAGCTTCGTACGC and ATCTATGATAAACAGAGAGAAAATTAGCTCTATCCTCTTTCTATAAAGTATATTTTTGTAAACATGCATAGG CCACTAGTGGATCTG to PCR a KAN marker from plasmid pFA6a-kanMX6. Bold portions of sequence have homology to pFA6a-kanMX6 plasmid. Transformants were screened by PCR fragment size with primers CAGTAATGGCCGACCAATTCTATGATAGATCTTC and GGCAATATATCCATTCTTGCTAGATAGTGGAAG. Strain JLY1071-1 had *mcm21* removed using primers GAGAGCGCTAATCCTATAGTACA and TACGAGCTTGCCCTTGCCATTGTT on a genomic DNA sample extracted from KBY9059. Transformants were screened by PCR fragment size with primers GAGAGCGCTAATCCTATAGTACA and TACGAGCTTGCCCTTGCCATTGTT. Strains JLY1062-1 and JLY1072-1 were transformed with the plasmid pSOI digested with Pvu1 and Xho1 to introduce the *brn1-9* mutation. Strains were screened for temperature sensitivity to 42° C. The dicentric plasmid was transformed into yeast and screened using GFP signal. All strains were grown in liquid media 24 °C. All biological experiments were performed using at least three different liquid yeast cultures grown on separate days. All strains were grown to mid-logarithmic phase prior to imaging. Strains with temperature sensitive mutations and their wildtype controls strains were grown at 37 °C for three hours prior to imaging. Strains, excluding strains containing the dicentric plasmid, were grown in rich YPD media. Strains with an adenine mutation were grown with 0.5 mg/mL additional adenine. Strains with the dicentric plasmid pT431 were grown in YCAT-galactose media with 0.5 mg/mL additional adenine and methionine. Four hours prior to imaging, cells with the dicentric plasmid pT431 were washed and incubated in SG (synthetic-containing galactose) media lacking methionine with 0.5 mg/mL additional adenine to induce the recombinase to excise the ARS sequence of the plasmid. Cells were then resuspended in YPD for 20 minutes to repress transcription from the GAL1 promoter and activate the second, conditional centromere (Dewar et al., 2004). Cells were then washed and resuspended in YC complete media with 2% filter sterile glucose. Prior to imaging, cells with Smc4-GFP were washed and

resuspended with YC complete media lacking sugar. Prior to imaging, cells with the 10-kb lacO/LacI-GFP array were washed and then incubated for 20 minutes with YC complete media with 0.02% sodium azide and 1 μ M deoxy-glucose. Prior to imaging, cells with the 1.2-kb lacO/LacI-GFP array were washed and then resuspended in YC complete media with 2% filter sterile glucose. Strains containing the dicentric plasmid were imaged on slides with agar pads composed of 2% low melting temperature agarose and YC complete media with 2% filter sterile glucose. All other strains were imaged on untreated glass coverslips.

Table 4.1 – Strain genotypes

Strain Name	Relevant Genotype
KBY9035-2	(YEF 473A) Smc4-GFP:Kan, Spc29-RFP:Hyg
YYY1003-1	(YEF 473A) brn1-9:Nat, Spc29-RFP:Hyg, Smc4-GFP:Kan
KBY8065	MATa CEN15(1.8)-GFP[10kb] ade2-1, his3-11, trp1-1, ura3-1, leu2-3,112, can1-100, LacINLSGFP:HIS3, lacO::URA3, Spc29-RFP:Hyg
KBY9059-1	MATa CEN15(1.8)-GFP[10kb] ade2-1, his3-11, trp1-1, ura3-1, leu2-3,112, can1-100, LacINLSGFP:HIS3, lacO::URA3, Spc29-RFP:Hyg, mcm21Δ:Nat
KBY9039-2	MATa CEN15(1.8)-GFP[10kb] ade2-1, his3-11, trp1-1, ura3-1, leu2-3,112, can1-100, LacINLSGFP:HIS3, lacO::URA3, Spc29-RFP:Hyg, brn1-9-Nat
JLY1039-1	(W303) Mat A trp1::MET-Recombinase::TRP leu2::TetR-GFP::LEU2, Spc42-mCherry:Nat, pT431 #9
JLY1043-1	(W303) Mat A trp1::MET-Recombinase::TRP leu2::TetR-GFP::LEU2, Spc42-mCherry:Nat, mcm21Δ:Kan, pT431 #9
JLY1062-1	(W303) Mat A trp1::MET-Recombinase::TRP leu2::TetR-GFP::LEU2, Spc42-mCherry:Kan, brn1-9:Nat, pT431 #9
KBY8159-1	MATa ade1, met14, ura3-52, leu2-3,112 his3-11,15 lys2Δ::lacI-GFP-NLS-NAT, 1.1 kb CEN 3::LacOKAN (1.2-kb array), natΔ:His3
JLY1071-1	MATa ade1, met14, ura3-52, leu2-3,112 his3-11,15 lys2Δ::lacI-GFP-NLS-NAT, 1.1 kb CEN 3::LacOKAN (1.2-kb array), natΔ:His3, mcm21Δ:Nat
JLY1072-1	MATa ade1, met14, ura3-52, leu2-3,112 his3-11,15 lys2Δ::lacI-GFP-NLS-NAT, 1.1 kb CEN 3::LacOKAN (1.2-kb array), natΔ:His3, brn1-9:Nat

Microscopy

Timelapses of strains containing the 10-kb lacO/LacI-GFP array or containing the dicentric plasmid were performed at room temperature (25°C) using an Eclipse Ti wide-field inverted microscope (Nikon) with a 100x Apo TIRF 1.49 NA objective (Nikon) and Clara charge-coupled device camera (Andor) using Nikon NIS Elements imaging software (Nikon). Timelapses of strains containing the 10-kb lacO/LacI-GFP array were 10 minutes in duration with 30 second intervals. At each interval a 7-step Z-stack of 300 nm step size was acquired in the GFP, RFP and Trans channels. Timelapses of strains containing the dicentric plasmid were the same as above but with a duration of 20 minutes.

Population images of the dicentric plasmid strains and of strains containing the 1.2-kb lacO/LacI-GFP array were imaged at room temperature (25°C) using an Eclipse E600FN microscope (Nikon) with a 100x Plan Apo TIRF 1.45 NA objective (Nikon) and ImagEM EM-CCD digital camera (Hamamatsu) with a custom Lumencor LED illumination system (Lumencor Inc.) using MetaMorph 7.7 imaging software (Molecular Devices). Each acquisition was a 7-step Z-stack with a 300-nm step size in the GFP, RFP, and Trans channels.

FRAP

FRAP of strains containing SMC4-GFP was performed at room temperature (25°C) the Eclipse Ti wide-field inverted microscope (Nikon) described above. For each experiment, a single 7-step Z-stack with 300-nm step size was acquired prior to bleaching in the GFP, RFP, and Trans channels, then the laser image, then a 30 s timelapse with 1 second intervals in the same z-plane as the laser bleaching in the GFP channel only. Image analysis was carried out using a custom MATLAB GUI, FRAP_gui.m. The GUI allows the user to generate and alter binary masks of the bleached nucleus, a reference nucleus, and the bleached region. The program then generates a bleach curve for the reference region, the unbleached portion of the nucleus, and the bleached region and saves all the relevant data to a MAT data file that is parsed by an analysis program, FRAP_summary_ind_t_half.m, to generate the average bleach curves shown in Fig. 2 D and calculate the half-life and percent recovery of the curves.

Signal variance analysis

The pre-bleach image stacks of strains containing SMC4-GFP were cropped such that only nuclei remained in the image. The cropped stacks were converted into maximum intensity projections. The

intensities of the projections were then normalized by dividing each intensity value by the maximum intensity value of the projection. The background was removed by using Otsu thresholding with the MATLAB function `multithresh`. The variance of the remaining signal was calculated for each image using the MATLAB program `SMC4_GFP_variance_analysis.m`.

ChromoShake simulation and Analysis

The centromere models were generated using `chromoShake_make_spindle` C++ program to generate a configuration file. Unpinning of the models was performed by altering the drag coefficient term in the configuration file from 3.38889×10^{-15} to 3.38889×10^{-20} . Simulations were then run using the `chromoShake` simulator. Radius of gyration calculations of condensin-bound DNA beads was performed using a custom MATLAB program, `rog_specific_large_edit.m`, that parses the `chromoShake` outfiles and a list of beads to use in the calculation. Radius of gyration is a measure of the volume of the distribution of points and is defined as

$$R_g^2 \stackrel{\text{def}}{=} \frac{1}{N} \sum_{k=1}^N (r_k - \hat{r})^2 \quad (1)$$

where N is the number of beads, r_k is the position of an individual bead, and \hat{r} is the mean position of all the beads.

Calculating the mean inward force from pinned centromere simulations was performed using custom MATLAB programs, `end_to_end.m` and `inward_force.m`, to determine the mean drag force of the end beads. In pericentromere simulations, the centromeres are composed of two beads. Each of these beads has 105-fold greater drag force on each of them than all other beads in the simulation. The larger drag force effectively pins the centromeres in space to mimic attachment to the mitotic spindle. Each centromere bead has a corresponding sister centromere bead. To calculate the inward force on each centromere bead pair, the mean velocity of the sister centromere beads relative to each other was calculated after a 0.05 second equilibration time. The inward force is based on viscous drag and is calculated as

$$\vec{F} = 6\pi\eta a \vec{v} \quad (2)$$

where viscosity (η) is 0.001 PS*s, the drag radius (a) is 10 nm, and the velocity (\vec{v}) is the mean velocity of the sister centromere beads relative to each other. These calculations were performed with the `inward_force.m` program. The mean inward force per centromere (Figure 4.5 C) was calculated by

summing the inward force of each sister centromere bead and taking the mean of the resulting 16 centromere inward force measurements. The coloration of the pericentromere models based on normalized tension on each bead used a custom python script, AvgTensionTotalNorm.py, run by Blender. This program colored each bead in the simulation based on the mean bead-bead separation of each bead with its two neighbors across time. The mean bead-bead separations were normalized by dividing each bead-bead separation by the maximum bead-bead separation of that simulation. The inward force and tension visualization analyses were applied to the centromere simulations from Lawrimore et al. (2016).

The initial dicentric plasmid model was created using the chromoShake_make_chromatin_loop C++ program. The model is composed of 386 beads to mimic the size of the plasmid after the ARS sequence is looped out, approximately 11 kb. The centromeres of the plasmid were physically pinned 800 nm apart by altering the positions of the centromere beads in the configuration file and running the model for 0.18 seconds at a timestep of 0.9 ns using the chromoShake simulator. The color section was altered to match the size and position of the tetO array. Ten simulations of this dicentric plasmid model were run with different random seeds. Static condensin was added to the dicentric plasmid model by using Excel's (Microsoft) RANDBETWEEN function to generate three random bead pairs within the plasmid and adding three springs pairing the beads to the dicentric plasmid outfile. The springs were given the default rest length (10 nm) and spring constant (~ 0.23 N/m). Ten versions of the static dynamic simulations were creating using different spring locations. Each static condensin simulation was run using the chromoShake simulator. Three dynamic condensins were added to the dicentric plasmid model using the MATLAB program add_condensin.m. Ten version of the dynamic simulations were creating using different random seeds to generate different starting positions for the dynamic condensin complexes. Simulated images of the tetO array were created using Microscope Simulator 2 (Quammen et al., 2008). The simulated images were analyzed using a custom MATLAB program that automatically converted the simulated images into binary masks and used the REGIONPROPS function in MATLAB to measure the signal lengths. Simulated density maps of dicentric plasmids (Figure 4.6 E) were generated using the data from the REGIONPROPS analysis using the MATLAB program sim_plasmid_heatmap_summary.m which uses the same plasmid_heatmap function used to generate the experimental density maps (Figure

4.3 H) using MATLAB's HeatMap function. The mean simulated plasmid signal length and mean rate of change in signal length were calculated using the MATLAB programs `sim_plasmid_rate_analysis.m` and `simulated_plasmid_barcharts.m`.

Motion tracking and analysis

Timelapses of the 10-kb *lacO/LacI*-GFP arrays were analyzed using Speckle Tracker (Wan et al., 2009) and an automated version of Speckle Tracker called Auto Track. Both programs fit a 2D gaussian to each GFP signal (5x5 pixel region) to generate a sub-pixel position in X and Y using the MATLAB function `LSQCURVEFIT`. The mean position of the sister GFP foci was calculated as a fiducial point for the motion of the GFP foci as described in Chacon et al. (2014). After subtracting the fiducial point from the foci, the foci positions over time are used to calculate the mean squared displacement curves and the radii of confinement using the MATLAB program `midpoint_motion.m`. The radius of confinement was calculated using the equation

$$R_c = \frac{5}{4} \times \sqrt{(2\sigma^2 + \Delta r_0^2)} \quad (3)$$

where σ^2 is mean of the variance of the foci position in X and Y, and Δr_0^2 is the mean squared deviation from the mean position calculated by

$$\Delta r_0^2 = \Delta x_0^2 + \Delta y_0^2 \quad (4)$$

where Δx_0^2 is the mean squared deviation from the mean position in the x-dimension and Δy_0^2 is the mean squared deviation from the mean position in the y-dimension. Each timelapse represents a biological replicate.

The mean rate of sister foci fluctuations was calculated using the MATLAB program `sister_rate_analysis.m`. The program identified persistent motion events, sister foci coming toward/away from each other, in the timelapses. The rate of the fluctuation was calculated by dividing the total displacement of the event by the duration of the event. Each event was treated as a random sample and all the events for each treatment group or strain was pooled to determine the mean rate of sister foci fluctuation.

Dicentric plasmid image analysis

Both timelapse and population images of strains containing dicentric plasmids were analyzed using a custom MATLAB GUI, `population_GUI_v1_2.m`. The GUI allows users to select plasmid signals in

the GFP channel, select a background region in the GFP channel for background subtraction, generate and alter a binary mask based on background subtraction of plasmid signal, and select spindle pole bodies in the RFP channel. Only cells containing a single plasmid signal were analyzed. The data for each plasmid signal was saved in a .MAT file for summary analysis of plasmid signal length, plasmid stretching (aspect ratio greater than or equal to 1.5), plasmid signal length changes over time, and spindle length by various MATLAB programs. Density maps of plasmid dynamics were constructed using the MATLAB program `plasmid_heatmap.m` that utilizes MATLAB's HeatMap function.

Population image analysis of 1.2-kb lacO/LacI-GFP array

Population images of strains containing the 1.2-kb lacO/LacI-GFP array were analyzed using the MATLAB GUI, `heatmap_GUI.m` which allows the user to measure the positions (brightest pixel) and the stretched state (determined by user) of the array signals and the positions (brightest pixel) of the spindle pole bodies. Various summary MATLAB programs were used to measure the mean separation of the sister arrays and the mean stretch frequency of the arrays from the .MAT files generated by the `heatmap_GUI.m` program. For mean sister foci separation each cell was considered a biological replicate. For the mean stretch frequency each image session, containing multiple cells, was considered a technical replicate.

Statistical analysis

Unless otherwise noted in the figure legends markers of statistical significance in the figure legends are NS, $p \geq 0.05$. *, $p < 0.05$. **, $p < 0.01$. ***, $p < 0.001$. The non-parametric Wilcoxon rank-sum test, MATLAB function `ranksum`, was used for all statistical comparisons. We chose a minimum sample size of 34 assuming 0.9 power and a large effect size (Cohen, 1988).

The histograms of experimental and simulated plasmid signal lengths were generated using MATLAB's histogram function. The Gaussian fits and the goodness-of-fit statistics were calculated using MATLAB's fit function on a plot of the histograms' bin edges, excluding the first bin edge, and the bin counts.

REFERENCES

- Bloom, K.S. 2014. Centromeric Heterochromatin: The Primordial Segregation Machine. *Annu Rev Genet.*
- Chacon, J.M., S. Mukherjee, B.M. Schuster, D.J. Clarke, and M.K. Gardner. 2014. Pericentromere tension is self-regulated by spindle structure in metaphase. *J Cell Biol.* 205:313-324.
- Cohen, J. 1988. Statistical power analysis for the behavioral sciences. L. Erlbaum Associates, Hillsdale, N.J. xxi, 567 p. pp.
- D'Ambrosio, C., C.K. Schmidt, Y. Katou, G. Kelly, T. Itoh, K. Shirahige, and F. Uhlmann. 2008. Identification of cis-acting sites for condensin loading onto budding yeast chromosomes. *Genes Dev.* 22:2215-2227.
- Dewar, H., K. Tanaka, K. Nasmyth, and T.U. Tanaka. 2004. Tension between two kinetochores suffices for their bi-orientation on the mitotic spindle. *Nature.* 428:93-97.
- Eckert, C.A., D.J. Gravidahl, and P.C. Megee. 2007. The enhancement of pericentromeric cohesin association by conserved kinetochore components promotes high-fidelity chromosome segregation and is sensitive to microtubule-based tension. *Genes Dev.* 21:278-291.
- Fisher, J.K., M. Ballenger, E.T. O'Brien, J. Haase, R. Superfine, and K. Bloom. 2009. DNA relaxation dynamics as a probe for the intracellular environment. *Proc Natl Acad Sci U S A.* 106:9250-9255.
- Ganji, M., I.A. Shaltiel, S. Bisht, E. Kim, A. Kalichava, C.H. Haering, and C. Dekker. 2018. Real-time imaging of DNA loop extrusion by condensin. *Science.* 360:102-105.
- Gibcus, J.H., K. Samejima, A. Goloborodko, I. Samejima, N. Naumova, J. Nuebler, M.T. Kanemaki, L. Xie, J.R. Paulson, W.C. Earnshaw, L.A. Mirny, and J. Dekker. 2018. A pathway for mitotic chromosome formation. *Science.*
- Glynn, E.F., P.C. Megee, H.G. Yu, C. Mistrot, E. Unal, D.E. Koshland, J.L. DeRisi, and J.L. Gerton. 2004. Genome-wide mapping of the cohesin complex in the yeast *Saccharomyces cerevisiae*. *PLoS Biol.* 2:E259.
- Goloborodko, A., M.V. Imakaev, J.F. Marko, and L. Mirny. 2016. Compaction and segregation of sister chromatids via active loop extrusion. *Elife.* 5.
- Hirano, T. 2012. Condensins: universal organizers of chromosomes with diverse functions. *Genes Dev.* 26:1659-1678.
- Hirano, T. 2016. Condensin-Based Chromosome Organization from Bacteria to Vertebrates. *Cell.* 164:847-857.
- Hu, B., T. Itoh, A. Mishra, Y. Katoh, K.L. Chan, W. Upcher, C. Godlee, M.B. Roig, K. Shirahige, and K. Nasmyth. 2011. ATP hydrolysis is required for relocating cohesin from sites occupied by its Scc2/4 loading complex. *Curr Biol.* 21:12-24.
- Kinoshita, K., T.J. Kobayashi, and T. Hirano. 2015. Balancing acts of two HEAT subunits of condensin I support dynamic assembly of chromosome axes. *Dev Cell.* 33:94-106.
- Lavoie, B.D., K.M. Tuffo, S. Oh, D. Koshland, and C. Holm. 2000. Mitotic chromosome condensation requires Brn1p, the yeast homologue of Barren. *Mol Biol Cell.* 11:1293-1304.

- Lawrimore, J., J.K. Aicher, P. Hahn, A. Fulp, B. Kompa, L. Vicci, M. Falvo, R.M. Taylor, 2nd, and K. Bloom. 2016. ChromoShake: a chromosome dynamics simulator reveals that chromatin loops stiffen centromeric chromatin. *Mol Biol Cell*. 27:153-166.
- Lawrimore, J., B. Friedman, A. Doshi, and K. Bloom. 2017. RotoStep: A Chromosome Dynamics Simulator Reveals Mechanisms of Loop Extrusion. *Cold Spring Harb Symp Quant Biol*.
- Lawrimore, J., P.A. Vasquez, M.R. Falvo, R.M. Taylor, 2nd, L. Vicci, E. Yeh, M.G. Forest, and K. Bloom. 2015. DNA loops generate intracentromere tension in mitosis. *J Cell Biol*. 210:553-564.
- Lebedeva, N.V., A. Nese, F.C. Sun, K. Matyjaszewski, and S.S. Sheiko. 2012. Anti-Arrhenius cleavage of covalent bonds in bottlebrush macromolecules on substrate. *Proc Natl Acad Sci U S A*. 109:9276-9280.
- Liang, Z., D. Zickler, M. Prentiss, F.S. Chang, G. Witz, K. Maeshima, and N. Kleckner. 2015. Chromosomes Progress to Metaphase in Multiple Discrete Steps via Global Compaction/Expansion Cycles. *Cell*. 161:1124-1137.
- Losada, A., T. Yokochi, R. Kobayashi, and T. Hirano. 2000. Identification and characterization of SA/Scs3p subunits in the *Xenopus* and human cohesin complexes. *J Cell Biol*. 150:405-416.
- Megee, P.C., C. Mistrot, V. Guacci, and D. Koshland. 1999. The centromeric sister chromatid cohesion site directs Mcd1p binding to adjacent sequences. *Mol Cell*. 4:445-450.
- Naumova, N., M. Imakaev, G. Fudenberg, Y. Zhan, B.R. Lajoie, L.A. Mirny, and J. Dekker. 2013. Organization of the mitotic chromosome. *Science*. 342:948-953.
- Ng, T.M., W.G. Waples, B.D. Lavoie, and S. Biggins. 2009. Pericentromeric sister chromatid cohesion promotes kinetochore biorientation. *Mol Biol Cell*. 20:3818-3827.
- Panyukov, S., E.B. Zhulina, S.S. Sheiko, G.C. Randall, J. Brock, and M. Rubinstein. 2009a. Tension amplification in molecular brushes in solutions and on substrates. *J Phys Chem B*. 113:3750-3768.
- Panyukov, S.V., S.S. Sheiko, and M. Rubinstein. 2009b. Amplification of tension in branched macromolecules. *Phys Rev Lett*. 102:148301.
- Pearson, C.G., P.S. Maddox, T.R. Zarzar, E.D. Salmon, and K. Bloom. 2003. Yeast kinetochores do not stabilize Stu2p-dependent spindle microtubule dynamics. *Mol Biol Cell*. 14:4181-4195.
- Piazza, I., A. Rutkowska, A. Ori, M. Walczak, J. Metz, V. Pelechano, M. Beck, and C.H. Haering. 2014. Association of condensin with chromosomes depends on DNA binding by its HEAT-repeat subunits. *Nat Struct Mol Biol*. 21:560-568.
- Quammen, C.W., A.C. Richardson, J. Haase, B.D. Harrison, R.M. Taylor, 2nd, and K.S. Bloom. 2008. FluoroSim: A Visual Problem-Solving Environment for Fluorescence Microscopy. *Eurographics Workshop Vis Comput Biomed*. 2008:151-158.
- Ribeiro, S.A., J.C. Gatlin, Y. Dong, A. Joglekar, L. Cameron, D.F. Hudson, C.J. Farr, B.F. McEwen, E.D. Salmon, W.C. Earnshaw, and P. Vagnarelli. 2009. Condensin regulates the stiffness of vertebrate centromeres. *Mol Biol Cell*. 20:2371-2380.
- Rubinstein, M., and R.H. Colby. 2003. *Polymer physics*. Oxford University Press, Oxford ; New York. xi, 440 p. pp.

- Shintomi, K., F. Inoue, H. Watanabe, K. Ohsumi, M. Ohsugi, and T. Hirano. 2017. Mitotic chromosome assembly despite nucleosome depletion in *Xenopus* egg extracts. *Science*. 356:1284-1287.
- Stephens, A.D., J. Haase, L. Vicci, R.M. Taylor, 2nd, and K. Bloom. 2011. Cohesin, condensin, and the intramolecular centromere loop together generate the mitotic chromatin spring. *J Cell Biol*. 193:1167-1180.
- Stigler, J., G.O. Camdere, D.E. Koshland, and E.C. Greene. 2016. Single-Molecule Imaging Reveals a Collapsed Conformational State for DNA-Bound Cohesin. *Cell Rep*. 15:988-998.
- Tanaka, T., M.P. Cosma, K. Wirth, and K. Nasmyth. 1999. Identification of cohesin association sites at centromeres and along chromosome arms. *Cell*. 98:847-858.
- Terakawa, T., S. Bisht, J.M. Eeftens, C. Dekker, C.H. Haering, and E.C. Greene. 2017. The condensin complex is a mechanochemical motor that translocates along DNA. *Science*. 358:672-676.
- Uhlmann, F. 2016. SMC complexes: from DNA to chromosomes. *Nat Rev Mol Cell Biol*. 17:399-412.
- Verdaasdonk, J.S., P.A. Vasquez, R.M. Barry, T. Barry, S. Goodwin, M.G. Forest, and K. Bloom. 2013. Centromere tethering confines chromosome domains. *Mol Cell*. 52:819-831.
- Wan, X., R.P. O'Quinn, H.L. Pierce, A.P. Joglekar, W.E. Gall, J.G. DeLuca, C.W. Carroll, S.T. Liu, T.J. Yen, B.F. McEwen, P.T. Stukenberg, A. Desai, and E.D. Salmon. 2009. Protein architecture of the human kinetochore microtubule attachment site. *Cell*. 137:672-684.
- Wang, B.D., D. Eyre, M. Basrai, M. Lichten, and A. Strunnikov. 2005. Condensin binding at distinct and specific chromosomal sites in the *Saccharomyces cerevisiae* genome. *Mol Cell Biol*. 25:7216-7225.
- Weber, S.A., J.L. Gerton, J.E. Polancic, J.L. DeRisi, D. Koshland, and P.C. Megee. 2004. The kinetochore is an enhancer of pericentric cohesin binding. *PLoS Biol*. 2:E260.
- Yeh, E., J. Haase, L.V. Paliulis, A. Joglekar, L. Bond, D. Bouck, E.D. Salmon, and K.S. Bloom. 2008. Pericentric chromatin is organized into an intramolecular loop in mitosis. *Curr Biol*. 18:81-90.

CHAPTER 5: FUTURE DIRECTIONS

Nucleosome Remodeling's Influence on Pericentric Chromatin Dynamics

The fluorescently labeled, conditionally dicentric plasmid, pT431 (Dewar et al., 2004), used in Chapters 1 and 4 is a useful tool into how DNA-binding protein complexes influence chromatin organization and dynamics. While the studies above highlight the role of condensin-mediate loops in the organization of pericentric chromatin, previous work has demonstrated that nucleosome remodeling plays a key role in the dynamics of pericentric chromatin. Nucleosomes exhibit greater turnover in the pericentric region than the arm region of chromosomes during metaphase (Verdaasdonk et al., 2012). A reduction in tension from the microtubule-depolymerizing drug nocodazole or disrupting kinetochore function results in decreased turnover of nucleosomes (Verdaasdonk et al., 2012). Interestingly, a global reduction of histone H3 (using a conditional galactose promoter) and the condensin temperature sensitive allele *brn1-9* each resulted in longer metaphase spindle lengths, while only *brn1-9* cells exhibited significantly greater spindle length variation (Stephens et al., 2011). Since both histones and condensin act to compact pericentric chromatin but only condensin seems to stabilize pericentric chromatin fluctuations, how nucleosome remodeling is regulated by tension remains an open question. Moreover, a null mutation of the histone deacetylase Sir2 has shown to alter the distribution of pericentric condensin (Stephens et al., 2013), although whether the altered distribution of condensin is due to altered nucleosome remodeling or increased pericentric cohesin is unclear. Given that chromatin loops isolate tension to axial chromatin, it is possible that condensin could be influencing pericentric nucleosome remodeling and vice versa.

A useful experiment would be to test if nucleosome turnover is altered in a *sir2Δ* and *brn1-9* mutants using the same Fluorescent Recovery After Photobleaching (FRAP) technique employed in Verdaasdonk et al. (2012). Simulations of nucleosome remodeling using ChromoShake may also yield insights into how condensin-mediate loops alter the tension and thus nucleosome remodeling of a

simulated dicentric plasmid. Additionally, the tetO/TetR-GFP array on the dicentric plasmid can be combined an RFP-labeled histone protein to utilize Förster Resonance Energy Transfer (FRET) to monitor only the histone dynamics of the tetO/TetR-GFP array. This FRET-based imaging of histone dynamics would potentially provide precise monitoring of histone dynamics in situations with high tension, when the second centromere is active, and low tension, when the second centromere is inactive.

Machine-Learning-Assisted Model Fitting of Protein Distributions to Fluorescent Images

One of the original goals of the Microscope Simulator 2 program (Quammen et al., 2008) was to allow users build three dimensional models to fit fluorescent images. This aspect of the Microscope Simulator 2 program was used to describe the dimensions of the cohesin barrel (Stephens et al., 2013). However, given the advance in machine learning techniques over the past decade, we can now use model fitting with much greater precision. Rather than generating simulated images and comparing a single metric measured from the images, a user could load in an experimental image stack and have a list of fluorophore locations returned to the user. One type of machine learning technique that is has proved successful with imaging data is the Convolution Neural Net (CNN). A recent study has employed a CNN to accelerate super-resolution localization microscopy and enabling super-resolution reconstructions from wide-field images (Ouyang et al., 2018). This study acts a proof-of-concept for converting widefield images into precise fluorophore locations. Using Microscope Simulator 2 we can generate the large number of images and precise fluorophore locations needed to properly train a CNN. This technique can be validated on biological protein complexes with known structures. Once properly validated, this technique could provide the precision of super resolution microscopy with the speed of wide-field imaging.

REFERENCES

- Dewar, H., K. Tanaka, K. Nasmyth, and T.U. Tanaka. 2004. Tension between two kinetochores suffices for their bi-orientation on the mitotic spindle. *Nature*. 428:93-97.
- Ouyang, W., A. Aristov, M. Lelek, X. Hao, and C. Zimmer. 2018. Deep learning massively accelerates super-resolution localization microscopy. *Nat Biotechnol*. 36:460-468.
- Quammen, C.W., A.C. Richardson, J. Haase, B.D. Harrison, R.M. Taylor, 2nd, and K.S. Bloom. 2008. FluoroSim: A Visual Problem-Solving Environment for Fluorescence Microscopy. *Eurographics Workshop Vis Comput Biomed*. 2008:151-158.
- Stephens, A.D., J. Haase, L. Vicci, R.M. Taylor, 2nd, and K. Bloom. 2011. Cohesin, condensin, and the intramolecular centromere loop together generate the mitotic chromatin spring. *J Cell Biol*. 193:1167-1180.
- Stephens, A.D., C.W. Quammen, B. Chang, J. Haase, R.M. Taylor, 2nd, and K. Bloom. 2013. The spatial segregation of pericentric cohesin and condensin in the mitotic spindle. *Mol Biol Cell*. 24:3909-3919.
- Verdaasdonk, J.S., R. Gardner, A.D. Stephens, E. Yeh, and K. Bloom. 2012. Tension-dependent nucleosome remodeling at the pericentromere in yeast. *Mol Biol Cell*. 23:2560-2570.

APPENDIX 1: CHROMOSHAKE MANUAL¹

This document will guide the user through installing and running ChromoShake and the rendering and analysis programs. Throughout this guide, we will be using a 1-micron polymer chain as an example. This guide will only cover Window's based systems, although ChromoShake's source code, which has been provided at http://bloomlab.web.unc.edu/files/2016/01/Source_code.zip, has been compiled and run on UNIX-based systems.

ChromoShake Installation Using Microsoft Installer

- Download chromoShake_1_2_0.msi installer.
http://bloomlab.web.unc.edu/files/2016/01/chromoShake_1_2_0.zip
- Run the installer and follow the instructions.

Create a 1- μ m chain

- Open the Window's Command Prompt, cmd.exe, as an administrator. Administrator privileges are needed to write out files to certain locations.
- Navigate to chromoShake_1_2.0 directory containing the program using cd. By default, the location of chromoShake_make_linear_chain.exe is:
C:\Program Files\CISMM.org\chromoShake_1_2.0\
 - Type: cd "C:\Program Files\CISMM.org\chromoShake_1.2.0"
 - NOTE: Include the double quotations for account for the space.
- Run chromoShake_make_linear_chain.exe and save output to a file named default_chain.cfg
 - Type: chromoShake_make_linear_chain.exe > default_chain.cfg
 - Open the .cfg file using a text editor such as Notepad or WordPad to see the default conditions and locations of the masses.

¹ This manual previously appeared within the supplementary materials in Molecular Biology of the Cell. The original citation is as follows: Lawrimore, J., Aicher, J.K., Hahn, P., Fulp, A., Kompa, B., Vicci, L., Falvo, M., Taylor, R.M., 2nd, and Bloom, K. (2016). ChromoShake: a chromosome dynamics simulator reveals that chromatin loops stiffen centromeric chromatin. Mol Biol Cell 27, 153-166.

Run ChromoShake

- Run chromoShake.exe on the default_chain.cfg file, outputting coordinates every 10 microseconds (2 nanosecond timestep per calculation * 5000 calculations between outputs), for 1 millisecond (100 outputs * 10 microsecond per output). Save output to default_chain.out file.
 - Type: chromoShake.exe –openCL_dir openCL –save default_chain.out 5000 100 default_chain.cfg
 - The –openCL flag tag directs ChromoShake to the openCL files installed with the MSI installer. The default location is:
C:\Program Files\CISMM.org\chromoShake_1.2.0\openCL

NOTE: ChromoShake is not compatible with all versions of the OpenCL compiler. A common error is:

Constructing simulation

--- Build log ---

```
C:\cygwin64\tmp\OCLD906.tmp.cl(54): error: identifier "M_PI" is undefined
      CS_REAL angle = fabs( M_PI - acos( dot( left, right ) ) );
                          ^
```

```
C:\cygwin64\tmp\OCLD906.tmp.cl(59): warning: double-precision constant is
represented as single-precision constant because double is not
enabled
if ( any( isnan( f ) ) || angle < 0.001 ) {
^
```

1 error detected in the compilation of "C:\cygwin64\tmp\OCLD906.tmp.cl".

Internal error: clc compiler invocation failed.

ERROR: clBuildProgram in Force Hinge (Program build failure)

Update drivers to latest version to test for GPU compatibility. Otherwise specify CPU usage by typing

chromoShake.exe –CPU –save default_chain.out 5000 100 default_chain.cfg

View 1- μ m chain using ChromoView

- Open chromoView.exe. Unlike ChromoShake, ChromoView has a graphical interface. By default ChromoView is located at C:\Program Files\CISMM.org\chromoShake_1.2.0\
- Click "Load Simulation Output File"
- Select default_chain.out file.
- NOTE: chromoView.exe reads in all data before rendering, so larger files (i.e. > 3 Gigabytes) may not load due to lack of memory. You can view simulations that are currently running.

Rendering with Blender

The required files are available at <http://bloomlab.web.unc.edu/files/2016/01/Video.zip>. A bash script, a python script, and a blender file are provided to parse .out files in to Blender. Blender is an open source program 3D graphics and animation software. Blender can be downloaded from <https://www.blender.org/download/>. The python script has been tested with Blender version 2.68a. The script outputs an untitled.blend file that can be loaded into blender and then rendered. Note the bash script is not fully compatible with Cygwin. The bash script will successfully make the files needed, but Blender will fail to locate the files based on differences in directory structure.

- To create a .blend file using the Windows and the Command Prompt
 - Copy and rename the vidprecode4_batch.blend file to default_chain.blend in same directory as default_chain.out
 - Copy and rename the read_chromoShake_file_into_blender.py to default_chain.py in same directory as default_chain.out
 - Open default_chain.py with a text editor or IDLE. Change 'INPUT_FILE.txt' in line 5 to 'default_chain.out'
 - Open Command Prompt
 - Change directory to directory containing default_chain.blend, default_chain.out, and default_chain.py
 - Assuming that blender is in this default directory, type: "C:\Program Files(x86)\Blender Foundation\Blender\blender.exe" -b default_chain.blend -P default_chain.py -noaudio
 - This will output an untitled.blend file. Open this file in Blender to render the file.
 - NOTE: The default camera angle for linear chains is end on so first rendered image will look like a single bead.

Analysis Programs and Usage

Analysis programs can be run on UNIX based systems or on windows with Cygwin (<https://www.cygwin.com/>) installed. A C++ compiler is needed. Existing programs require Python (<https://www.python.org/>), PERL (<https://www.perl.org/get.html>) and BASH script (.sh) support.

Mean Squared Displacement Analysis

The required files are available at http://bloomlab.web.unc.edu/files/2016/01/MSD_scripts.zip.

This program calculates the mean square displacement of a single bead or the mean position of an array of beads. The program requires the .out file have the header removed and the bead coordinates be changed from meters to microns.

BASH Scripts

These scripts link together a set of PERL programs and C++ programs to produce “colorfiles” (known as SRCs) that indicate which beads are measured by mean squared displacement. The bead position files used to generate SRCs that were used in this paper are kept in the folder beadPositionFiles. Each bead position file has a row of numbers that correspond to bead numbers (bead 0, 1, 2, 3, etc.). The mean 3D position of each of the beads in a row will be calculated by coord_summary.cpp. Each row will then become a single file of the average 3D position of all the beads over time. The MSD is calculated from these average 3D positions. The bead position files can be made by the updated chromoShake_make_spindle.cpp program (not included in MSI installer but is in the source code). An example bash script, updated_MSD_example_summary.sh, has been provided. The .out files must be placed in the OUTFILE directory. These data files can also be trimmed to a timepoint to allow for equilibration. The OUTFILE directory currently contains truncated (0.05 to 0.055 seconds) centromere models as examples. The WT.out simulation contains cohesin and condensin. The no_coh.out simulations lacks cohesin but contains condensin. The no_cond.out simulation contains cohesin but lacks condensin. The no_coh_no_cond.out lacks cohesin and lacks condensin. Compile the coord_summary.cpp to coord_summary.exe (for Windows) or coord_summary (for UNIX). If on a UNIX system change line 8 in MSD_summary.sh from coord_summary.exe to coord_summary. To run scripts: sh updated_MSD_example_summary.sh beadPositionFiles\10kb_loop_default. Several directories will be created. SRCs contain the SRC files. Coord_summs contain the coordinate summary containing the average 3D positions. MSDs will contain the MSD files plus a summary MSD file with all the MSDs over time of each file concatenated horizontally.

ChromoMap MATLAB Script

The script is available at http://bloomlab.web.unc.edu/files/2016/01/Simulation_heatmaps.zip.

This MATLAB script creates a heatmap of the array position over simulated time. Reads in the coord_summ directory from the MSD analysis script. To only sample “in-focus” arrays so data can be directly compared to imaging data only the center 200 nm are sampled in the Z direction, so minimum Z is -100 and maximum Z is 100. □□NOTE – For this program, the axis have been rotated to match our typical imaging axis. Z is orthogonal to the XY plane where the X is parallel to the spindle axis and Y is perpendicular.

CorrMotion MATLAB Script

The script is available at http://bloomlab.web.unc.edu/files/2016/01/Correlated_motion.zip. This MATLAB script calculates the correlated motion of neighboring chromatin loops and sisters. Neighboring loops cross-linked by cohesin are “Cohesin Neighbors,” while neighboring loops that are not cross-linked are “Unlinked Neighbors.” The program inputs the coord_summ files of the 10 kb loop (default) spindle model. The axes were not rotated in this program so the Z dimension is parallel to the spindle axis.

Radius of gyration MATLAB Script

The script is available at http://bloomlab.web.unc.edu/files/2016/01/Radius_of_gyration.zip. The function radiusOfGyration_color1.m calculates the radius of gyration of all the beads labeled with the color 1 (red in ChromoView). This script was used to measure the radius of gyration of the primary axis of a bottlebrush polymer simulation and the radius of gyration of a ring of chromatin with cohesin. The input is a .out file. The function radiusOfGyration_cohesinRings.m calculates the average radius of gyration over time of cohesin rings labeled with the color 5 (white in ChromoView). The input is an out file.

Old Format Analysis Programs

The following analysis programs were developed for a prior version of ChromoShake. The .out files need to be converted using the following PERL scripts to be compatible with these analysis programs.

Header Removal

The script is available at http://bloomlab.web.unc.edu/files/2016/01/Header_removal.zip. All data before the line “Time 0” must be deleted for the old format analysis programs. This can be

accomplished using various text editors but can be problematic for larger files. We have provided a PERL script to remove the header named ChromoShakeRemoveHeader.pl using standard input and output. To remove header using ChromoShakeRemoveHeader.pl ensure that PERL is installed on your computer. To use the script type the following in the command prompt: perl ChromoShakeRemoveHeader.pl < default_chain.out > default_chain_noHead.txt.

Unit Conversion

The script is available at http://bloomlab.web.unc.edu/files/2016/01/Unit_conversion.zip. This PERL script converts the coordinates from meters to microns. To use type in the following into the command prompt: perl ChromoShakeUnitConvert.pl < default_chain_noHead.txt > default_chain_noHead_um.txt.

Radial Displacement Analysis

The program is available at http://bloomlab.web.unc.edu/files/2016/01/Radial_analysis.zip. The C++ program, cohesin_summary.cpp, parses the bead coordinate files (lacking header, beads position in microns) based on a color file. The color file contains a list of integers that indicates the color of the bead. This program parses the coordinates of the beads corresponding with the color 4 (white, originally indicated cohesin). Two SRC files have been provided in Radial_analysis directory, default_chain_SRC.txt, that labels all beads in a default chain, and someRandomColor.txt, that labels cohesin in default centromere model. To use this program type in the following into the command prompt: cohesin_summary.exe default_chain_SRC.txt default_chain_noHead_um.txt

Brownian to Fluorosim Conversion

The scripts are available at http://bloomlab.web.unc.edu/files/2016/01/Brownian_to_fluorosim.zip. These Python scripts convert to the old format of ChromoShake's output (no header, coordinates in microns) to XML files that Microscope Simulator 2 can parse to generate simulated fluorescent images. A detailed README.html file is included and contains usage instructions. Microscope Simulator 2 can be downloaded from CISMM's website at <http://cismm.cs.unc.edu/downloads/>. In the README file \$point_colors refers to the colorfiles. The same files used in the Radial Displacement Analysis section can also be used to indicate which beads should be fluorescent. The number 4 labels a bead for fluorescence. In the README file \$coordinates refers to the .out files after the header has been removed

and the coordinate units have been converted from meters to microns. The XML files generated by ParseBrownian.py can be open directly using Microscope Simulator 2. The default view is too large in Microscope Simulator 2 for chromoShake models, so you must zoom into the center of the grid to view the models.

APPENDIX 2: AUTOTRACKER PIPELINE GUIDE

The autotracker pipeline was designed to accelerate particle tracking of sister chromatids labeled with a fluorescent operator/reporter system such as lacO/LacR-GFP array. This pipeline assumes only two foci are present within each image. The pipeline requires the user to operate FIJI (FIJI Is Just ImageJ), a distribution of ImageJ2. FIJI is free to use and is available to download at <https://imagej.net>. However, any image process software that can crop individual yeast nuclei and save the resulting cropped images in a TIFF format can substitute for FIJI. The remainder of the pipeline requires MATLAB. The MATLAB scripts were written using MATLAB 2017a and may not be compatible with older versions of MATLAB. This guide was written assuming the user acquired three-color timelapses using Nikon Elements being saved in the ND2 format.

ImageJ/FIJI Cell Selection

1. Open raw ND2 images using ImageJ/FIJI using Bio-Formats Importer under Plugins>>Bio-Formats
2. Ensure that “Open all series” and “Concatenate series when compatible” are checked.
3. Hit OK.
4. Wait for file to open. Timelapse files can be around 1 GB or larger, this can take a few minutes to load into memory. I would suggest moving the ND2 file to your hard drive before attempting to open them if they are stored online.
5. Hit “t” to open ROI Manager
6. Hit “SHIFT+C” to open B&C (brightness and contrast menu)
7. Change Z slider to the middle plane (for 7 steps this is $z=4/7$)
 - For most image stacks the Color order is: Trans, GFPbi, RFPbi (C=0, C=1, C=2 respectively). NOTE: the Trans channel only has an image at the “Home” position, the rest of the z-planes will be blank (all 0s).
8. Hit “Reset” button in B&C window.
9. Change to channels one and two (indexing starts at 0 in ImageJ/FIJI) using C slider.
10. Adjust contrast for each channel by first hitting “Reset” button then user Minimum and Maximum sliders to adjust contrast to your liking.

11. Navigate to the GFP channel (typically middle channel)
12. Draw a Rectangular ROI around the cell containing the two GFP foci you wish to track
 - By default, the Rectangular ROI drawing tool should be selected, if not, it is the box icon on the far left of the ImageJ/FIJI window
13. Use the white boxes on the edges of the ROI to resize to your liking
 - NOTE: Ensure that ONLY TWO foci are in your ROI over all timepoints. This will prevent errors in auto_track and tedious corrections in verify_paths. Be sure to scrub through all timepoints.
14. To confirm your ROI hit “t”. Three hyphenated numbers should appear in the ROI Manager.
 - To view all your ROIs on the current image file, check the box next to “Show All” in the ROI manager. Uncheck the box next to “Labels” to turn off the numbers that typically block the view of your foci.
15. When all ROIs are selected, hit the “More>>” button in the ROI Manager and select “Save...” from the pop-up menu.
16. IMPORTANT: Click on the name of the image you are currently viewing. If you are unsure of which file you are currently viewing, the filename appears at the top of the main window. REMOVE the .nd2 portion of the name and then hit “Save”.
 - NOTE: If more than one ROI has been created for the image the file will save a .ZIP file, otherwise it will be saved as a .ROI file.
17. After saving the ROI(s) press “Delete” in the ROI Manager. A pop-up window will appear stating “Delete all items on the list?” Press “Yes”.
 - NOTE: If an ROI happens to be select at the time you press “Delete”, that ROI will be removed from the list without any request for confirmation. Hit “Delete” again to delete all ROIs in the list.
18. Close the image window and repeat above steps until all images have been screened for cells containing 2 GFP foci.

Notes for ImageJ/FIJI Cell Selection

- Typically, you will select cells with a medium sized bud. However, cells with large or misshapen buds are okay to track.
- Do NOT select cells in which one of the foci stretches into a filamentous line.
- Do NOT select cells in which the foci separate into mother and daughter buds. This cell is undergoing anaphase and should not be tracked.
- Foci that join may be difficult to track but should be selected anyway.
- If you are unsure if you should select a cell, go ahead and selected it anyway. The program `verify_paths.m` has a feature that will allow you to quickly discard difficult to track cells.

ImageJ/FIJI `timelapse_bioformats_split_dir.ijm`

1. IMPORTANT: The macro (type of program) you will run in ImageJ/FIJI requires that each ND2 file in a directory is followed by either a .ZIP or .ROI file. ND2 files that did not contain any suitable cells need to be removed from the directory prior to running the macro.
2. Select “Plugins>>Macros>>Run”
3. Locate the ImageJ Macro named “`timelapse_bioformats_split_dir.ijm`”
4. You will be prompted to choose a source directory. Select the directory that contains your ND2 and ROI/ZIP files. REMEMBER: each ND2 file MUST be followed by a ROI/ZIP file. Remove any ND2 files without corresponding ROI/ZIP files prior to running the script.
5. The script will loop through all the images and automatically crop and divide the ND2 files into separate channels. The source directory will contain three .TIF files for each cell selected from the ND2 file.

MATLAB `auto_track.m`

1. Open MATLAB
2. Add `auto_track` directory to path
3. Add `bformatlab` folder to path
 - The folder `bformatlab` is available from the Open Microscopy Environment group at <https://www.openmicroscopy.org/bio-formats/>. Download the MATLAB toolbox. This package enables MATLAB to parse a variety of image formats.

4. Change directory to the same directory containing the cropped GFP.tif files you created using the `timelapse_bioformats_split_dir.ijm` script.
5. Run `auto_track` by typing `auto_track` and hitting enter. Folders with plane-picked .tif images and tracking data, including the radius of confinement in nm (`rc` variable), mean squared displacement in nm (`msd` variable), initial spot separation vs change in spot separation in pixels (`delta_dist` variables and the corrected foci coordinates (`path1` and `path2`, columns are X pixel position, Y pixel position, Z-depth in nm, and in-focus plane number). The `coords1` and `coords2` variables are the first guess of the foci's positions that are checked using a distance-based cost algorithm. The sub-pixel positions from the Gaussian fittings using the coordinates within `path1` and `path2` are in `x_mu1`, `x_mu2`, `y_mu1`, and `y_mu2`.

Notes for MATLAB `auto_track.m`

- The `auto_track.m` program is NOT perfect. Paths of foci must be verified using `verify_paths` function.
- By default, the `auto_track.m` program only parses the GFP images by searching for files ending with GFP.tif. To change this behavior, edit line 8 in `auto_track.m` to specify the files you would like to parse, i.e. change to `gfp_files = dir('*RFP.tif');` to track the RFP images.

MATLAB `verify_paths.m`

1. The `auto_track` program creates a folder for each image it tracks in the same folder as the original TIFF image. The MATLAB function `verify_paths.m` relies on this structure and was designed to be run from the same folder `auto_track.m` originally ran. Note, if you want to move the folders outputted by `auto_track.m` to a new location, be sure to also move the corresponding *GFP.tif file with it (they will have the same name) as `verify_paths.m` needs this image to function.
2. To run, type `verify_paths(directory)` into the command line with `directory` being the path to the root folder containing the folders outputted by the `auto_track` program.
3. A simple interface will open displaying the image name and the first in-focus plane for a focus with a red circle mapped over it. The circle is the results of a 2D Gaussian fit over the focus. If the red circle is not over a focus, then the `auto_track` program committed an error.

4. To advance to the first in-focus plane for the other focus click the left mouse button. A green circle should map over the other focus. If the green circle is not over a focus or the green circle is over the same focus as before, then the `auto_track` program committed an error.
5. If no error has been detected simply continue through the timelapse by clicking the left mouse button.
6. If an error has occurred press the space bar. A new window will open with the first plane of that z-stack displayed. Use the left and right arrow keys to navigate through the planes of the z-stack to locate the in-focus plane for the focus you want to re-track. Once you have navigated to the desired image plane, press the space bar. A new window will open displaying the image plane you selected. Use your mouse to right-click on the foci you want to re-track. After right-clicking on the focus, the window will close, and the original window will be redisplayed with the next in-focus image plane.
7. If you correct a tracking error during a timelapse the original folder and image will be moved to a folder named `error`. A new folder with `_fixed` appended to the original folder name will be created in its place with the correct tracking data and in-focus image stacks for each foci.
8. If the timelapse you are verifying is too noisy or has photobleached too much for accurate tracking press the escape key. The display will close and the `auto_track` folder and the original TIFF file will be moved to the folder named `hopeless`.
9. The `verify_paths` function will parse all the tracking folders in a given folder.

MATLAB midpoint_summary.m

1. After all the tracks are verified, move the correct image folders to the same root folder.
2. Run the `midpoint_summary.m` script from within that root folder. The script will open all the folders within the root folder and search for any MAT files within. The radius of confinement (`rc` variable), the mean squared displacement (`msd` variable), and the spot separation vs change in spot separation (`dist_delta` variable) will be collected from each file and stored in the variables `ens_rc`, `msd_cell` and `ens_dist_delta` respectively.

APPENDIX 3: DICENTRIC PLASMID TRACKING INTERFACE

This is a manual for the MATLAB Graphical User Interface (GUI) `population_GUI_v1_2.m`. This GUI is designed to track the length, width and position of the fluorescently labeled, conditionally dicentric plasmid pT431 and the positions of the fluorescently labeled spindle pole bodies. The program measures the plasmid's tetO/TetR-GFP array signal by subtracting the user-selected, nuclear background signal from the plasmid signal and then uses the MATLAB thresholding function, `multithresh`, to convert the background-subtracted image into a binary mask. The binary mask is fit to an ellipse using the built-in function `regionprops`. The image plane, major axis length, the minor axis length, the aspect ratio (major axis length divided by the minor axis length), centroid, if the plasmid signal is split, and an image of the plasmid signal after the threshold is applied is recorded in a cell array. The cell array also contains the three-dimensional spindle length, the spindle pole body positions, the spindle pole body's brightest pixel value and the shortest distance between the spindle pole body and the plasmid signal (recorded as `kMT1` and `kMT2`).

Cell Selection (Optional)

If you want to track a single plasmid over time, it is generally easier to track an image that only contains the cell of interest. Appendix 2 describes a method to quickly cell select using FIJI/ImageJ.

MATLAB Plasmid GUI Manual

1. Open MATLAB. The GUI was written with MATLAB 2015a using MATLAB's GUIDE application. The program may not function correctly with older versions of MATLAB.
2. The GUI relies on the bioformats plugin for MATLAB. Ensure the `bformats` folder is added to path. The folder `bformatlab` is available from the Open Microscopy Environment group at <https://www.openmicroscopy.org/bio-formats/>. Download the MATLAB toolbox. This package enables MATLAB to parse a variety of image formats.
3. Ensure that the folder containing the `population_GUI_v1_2.m` and `population_GUI_v1_2.fig` files are added to path.
4. For convenience, navigate MATLAB to the folder containing the image stacks you wish to analyze. This prevents the user from having to tediously navigate to the image files.

5. Run `population_GUI_v1_2.m`. If the program is added to path you can run the GUI by typing `population_GUI_v1_2` in the command line. The GUI will open in a new window. You can expand the GUI to full screen.
6. In the upper-left corner click File>Open Image.
7. Select the plasmid image stack first then the corresponding spindle pole body stack second. The plasmid image stack will be on the left. The spindle pole body image stack will be on the right.
8. At the bottom of the GUI is a slider with two ratios. The left ratio is the plane number/total plane number. The right ratio is the current z-stack/total number of z-stacks. The number of z-stacks is determined by the Step Number variable located in the top-right of the GUI. The Step Number, Step Size (nm) and Pixel Size variables are editable. If you wish to alter the default settings permanently close the GUI window, type `guide` into MATLAB's command line, click the Open Existing GUI tab, click the Browse button, navigate to the `population_GUI_v1_2.fig` file and select the file. MATLAB's guide interface will open in a new window. Double-click on the white box of containing the variable value you wish to change. A property inspector window will open. Double-click on the value for the String variable in the right column. Change that value to your desired number and press the ENTER key. Close the property inspector window. In the guide window the variable should the new value you entered. Click on the save icon in the guide window to save your changes. This will permanently change the default value of the variable for that instance of the `population_GUI_v1_2` file. If the Pixel Size (nm) or Step Size (nm) variables are incorrect, the Major Axis, Minor Axis, 3D Spindle Length, kMT 1 and kMT2 variables will also be incorrect; therefore, please ensure these variables are accurate for your image stacks.
9. You can zoom in on the image stack using the magnifying tool. Click on the magnifying glass icon in the top-left of the GUI. The cursor will turn from an arrow to a double crosshair when hovering over the image stacks. To zoom in either hold down the left mouse button and drag a box around the desired region or left click on the region you wish to enhance. Right-click on the mouse to zoom out. To reset the image to the original zoom, double-click the left mouse button. To exist zoom mode, click on the magnifying glass icon. Note, if no plasmid or spindle pole body has been selected, changing the image plane will reset the zoom. However, once a plasmid or spindle pole

body has been selected (a green or red dot has been overlaid over the plasmid or spindle pole body respectively) the zoom will remain the same if the user changes the image plane displayed.

10. Use the slider to navigate to the in-focus plane of the plasmid stack.
11. Click on the Select BG button. This will convert the cursor from an arrow to a crosshair. With the left mouse button held down, drag a rectangle over a nuclear background region. Release the left mouse button. You can drag the rectangle around the image by holding the left mouse button with the cursor within the rectangle and moving the rectangle with the left mouse button held down. You can resize the rectangle using the blue boxes along the rectangle's border. Once the rectangle is in the desired location within the nuclear signal double click within the rectangle. The text box containing Average BG in the top-left of GUI will convert to the average signal intensity within the rectangle.
12. Click on the Select FG button. Drag a rectangle over the plasmid signal. Click on the rectangle once. The selected region will appear in the top-left of the GUI.
13. Click the left mouse button once. The background subtracted image will appear.
14. Click the left mouse button again. The binary mask image will appear.
15. If the binary mask contains background noise you can use the morphological operators erode and dilate to remove it. First, click the Erode button. This will erode all binary objects within the image. This will remove the noise but also shrink the plasmid signal's binary mask. To return the binary mask to its original proportions, click the Dilate button.
16. Click on the Get Axis Lengths button to measure the current binary mask. The text boxes containing Major Axis Length and Minor Axis Length will update with the binary mask's measurements.
17. To clear the recorded axis length for the binary mask, click the Clear Axis Length button.
18. If there are multiple, discontinuous plasmid signals, click the Plasmid Split checkbox. If the plasmid signal is split, only one of the signals can be tracked at a time. The Use KMT1? and Use KMT2? checkboxes allow the user to specify which spindle pole body to use to as a reference point when measuring the nearest distance from the spindle pole body to most proximal plasmid signal, which is what the kMT value represents.

19. To record that there was no plasmid in the cell of interest, click the No Plasmid Detected checkbox.
20. Use the slider to navigate to the in-focus plane of a spindle pole body.
21. Click on the Find SPB 1 button and then click on the spindle pole body signal. A red X will appear over the signal. The program will automatically find the brightest pixel value within a 5-pixel by 5-pixel by 7-plane volume.
22. Repeat the above step to track the second spindle pole body.
23. Once both spindle pole bodies have been tracked click on the Calc Spindle Button. The 3D spindle length will be displayed below the Calc Spindle button.
24. If one or both spindle pole body signals is not in the image stack, you can omit them using the No SPB 1 or No SPB 2 checkboxes. The user should still press the Calc Spindle button to measure the kMT value that can be calculated prior to pressing the Record Data button.
25. Once the plasmid axis lengths and the spindle pole bodies have been tracked, click on the Record Data button to write those cell's measurements in the cell array.
26. To save the cell array to a data file, click File>Save Data. The user must save the data prior to closing the interface or all the recorded data will be lost!